GEOLOGICAL SURVEY OF CANADA
COMMISSION GÉOLOGIQUE DU CANADA

Current Research 1999-D
Recherches en cours 1999-D

EASTERN CANADA AND NATIONAL AND GENERAL PROGRAMS

EST DU CANADA ET PROGRAMMES NATIONAUX ET GÉNÉRAUX

Natural Resources Canada
Ressources naturelles Canada
Canada

NOTICE TO LIBRARIANS AND INDEXERS

The Geological Survey's Current Research series contains many reports comparable in scope and subject matter to those appearing in scientific journals and other serials. Most contributions to Current Research include an abstract and bibliographic citation. It is hoped that these will assist you in cataloguing and indexing these reports and that this will result in a still wider dissemination of the results of the Geological Survey's research activities.

AVIS AUX BIBLIOTHÉCAIRES ET PRÉPARATEURS D'INDEX

La série Recherches en cours de la Commission géologique contient plusieurs rapports dont la portée et la nature sont comparables à celles des rapports qui paraissent dans les revues scientifiques et autres périodiques. La plupart des articles publiés dans Recherches en cours sont accompagnés d'un résumé et d'une bibliographie, ce qui vous permettra, on l'espère, de cataloguer et d'indexer ces rapports, d'où une meilleure diffusion des résultats de recherche de la Commission géologique.

GEOLOGICAL SURVEY OF CANADA
COMMISSION GÉOLOGIQUE DU CANADA

CURRENT RESEARCH 1999-D

EASTERN CANADA AND NATIONAL AND GENERAL PROGRAMS

RECHERCHES EN COURS 1999-D

EST DU CANADA ET PROGRAMMES NATIONAUX ET GÉNÉRAUX

1999

Catalogue No. M44-1999/4
ISBN 0-660-60780-8

Available in Canada from
Geological Survey of Canada offices:

601 Booth Street
Ottawa, Ontario K1A 0E8

3303-33rd Street N.W.
Calgary, Alberta T2L 2A7

101-605 Robson Street
Vancouver, B.C. V6B 5J3

A deposit copy of this publication is also available for reference
in selected public libraries across Canada

Price subject to change without notice

Cover illustration

Photograph, taken on the north flank of Mount Bélair, of an old, striated glacial groove trending 200° on a large outcrop that was striated and polished during the main regional ice flow towards 095°. *See* paper by Paradis and Bolduc, this volume. Photograph by A.M. Bolduc. GSC 1998-071

Photo en page couverture

Photo, prise sur le flanc nord du mont Bélair, d'une vieille cannelure striée orientée vers 200°, préservée sur un affleurement qui a été strié et poli lors du mouvement glaciaire régional vers 095°. Voir l'article de Paradis et Bolduc dans le présent volume. Photo : A.M. Bolduc GSC 1998-071

Separates

A limited number of separates of the papers that appear in this volume are available by direct request to the individual authors. The addresses of the Geological Survey of Canada offices follow:

Geological Survey of Canada
601 Booth Street
Ottawa, Ontario
K1A 0E8
(FAX: 613-996-9990)

Geological Survey of Canada (Calgary)
3303-33rd Street N.W.
Calgary, Alberta
T2L 2A7
(FAX: 403-292-5377)

Geological Survey of Canada (Pacific)
101-605 Robson Street
Vancouver, British Columbia
V6B 5J3
(FAX: 604-666-1124)

Geological Survey of Canada (Pacific)
P.O. Box 6000
9860 Saanich Road
Sidney, British Columbia
V8L 4B2
(FAX: 604-363-6565)

Geological Survey of Canada (Atlantic)
Bedford Institute of Oceanography
P.O. Box 1006
Dartmouth, Nova Scotia
B2Y 4A2
(FAX: 902-426-2256)

Geological Survey of Canada (Quebec)
2535, boulevard Laurier
C.P. 7500
Sainte-Foy (Québec)
G1V 4C7
(FAX: 418-654-2615)

Tirés à part

On peut obtenir un nombre limité de «tirés à part» des articles qui paraissent dans cette publication en s'adressant directement à chaque auteur. Les adresses des différents bureaux de la Commission géologique du Canada sont les suivantes :

Commission géologique du Canada
601, rue Booth
Ottawa (Ontario)
K1A 0E8
(Télécopieur : 613-996-9990)

Commission géologique du Canada (Calgary)
3303-33rd Street N.W.,
Calgary, Alberta
T2L 2A7
(Télécopieur : 403-292-5377)

Commission géologique du Canada (Pacifique)
101-605 Robson Street
Vancouver, British Columbia
V6B 5J3
(Télécopieur : 604-666-1124)

Commission géologique du Canada (Pacifique)
P.O. Box 6000
9860 Saanich Road
Sidney, British Columbia
V8L 4B2
(Télécopieur : 604-363-6565)

Commission géologique du Canada (Atlantique)
Institut océanographique Bedford
P.O. Box 1006
Dartmouth, Nova Scotia
B2Y 4A2
(Télécopieur : 902-426-2256)

Commission géologique du Canada (Québec)
2535, boulevard Laurier
C.P. 7500
Sainte-Foy (Québec)
G1V 4C7
(Télécopieur : 418-654-2615)

CONTENTS

Mouvement glaciaire vers le nord sur le piémont laurentien dans la région de Québec, Québec

Serge J. Paradis et Andrée M. Bolduc
Centre géoscientifique de Québec, Sainte-Foy

Paradis, S.J. et Bolduc, A.M., 1999: Mouvement glaciaire vers le nord sur le piémont laurentien dans la région de Québec, Québec; dans *Recherches en cours 1999-D; Commission géologique du Canada, p.* 1-7.

Résumé : Un relevé des marques d'érosion glaciaire dans la région de Québec a permis de reconnaître un mouvement glaciaire vers le nord sur la bordure sud des Laurentides jusqu'à une altitude d'environ 200 m. Ces nouvelles observations permettent d'envisager une avancée tardiglaciaire des glaces appalachiennes jusqu'au piémont laurentien sur la rive nord du Saint-Laurent. La découverte de ce mouvement glaciaire récent permet d'ajouter un nouvel événement à la chronologie générale des mouvements glaciaires dans le secteur à l'étude, laquelle comprend un premier mouvement glaciaire vers le sud-sud-ouest puis un deuxième vers le sud-est. Un rétablissement subséquent vers l'est suivi d'un réajustement vers le sud-est pourraient être reliés au développement puis à la disparition d'un courant de glace et d'une baie de vêlage dans la vallée du Saint-Laurent. Cette phase a été suivie par un dernier mouvement local vers le nord, en provenance des Appalaches.

Abstract: A survey of glacial flow indicators in the Québec City area has revealed the presence of a northward movement as far as the edge of the Laurentians to an elevation of about 200 m. This could indicate a late-glacial advance of Appalachian ice to the Laurentian Piedmont on the north shore of the St. Lawrence River. This young, northward movement adds a new element to the general chronology of ice flow in the region: initial ice flow to the south-southwest, followed by flow to the southeast. A recovery towards the east, followed by another shift to the southeast, could be linked to the development and disappearance of an ice stream and a calving bay in the St. Lawrence Valley. This phase was followed by a final, local, northward flow originating from the Appalachians.

INTRODUCTION

Des travaux de terrain entrepris en septembre 1998 en vue d'une nouvelle cartographie des formations superficielles ont inclu un relevé systématique des marques d'érosion glaciaire sur la rive nord du Saint-Laurent, dans la région de Québec (21 L/14). Ce relevé a permis de reconnaître un mouvement tardiglaciaire vers le nord dans la région à l'étude. Auparavant, des indices d'un mouvement glaciaire vers le nord n'avaient été reconnus que dans les hautes terres des Appalaches et le piémont appalachien (Chalmers, 1898; Clark, 1937; Cooke, 1937; Lamarche, 1971, 1974; Gauthier, 1975; Lortie, 1976; Lebuis et David, 1977; LaSalle et al., 1977; LaSalle, 1985; Chauvin et al., 1985).

Selon le modèle de déglaciation préconisé par LaSalle et al. (1977) et Chauvin et al. (1985), les glaces appalachiennes ont été isolées des glaces laurentidiennes par une baie de vêlage formée dans l'estuaire du Saint-Laurent. La présence de cette baie de vêlage a entraîné la réorientation et l'inversion de la direction de l'écoulement des glaces, soit vers le nord dans les hautes terres des Appalaches et le piémont appalachien, vers le nord-est près du fleuve et vers le sud-est dans le secteur de Québec. La progression de la baie de vêlage jusqu'aux environs de Saint-Jean-Port-Joli et les réajustements des masses glaciaires ont entraîné le dépôt des complexes morainiques de Saint-Antonin et de Saint-Jean-Port-Joli. La séparation complète et la stagnation des glaces appalachiennes ont donné lieu au dépôt du complexe morainique de Saint-Damien. Plus récemment, Parent et Occhietti (sous presse) ont attribué la réorientation des écoulements tardiglaciaires à la formation d'un grand courant glaciaire dans l'axe de la vallée du Saint-Laurent.

Le présent rapport se veut un compte rendu succinct des observations faites sur les marques d'écoulement glaciaire sur la rive nord du Saint-Laurent dans la région de Québec.

MÉTHODOLOGIE

Notre relevé a visé 71 affleurements rocheux striés dont 13 montrent des stries entrecroisées (figure 1). Toutes les stries glaciaires mesurées dans la région à l'étude sont sur un substratum rocheux constitué de roches ignées (granite, anorthosite et gabbro) et métamorphiques (gneiss) du Bouclier. Les stries glaciaires sont mieux conservées sur ces roches plus résistantes que sur les roches sédimentaires friables, surtout calcaire et shale, des basses terres du Saint-Laurent et des Appalaches. Ainsi, aucune strie glaciaire n'a été retrouvée dans la zone urbaine immédiate de la ville de Québec, d'autant plus que beaucoup de secteurs sont caractérisés par la présence de remblais et sont le site de toutes sortes de travaux subséquents. La polarité des stries glaciaires a été définie de façon générale en se basant principalement sur deux critères, soit la présence de microformes telles les queues-de-rat et les broutures, soit la présence de roches moutonnées.

La chronologie relative des écoulements glaciaires a été établie en étudiant le recoupement et la superposition des stries. Dans le cas de surfaces striées qui se recoupent, une surface striée plus ancienne, se trouvant relativement abritée, est protégée de l'érosion causée par un mouvement glaciaire subséquent (Klassen et Bolduc, 1984); typiquement, une troncature sépare les deux surfaces striées dont les stries ont des directions distinctes (Veillette, 1986), la surface plus ancienne étant située en contrebas de la troncature. Dans le cas de stries superposées, les stries glaciaires les plus récentes sont formées sur une surface striée plus ancienne, mais sans que cette dernière soit complètement oblitérée (Parent et Paradis, 1993).

Le mouvement tardiglaciaire a été reconnu grâce à l'identification de stries glaciaires indiquant un mouvement des glaces vers le nord, qui sont superposées sur une surface striée témoignant d'un écoulement vers le sud-est (figure 2a). Le sens de l'écoulement des glaces est donné par la répartition asymétrique des stries glaciaires superposées : la présence de marques d'écoulement glaciaire sur le côté sud-sud-ouest des microformes d'érosion, marques qui ne sont pas visibles sur le côté nord-nord-est des mêmes microformes, permet d'établir sans équivoque la polarité du mouvement glaciaire vers le nord (figures 2b et 2c).

RÉSULTATS

L'inventaire des mesures de stries glaciaires dans le secteur de Québec permet de reconstituer l'ensemble des écoulements glaciaires prépondérants (figure 3) et leur chronologie relative.

Les données relevées dans la région à l'étude permettent de reconnaître un premier mouvement glaciaire, le plus vieux, vers le sud-sud-ouest. Les mesures d'azimut de ce mouvement varient entre 200° et 215° et proviennent de quelques affleurements dans toute la région. Ce mouvement glaciaire a été suivi par un écoulement régional vers le sud-est, représenté par une série de stries glaciaires dont les azimuts varient de 145° à 150°.

Par la suite, un réajustement de la masse glaciaire aurait produit des stries glaciaires orientées vers l'est dont les azimuts sont concentrés entre 70° et 95°. L'inventaire général des stries glaciaires permet de définir une deuxième phase de réajustement de ce dernier mouvement glaciaire vers le sud-est reconnu dans tout le secteur à l'étude. Cette phase est caractérisée par des mesures d'azimuts qui sont groupées dans trois sous-ensembles, soit près de 70°, de 90° et de 120°.

Vient ensuite, dans le secteur de Québec, un mouvement des glaces vers le nord dont l'orientation varie de 340° à 20°. Les marques laissées par ce mouvement sont visibles sur quatre affleurements dans le piémont laurentien.

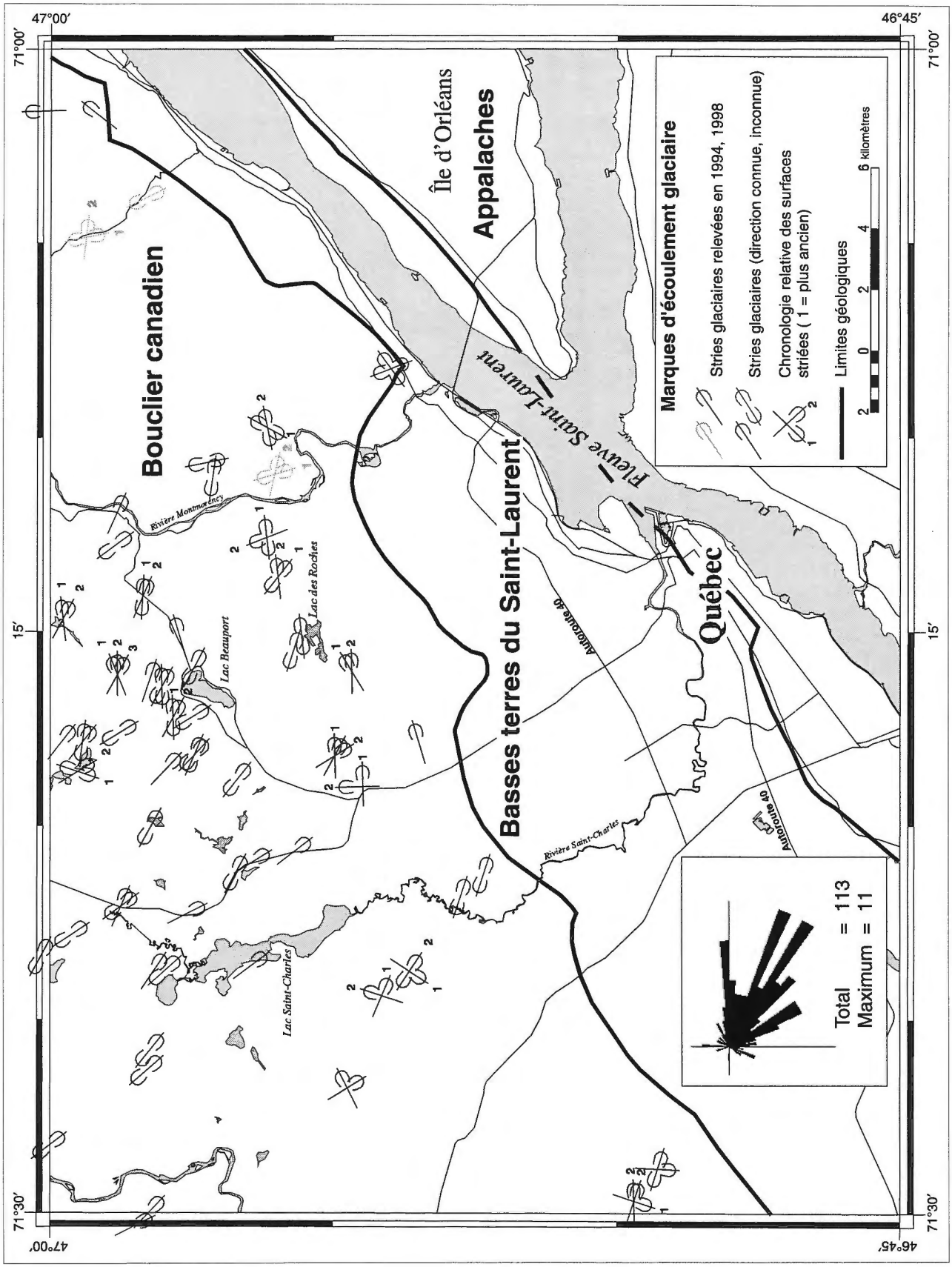

Figure 1. Marques d'écoulement glaciaire.

INTERPRÉTATION DES RÉSULTATS

Les diverses marques d'écoulement glaciaire nous permettent de reconnaître trois phases distinctes d'écoulement glaciaire et deux phases intermédiaires pendant lesquelles se sont produits des réajustements majeurs.

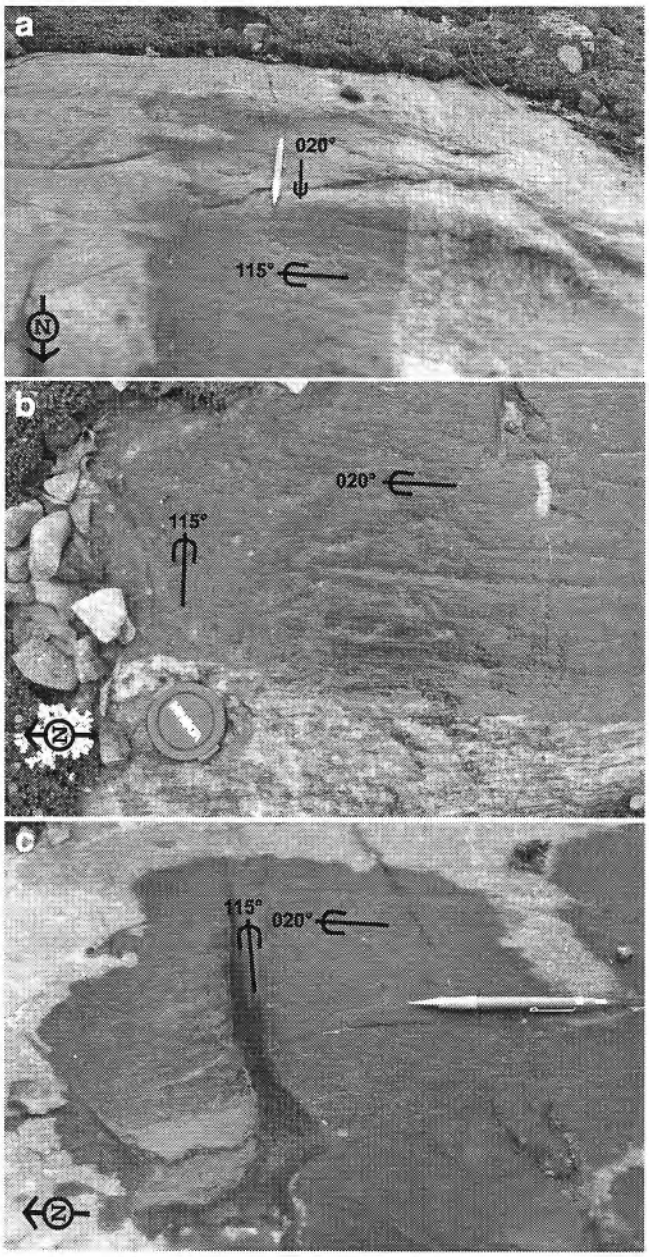

Figure 2. *(**a**) Stries à orientation nord (020°, mouvement récent) superposées sur des microformes profilées aux stries à orientation sud-est (105°–115°). (**b**) Vieille surface aux stries orientées de 105° à 115°, protégée du mouvement récent vers 020°. (**c**) Vieilles stries orientées de 105° à 115° situées dans une zone de fracture et protégées du mouvement récent vers 020°.*

Une première phase d'écoulement glaciaire vers le sud-sud-ouest (figure 3, écoulement ancien) est plus ou moins bien représentée localement. Elle est antérieure à tous les autres mouvements et pourrait être mise en corrélation avec la phase de croissance de l'Indlandsis laurentidien au Wisconsinien inférieur. Elle pourrait être la contrepartie sud-ouest du centre d'englacement situé au sud-ouest de Churchill Falls, dont l'existence a été proposée par Klassen et Bolduc (1984) pour expliquer un écoulement ancien vers le nord-est au Labrador central et par Parent et Paradis (1997) pour expliquer un mouvement vers le nord-ouest dans la région d'Ashuanipi.

Ce mouvement a été suivi au pléniglaciaire par une deuxième phase d'écoulement glaciaire vers le sud-est (figure 3 : écoulement vers le sud-est), qui a suivi la formation d'une ligne de partage des glaces dans le secteur de Némiscau (Paradis et Boisvert, 1995; Parent et al., 1995). Cette phase pourrait être mise en corrélation avec le maximum glaciaire du Wisconsinien inférieur.

Au Wisconsinien supérieur et suivant la formation d'un courant glaciaire (Parent et Occhietti, sous presse) dans la dépression occupée présentement par le fleuve Saint-Laurent, il y a eu réajustement de l'écoulement glaciaire du sud-est vers l'est (figure 3, réajustement causé par le courant glaciaire). Les stries glaciaires associées à la période active de ce courant de glace s'incurvent vers le nord-est jusqu'à environ 70°, suivant en partie la topographie du corridor actuel du fleuve. La présence de ce courant glaciaire a régi en grande partie l'histoire de la déglaciation du secteur de Québec en entraînant l'amincissement accéléré de la glace tant sur les hautes terres laurentiennes et appalachiennes que dans la vallée du Saint-Laurent jusqu'à Québec (Parent et Occhietti, sous presse). Cet amincissement de la glace a donné lieu à la formation de la baie de vêlage qui, en scindant la glace dans le corridor qu'occupe actuellement le fleuve, a entraîné un deuxième réajustement de la direction de l'écoulement des glaces laurentidiennes, soit de l'est-nord-est vers l'est, puis vers l'est-sud-est et enfin vers le sud-est (figure 3, réajustement causé par la formation de la baie de vêlage).

Ces réajustements de la direction de l'écoulement glaciaire ont été suivis au tardiglacaire par un écoulement de la glace vers le nord, comme en témoignent les stries glaciaires reconnues jusque sur le piémont laurentien dans le secteur du lac Saint-Charles et du lac des Roches (figure 3, écoulement tardiglaciaire vers le nord).

Grâce à l'étude comparative du relief élevé des Laurentides (de 300 à 500 m au-dessus du niveau de la mer) sur la rive nord et de celui du piémont appalachien (de 150 à 200 m au-dessus du niveau de la mer) sur la rive sud, il nous est possible de formuler l'hypothèse suivante : dans la zone de recharge à relief élevé du secteur laurentien, l'amincissement général de la glace par le courant glaciaire aurait été la cause principale de sa perte de vélocité, ce qui aurait permis à la glace appalachienne de s'étendre jusqu'au piémont laurentien. Ce dernier mouvement serait alors mis en corélation avec une avancée des glaces appalachiennes au Wisconsinien supérieur dans le secteur de Québec.

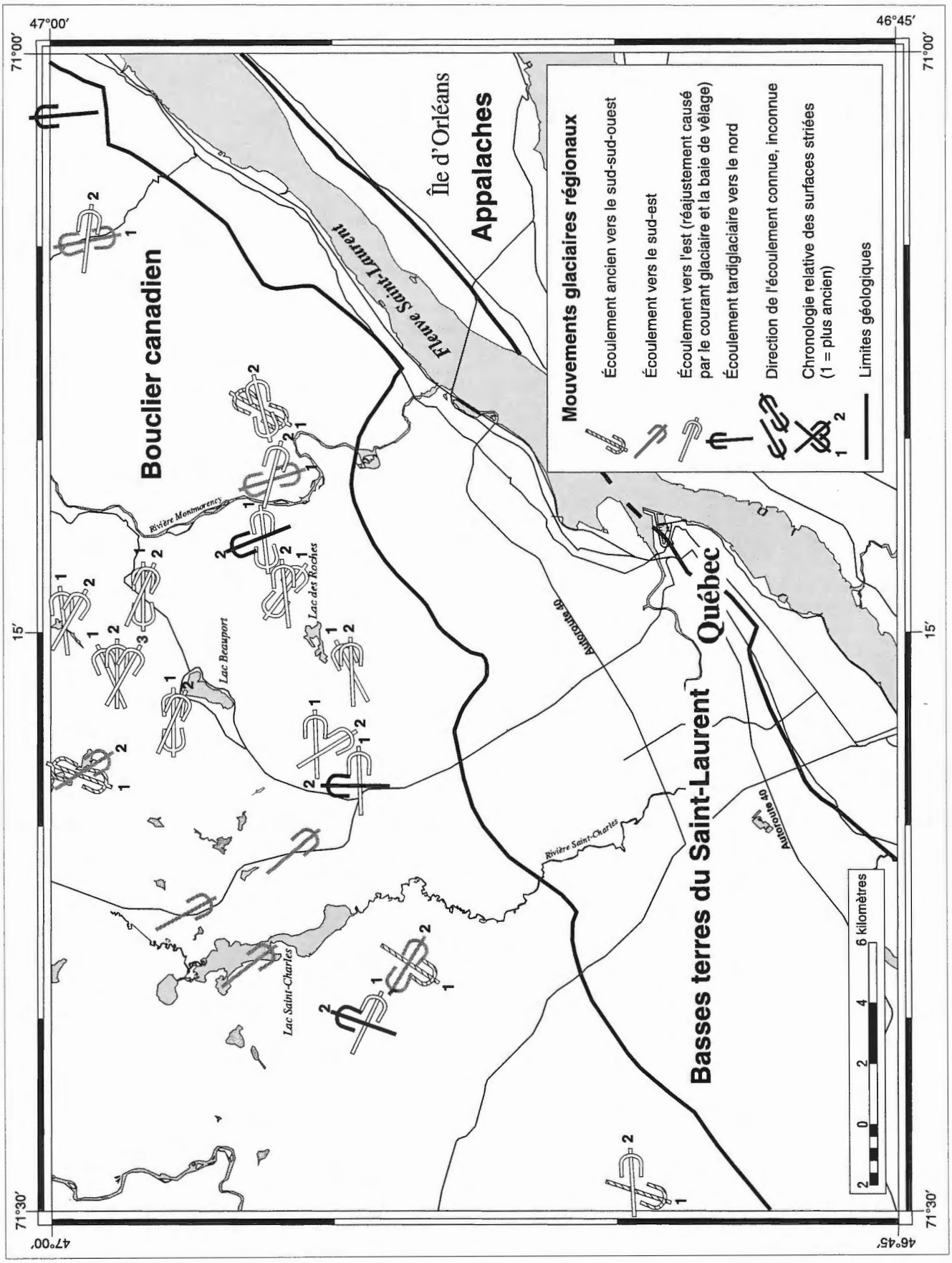

Figure 3. Mouvements glaciaires régionaux.

DISCUSSION

Les données préliminaires de la présente étude ne permettent certainement pas de formuler des hypothèses sur les relations lithostratigraphiques des sédiments et les différents mouvements glaciaires reconnus dans le secteur. La mise en carte prévue des formations superficielles apportera sans doute des solutions à ce problème. Le relevé a permis de mettre à jour la succession d'événements glaciaires proposée par Chauvin et al. (1985) et LaSalle (1989), tout en tenant compte des nouvelles données et interprétations.

Ainsi, la présente étude a permis de reconnaître deux points majeurs, soit l'importance du mouvement glaciaire récent vers le nord au niveau de son extension jusqu'aux environs du piémont laurentien, soit l'importance des phases de réajustement de la marge glaciaire pendant l'épisode du courant glaciaire et éventuellement lors du développement subséquent de la baie de vêlage.

La nouvelle hypothèse, basée sur la reconnaissance de marques témoignant d'un écoulement glaciaire vers le nord, pourrait entraîner une réinterprétation des données lithostratigraphiques de la région de Québec. La reconnaissance de ce mouvement tardiglaciaire permettra peut-être de mieux comprendre les dépôts morainiques situés dans le secteur du lac Saint-Charles, communément appelés «moraine du lac Saint-Charles» (LaSalle, 1989). Dans ce nouveau contexte d'interprétation, puisqu'on sait que les glaces se sont déplacées vers le nord jusque dans ce secteur, il pourrait s'avérer nécessaire de réinterpréter le dépôt de la moraine elle-même. Les indices d'un mouvement glaciaire vers le nord dans le secteur du piémont laurentien et la cartographie détaillée des formations superficielles devraient permettre de mieux comprendre l'ensemble de la dynamique glaciaire au Wisconsinien, y compris le style de déglaciation avec courant glaciaire et/ou baie de vêlage, style qui est proposé actuellement pour l'estuaire du Saint-Laurent.

D'autres écoulements glaciaires vers le nord en provenance des Appalaches se sont probablement produits avant celui qui est documenté ici. En effet, les grandes glaciations quaternaires ayant été cycliques, le scénario proposé ici a pu se produire antérieurement. Lors de travaux futurs, il faudra établir avec soin la chronologie des phases d'écoulement glaciaire à chaque site d'observation, afin de reconnaître ces mouvements glaciaires anciens.

CONCLUSION

Sur la foi des nouvelles observations de septembre 1998 et de l'étude comparative des résultats et de l'interprétation classique du contexte régional de déglaciation (LaSalle, 1989) qui implique une baie de vêlage, on doit envisager une réinterprétation assez importante de la dynamique de la marge glaciaire et de son évolution dans le temps, au Wisconsinien. Il faudra tenir compte du mouvement glaciaire vers le nord nouvellement reconnu lors de futures études au Québec méridional. D'autres travaux devront être entrepris pour mieux définir et comprendre la dynamique de l'Inlandsis laurentidien au Wisconsinien dans le secteur visé par la présente étude.

REMERCIEMENTS

La présente étude est une contribution au projet 960001 HD (Séquences quaternaires du piémont laurentien) qu'appuie le Programme d'hydrogéologie régional de la Commission géologique du Canada. La réalisation de ces travaux s'inscrit dans le cadre d'une entente de partenariat entre la Commission géologique du Canada et le ministère de la Défense nationale. Nous remercions sincèrement L. Dubé, R. Boivin pour les figures et notamment M. Parent, lecteur critique, pour les discussions et ses commentaires.

RÉFÉRENCES

Chalmers, R.
1898 : Surface geology and auriferous deposits of southeastern Quebec; Geological Survey of Canada, 1898 Annual Report, v. 10, pt J, 160 p.

Chauvin, L., Martineau, G., et LaSalle, P.
1985 : Deglaciation of the Lower St. Lawrence Region, Québec; Geological Society of America, Special Paper 197, p. 111–123.

Clark, T.H.
1937 : Northward moving ice in southern Quebec; American Journal of Science, 5th series, v. 34, p. 22.

Cooke, H.C.
1937 : Further note on northward moving ice; American Journal of Science, 5th series, v. 34, p. 22.

Gauthier, C.
1975 : Déglaciation d'un secteur des rivières Chaudière et Etchemin, Québec; thèse de maîtrise, Université McGill.

Klassen, R.A. et Bolduc, A.
1984 : Ice flow directions and drift composition, Churchill Falls, Labrador; *in* Current Research, Part A; Geological Survey of Canada, Paper 84-1A, p. 255–258.

Lamarche, R.
1971 : Northward moving ice in the Thetford Mines area of southern Quebec; American Journal of Science, v. 271, p. 383–388.
1974 : Southeast, northward, and westward ice movement in the Asbestos area of southern Quebec; Geological Society of America Bulletin, v. 85, p. 465–470.

LaSalle, P.
1985 : Stratigraphie du Quaternaire du Québec : une revue; ministère de l'Énergie et des Ressources du Québec, MB 85-11, 70 p.
1989 : Stratigraphy and glacial history of the Quebec City region; Friends of the Pleistocene, 52nd Annual Reunion, May 19–21, p. 27–70.

LaSalle, P., Martineau, G., et Chauvin, L.
1977 : Dépôts morainiques et stries glaciaires dans la région de Beauce–monts Notre-Dame–parc des Laurentides; ministère des Richesses naturelles du Québec, DPV-515, 22 p.

Lebuis, J. et David, P.P.
1977 : La stratigraphie et les événements du Quaternaire de la partie occidentale de la Gaspésie; Géographie physique et Quaternaire, vol. 31, p. 275–296.

Lortie, G.
1976 : Les écoulements glaciaires intérimaires wisconsiniens dans les Cantons de l'Est et la Beauce, Québec; thèse de maîtrise, Université McGill, 200 p.

Paradis, S.J. et Boisvert, É.
1995 : Séquences des écoulements glaciaires dans le secteur de Chibougamau-Némiscau, Québec; dans Recherches en cours 1995-C; Commission géologique du Canada, p. 259–264.

Parent, M. et Ochietti, S.
sous presse: Late Wisconsinan deglaciation and glacial lake development in the Appalachians of southeastern Québec; Géographie physique et Quaternaire, v. 53.

Parent, M. et Paradis, S.J.
1993 : Interprétation préliminaire des écoulements glaciaires dans la région de la Petite rivière de la Baleine, région subarctique du Québec; dans Recherche en cours, Partie C; Commission géologique du Canada, Étude 93-1C, p. 359–365.
1997 : Mouvements glaciaires polyphasés dans la région d'Ashuanipi (23 F, 23 C et 23 G/w), Moyen-Nord québécois; ministère des Richesses naturelles du Québec, DV 97-03, p. 34.

Parent, M., Paradis, S.J. et Boisvert, É.
1995 : Ice-flow patterns and glacial transport in the eastern Hudson Bay region: implications for the late Quaternary dynamics of the Laurentide Ice Sheet; Canadian Journal of Earth Sciences, v. 32, no. 12, p. 2057–2070.

Veillette, J.J.
1986 : Former southwesterly ice-flows in Abitibi-Témiscamingue: implications for the configuration of the Late Wisconsinan ice sheet; Canadian Journal of Earth Sciences, v. 23, p. 1724–1741.

Commission géologique du Canada Projet 960001 HD

Textural characteristics of rocks that display significant electrical anisotropy[1]

S. Connell, T.J. Katsube, P.A. Hunt, and D. Walker
Mineral Resources Division, Ottawa

Connell, S., Katsube, T.J., Hunt, P.A., and Walker, D., 1999: Textural characteristics of rocks that display significant electrical anisotropy; in *Current Research 1999-D; Geological Survey of Canada, p. 9–15.*

Abstract: Detailed texture analysis by scanning electron microscopy has been carried out on four rock samples (Bathurst mining camp, New Brunswick), which display significant electrical anisotropies (λ = 30:1 to 1300:1). The purpose was to determine the cause of the anisotropy. The electrical resistivity (ρ_r) in the directions parallel and perpendicular to their bedding are in the ranges of 10–1000 Ω•m and 1500–40 000 Ω•m, respectively.

Results indicate that the high ρ_r values for the direction perpendicular to the bedding are mainly due to tight siliceous layers that act as electrical insulators to the traversing electrical current. The low ρ_r values for the direction parallel to the bedding are mainly due to sulphide mineral concentrations or combinations of sulphide and clay mineral grains within certain layers, displaying good and continuous interconnection of the electrical conductive grains. The high λ values are mainly a result of large variations in ρ_r for the direction perpendicular to the bedding.

Résumé : Des analyses de texture détaillées réalisées par microscopie électronique à balayage sur quatre échantillons de roche (camp minier de Bathurst, Nouveau-Brunswick) qui présentent d'importantes anisotropies électroniques (λ = 30/1 à 1 300/1). L'objectif de ces analyses consiste à déterminer la cause de cette anisotropie. La résistivité électrique (ρ_c) dans les directions parallèle et perpendiculaire à la stratification s'inscrit respectivement dans les intervalles de 10 à 1 000 Ω•m et de 1 500 à 40 000 Ω•m.

Les résultats indiquent que les valeurs élevées de ρ_c pour la direction perpendiculaire à la stratification s'expliquent essentiellement par la présence de couches siliceuses compactes qui agissent comme isolants électriques pour les courants électriques présents. Les valeurs faibles de ρ_c pour la direction parallèle à la stratification sont attribuables principalement à des concentrations de minéraux sulfurés ou d'associations de grains de minéraux sulfurés et argileux au sein de certaines couches, lesquelles permettent une interconnexion efficace et continue entre grains électriquement conducteurs. Enfin, les valeurs élevées de λ sont dues pour l'essentiel à des variations importantes de ρ_c dans la direction perpendiculaire à la stratification.

[1] Contribution to the 1994-1999 Bathurst Mining Camp, Canada-New Brunswick Exploration Science and Technology (EXTECH II) Initiative

INTRODUCTION

Detailed texture analysis by scanning electron microscopy (SEM) has been carried out on four rock samples from the Bathurst mining camp (New Brunswick; Table 1) which display significant electrical anisotropies. The purpose was to determine the cause of these anisotropies. Since the first electrical anisotropies of relevance have been reported in 1996 (Katsube et al., 1996a, b; Jones et al., 1996), subsequent studies in the Bathurst region have also identified such characteristics. Some have displayed anisotropies (λ) as large as 1300:1 (Katsube et al., 1997), with electrical resistivities of 10 Ω•m in one direction and 13 000 Ω•m in the other (Table 2). These are clearly extremely large differences, with the lower value well within the detection limits of airborne electromagnetic systems and the other outside those limits. Many rock samples with relevant but with smaller λ values in the range of 10:1 to 400:1 (Katsube et al., 1998a, b, c; Connell et al., 1998), have also been reported. The four samples used in this study have λ values in the range of 30:1 to 1300:1. The purpose of this paper is to document the relationship that has been observed between the rock texture and the electrical resistivity (ρ) and anisotropy (λ) values.

METHOD OF INVESTIGATION

Samples and sample preparation

The four samples selected for this study displayed large electrical anisotropy values and were collected from various regions in the Bathurst mining camp (New Brunswick). One of the four samples is from the Brunswick No. 12 deposit (Katsube et al., 1997). The other three samples are from a regional sample set collected near various deposits in the same area (Katsube et al., 1998a). Information on drill hole identification, sample depth, formation, and lithology are listed in Table 1.

These samples were cut into rectangular shapes, with one side cut generally parallel to the bedding and the other two across the bedding. First, a detailed visual examination was performed and the key features were recorded, as shown in the block diagrams of Figures 1, 2, 3 and 4 (the left side of each figure). Then, relevant surfaces of these samples which best represented features of significance were polished and prepared for scanning electron microscope (SEM) analyses. The SEM analysis allowed a close examination of the sample mineralogy, texture, and fabric, including the connectivity of the sulphide and other mineral grains.

Table 1. Sample identification for samples collected for this study.

Sample number	Drill hole	Depth (m)	Fm.	Lithology
X-12-3a	5175	44.35		Chloritic Iron-formation
MXG-13A	B357	434.64	NF	Iron-formation
MXG-20	HORB96-12	347.84	BB	Shale-schist
MXG-2	H55	45.11	SL	Felsic volcanic

SL= Spruce Lake Formation
NF=Nepisiguit Falls Formation
BB=Boucher Brook Formation

Table 2. Results of electrical resistivity measurements.

Sample	Rock type	δ_B (g/mL)	Mean ρ_r, (10^3 Ωm) α	β	γ	Anisotropy λ
X-12-3a	IF	3.34	13.02	0.0082*	0.0015*	1300:1
MXG-13A	IF	4.1	21.26	0.072		295:1
MXG-20	Sh.	2.98	1.65	0.046		35.8:1
MXG-2	FV	2.85	42.75	1.05		40.7:1

ρ_r = Bulk electrical resistivity
δ_B = Bulk density (g/mL)
* = Possible reduction in measurement accuracy due to distortion of the complex resistivity plots (arcs). ρ_r is too low for an accurate measurement.
FV = Felsic volcanic
IF = Iron-formation
Sh. = Shale-schist

Image analysis procedure using scanning electron microscope

A Leica/Cambridge S-360 scanning electron microscope (SEM), Oxford/Link eXL-II energy dispersive X-ray analyser, was used for this study. Operating conditions for the SEM were generally 20 kV accelerating voltage and 25 mm working distance. Backscattered electron images were transferred from the SEM to a online PC where '.tif' format image files were captured. The .tif files were then imported into an image analysis program called 'UTHSCSA Image Tool'. This program was developed at the University of Texas Health Center at San Antonio, Texas. In this program the software detected the presence and location of each feature or object within the assigned minimum-maximum thresholds. With each feature or object identified, the program counted and preformed a variety of geometric measurements. This data was then imported into a spreadsheet program where plots of the results were produced.

ANALYTICAL RESULTS

The visual description of sample X-12-3 is displayed in the left-hand section of Figure 1. Below it, is shown the directions of the electrical resistivities (ρ_r), with 10 Ω•m in the directions parallel to bedding, and 13 000 Ω•m in the direction perpendicular to bedding, implying an electrical anisotropy (λ) larger than 1300:1 (Table 2). This is a chloritic iron-formation containing chlorite, quartz, apatite, iron oxide, pyrite, and minor sphalerite minerals that were identified under the SEM. The apatite and iron oxide are mixed with quartz and form most of the layering visible in hand sample. The SEM images are displayed in the right-hand section of the figure, the upper image representing the top surface of the sample, and the lower representing one of the cross-sections of the sample, as shown by the two arrows. The upper image shows a few very fine-grained, isolated sulphides (bright spots). The lower image displays distinct layering of tight, continuous siliceous layers, some containing isolated or interconnected sulphide grains (bright spots), and others barren of such

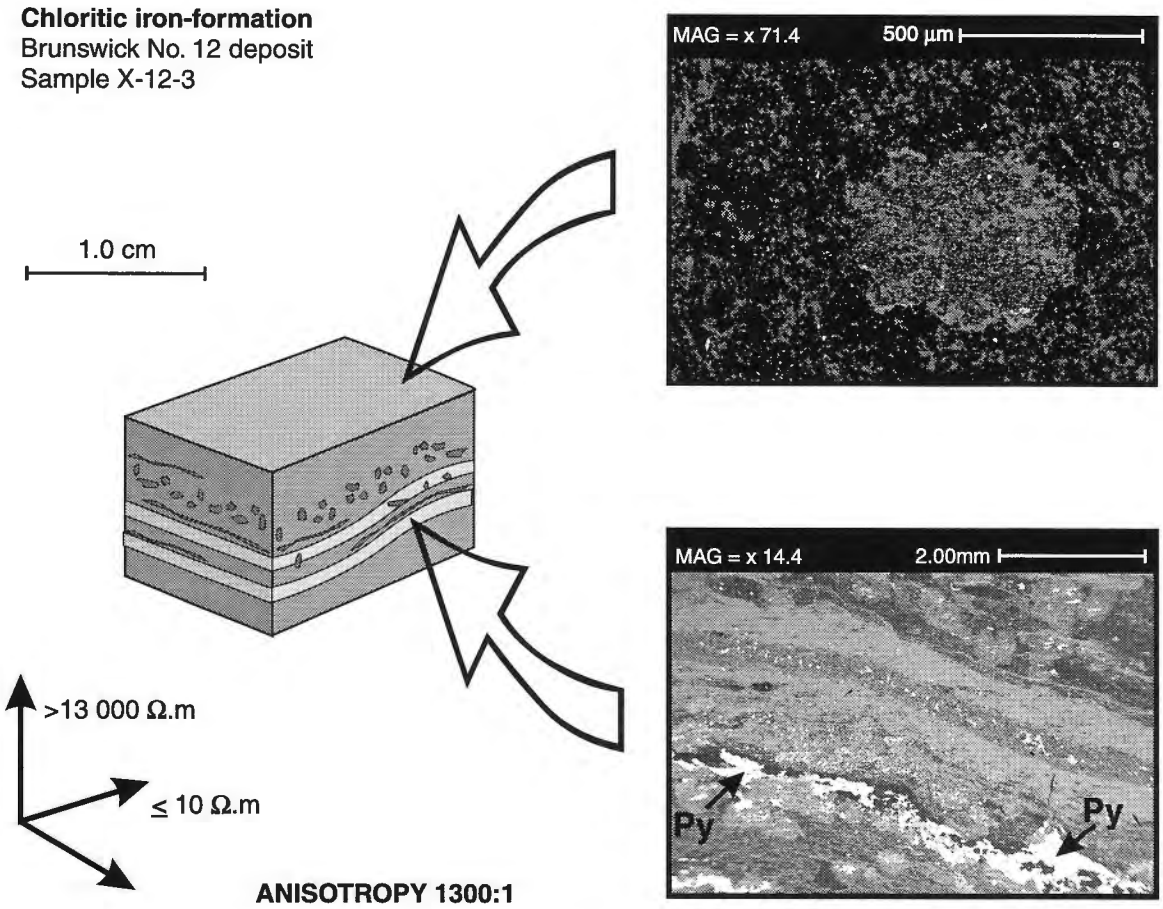

Figure 1. *Visual description (left-hand section) and SEM images (upper and lower right-hand section) for sample X-12-3, with electrical resistivities (ρ_r) for the three directions and their electrical anisotropy (λ) value (lower left-hand section).*

grains. The layer containing interconnected sulphide grains in the lower section of this image is probably one of the main sources of the very low ρ_r values (<10 Ω•m) in the horizontal direction, or the direction parallel to the bedding of this sample. The tight continuous siliceous layers barren of sulphides likely act as electrical insulators, and are the cause of the extremely high ρ_r values (>13 000 Ω•m) in the direction across or perpendicular to bedding.

The visual description of sample MXG-13a is displayed in the left-hand section of Figure 2. The directions of the electrical resistivities (ρ_r), are shown below the block diagram with 70 Ω•m in the directions parallel to bedding, and more than 20 000 Ω•m in the direction perpendicular to bedding, implying an electrical anisotropy (λ) larger than 300:1. This is also an iron-formation and contains galena, pyrite, quartz, chlorite, manganite, sphalerite, and arsenopyrite minerals that were identified under the SEM. This sample is different from the previous iron-formation sample (X-12-3), as bedding is not as clearly defined and there is a considerably higher sulphide content, as seen in both the upper and lower images. Even though there is no preferred orientation to the sulphide grains, many of them are interconnected and define some of the banding visible in hand sample and in the SEM images. Some of the grain connectivity is visible on both the upper and lower images. This connectivity between the sulphide grains within certain layers is probably the source of the low ρ_r values (<70 Ω•m) in the direction parallel to bedding. However, it is probably not the sulphide content alone that controls the electrical conductivity, because the ρ_r value (<70 Ω•m) of this sample is higher than the previous sample (X-12-3), even though it appears to have a higher sulphide mineral content. It is probably the sulphide grain connectivity that is the main factor. The quartz- and chlorite-rich bands between the sulphide-rich layers, such as the one in the lower section of the lower SEM image of this sample, act as electrical insulators and are the cause of the extremely high ρ_r values (>20 000 Ω•m) in the direction perpendicular to bedding. There is fine-grained galena disseminated throughout the sample but the grains do not appear to be interconnected.

The visual description of sample MXG-20 is displayed in the left-hand section of Figure 3. The directions of the electrical resistivities (ρ_r) are shown below it, with 40 Ω•m in the directions parallel to bedding, and 1500 Ω•m in the direction perpendicular to bedding, implying a λ value larger than 30:1. This sample is a shale-schist with fine quartzitic stringers and disseminated sulphides concentrated along bedding planes. SEM images are displayed in the right-hand section of the figure, the lower representing one of the cross-section surfaces of the sample and the upper representing an enlarged section of the lower image, as shown by the arrows. The mineralogy, identified by the SEM, includes quartz, apatite, pyrite, and

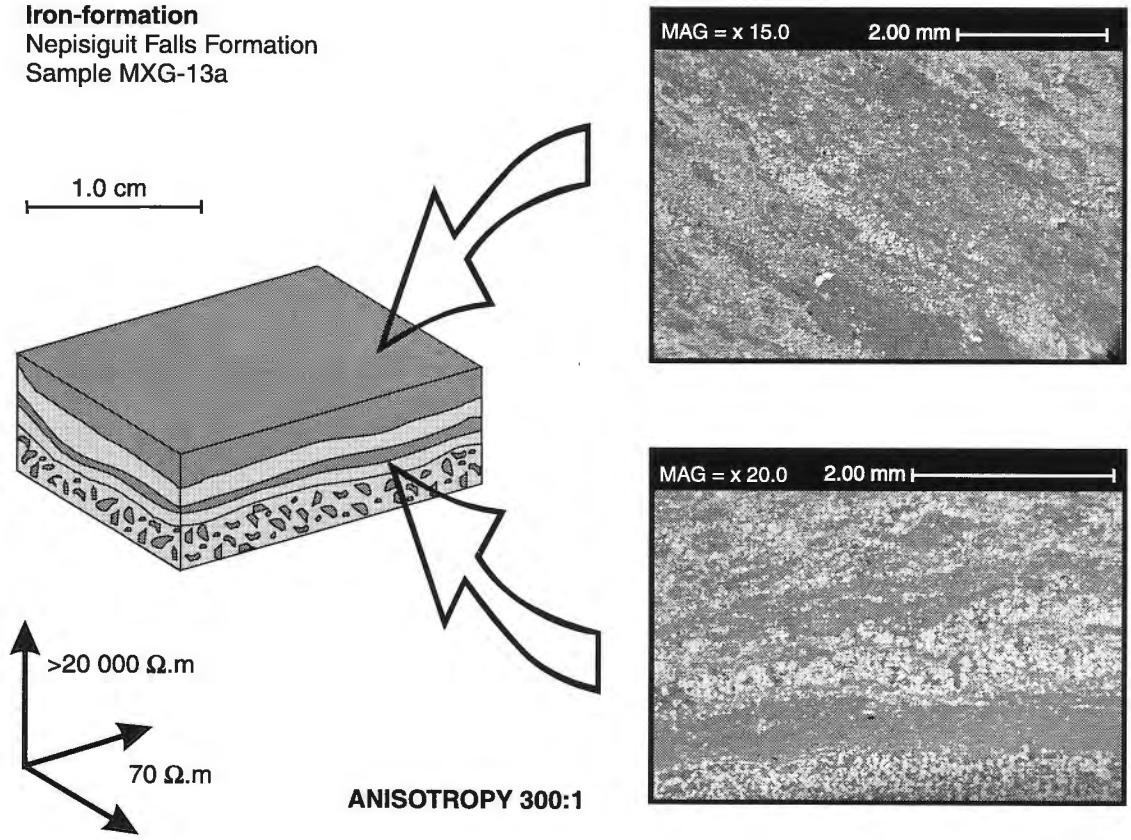

Figure 2. *Visual description (left-hand section) and SEM images (upper and lower right-hand section) for sample MXG-13a, with ρ_r values for the three directions and their λ value (lower left-hand section).*

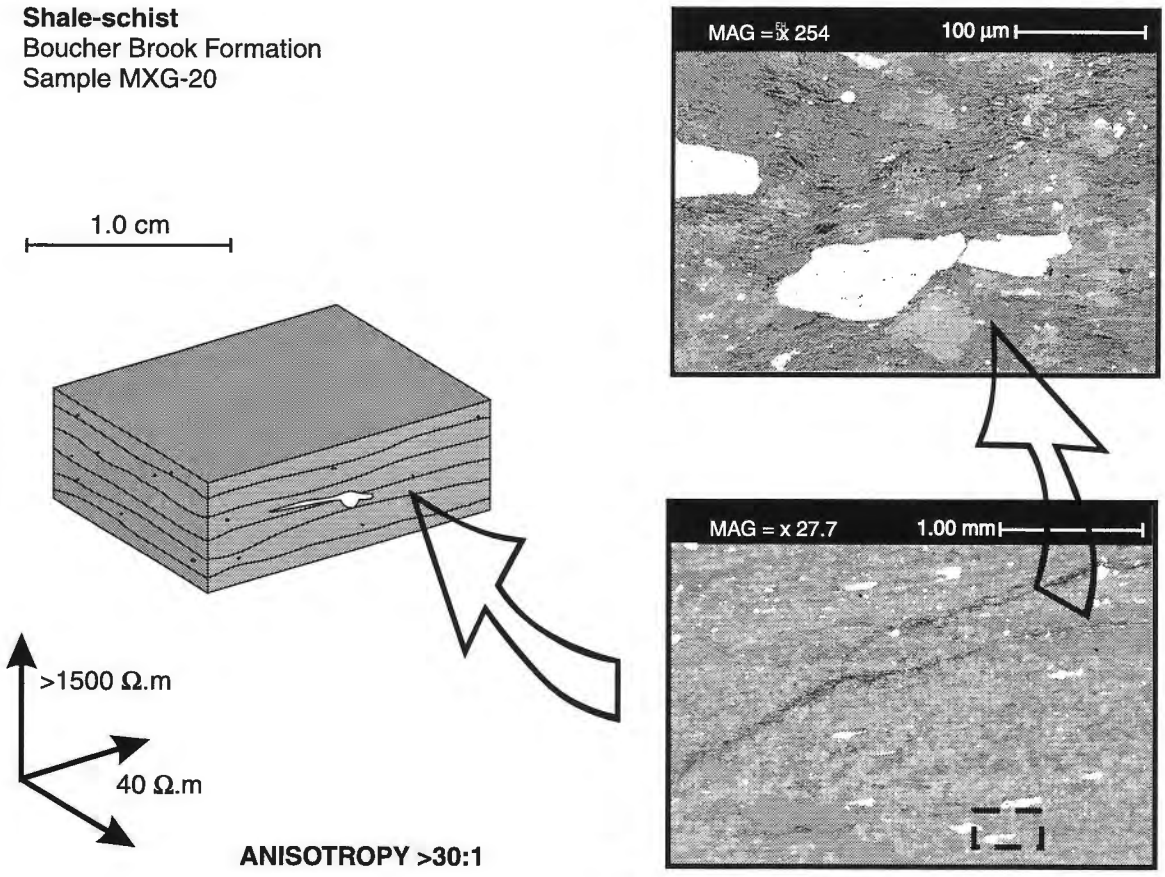

Figure 3. *Visual description (left-hand section) and SEM images (upper and lower right-hand section) for sample MXG-20, with ρ_r values for the three directions and their λ value (lower left-hand section). The upper SEM image is an enlargement of a section of the lower image.*

clay minerals. These images indicate that the sulphide content is low and that fine, blebby pyrite grains (bright spots) are disseminated throughout the rock with less of a concentration compared to the previous cases in this study. These images, however, show an abundance of fine, clay mineral grains (dark-grey plate-like grains) throughout the rock, which are generally aligned parallel to bedding. The larger pyrite grains also tend to be elongated and aligned parallel to bedding. The cluster of these elongated clay and pyrite grains, aligned along the bedding, likely form continuous paths for electrical currents to flow, and are the source of the low ρ_r values (40 Ω•m) in this direction. This implies that, here, the reduced ρ_r values parallel to bedding may be attributed to grain shape and/or orientation and connectivity as opposed to higher concentration of sulphides, as previously was the case. The ρ_r value perpendicular to the bedding is considerably lower (1500 Ω•m) than the two previous cases. This is probably due to the lack of the siliceous layers that likely disrupted the flow of the electrical current in that direction. The smaller λ value for this sample (30:1) is due to the lower ρ_r value perpendicular to the bedding.

The visual description of sample MXG-2 is displayed in the left-hand section of Figure 4. The directions of the electrical resistivities (ρ_r) are shown below it, with 1000 Ω•m in the directions parallel to foliation, and more than 40 000 Ω•m in the direction perpendicular to foliation, implying an electrical anisotropy (λ) larger than 40:1. This sample, a volcanic tuff, is essentially nonmineralized and siliceous. This explains the comparatively high to very high ρ_r values for all directions (1000–40 000 Ω•m). Quartz, monazite, zircon, rutile, apatite, galena, and mafic minerals have been identified under the SEM. These images display shearing and crenulations, along which fine Fe-rich and K-depleted alteration halos are present. The potassic leached zones appear as lighter grey areas on the SEM images. The chemical composition is essentially homogenous with only the Fe and K concentrations varying. Although the direction of the lower ρ_r value coincides with the direction of the shearing, it is not certain whether these slight variations in chemical compositions (Fe and K) are their source.

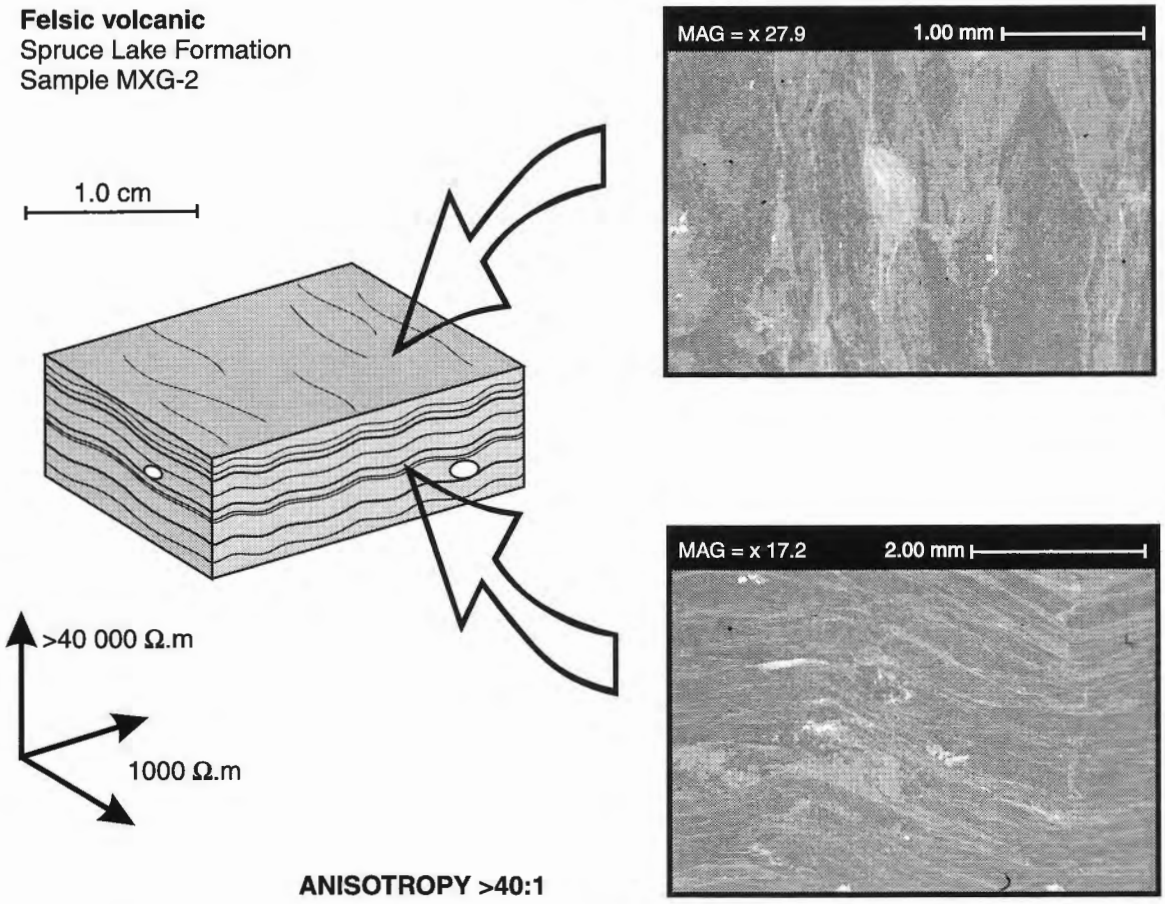

Figure 4. *Visual description (left-hand section) and SEM images (upper and lower right-hand section) for sample MXG-2, with ρ_r values for the three directions and their λ value (lower left-hand section).*

DISCUSSION AND CONCLUSIONS

The electrical anisotropy (λ) values for these four samples (two iron-formation, shale-schist, felsic volcanic) are in the range of 30:1 to 1300:1, and the electrical resistivity (ρ_r) values in the direction parallel and perpendicular to their bedding and/or foliation are in the ranges of 10-1000 Ω•m and 1500-40 000 Ω•m, respectively. Results of intensive examinations by visual and SEM analysis indicate that the very high ρ_r values (13 000–40 000 Ω•m) in the direction perpendicular to the bedding are due to the tight siliceous layers (samples X-12-3, MXG-13a, and MXG-2) that act as electrical insulators to the traversing electrical current. The lower ρ_r value (1500 Ω•m) for that direction is for the shale-schist sample (MXG-20) which has no tight siliceous layers. This indicates the significance of the electrical insulating effect of these layers. Results of the same examinations indicate that the very low ρ_r values (10–70 Ω•m, e.g. samples X-12-3, MXG-13a, and MXG-2) in the direction parallel to bedding are likely due to either sulphide mineral concentrations or a combination of sulphide and clay mineral concentrations within certain layers that are parallel to foliation. These concentrations appear to result in good continuous and interconnected electrical conductors. The higher ρ_r value (1000 Ω•m) in this direction is for sample MXG-2, which does not contain any high concentrations of sulphide or clay minerals. This implies that it does not have any continuous electrical conductors. Scanning electron microscope images for this sample, however, do reveal Fe-rich and K-depleted, thin altered layers along the shearing parallel to the bedding. However, it is not certain whether these features, or what type of mechanisms related to these features might contribute to the ρ_r value of 1000 Ω•m, which is not considered to be low, but is considerably lower than that (ρ_r >40 000 Ω•m) of the perpendicular direction. The moderately large to very large λ values for these samples are mainly a result of the large variation in ρ_r values (1500–40 000 Ω•m) for the direction perpendicular to bedding. The ρ_r variation in the direction parallel to the bedding is generally small (10–70 Ω•m).

ACKNOWLEDGMENTS

The authors are grateful for the critical review of this paper and for the very useful suggestions by P. Keating (Geological Survey of Canada). Thanks are also due to K. Shaw for her constructive comments and suggestions.

REFERENCES

Connell, S., Katsube, T.J., Best, M.E., Goodfellow, W.D., and Mwenifumbo, J.
1998: Electrical characteristics of mineralized and nonmineralized rocks at the Stratmat deposit, Bathurst mining camp, New Brunswick; *in* Current Research 1998-E; Geological Survey of Canada, p. 149–162.

Jones, A.G., Katsube, T.J., and Ferguson, I.
1996: Paleoproterozoic tectonic processes revealed through electromagnetic studies of the North American Central Plains (NACP) conductivity anomaly; from continental to hand sample scale; *in* Society of Exploration Geophysicists Expanded Abstracts with Authors' Biographies, Technical Program, 66th Annual Meeting and International Exhibition; Denver, Colorado, November 10–15, 1996, Volume I, p. 269–272.

Katsube, T.J., Best, M., and Jones, A.G.
1996a: Electrical anisotropy of mineralized and non mineralized rocks: In Society of Exploration Geophysicists Expanded Abstracts with Authors' Biographies, Technical Program, 66rd Annual Meeting and International Exhibition (Denver, November 10-15, 1996), Volume II, p.1279-1281.

Katsube, T.J., Connell, S., Goodfellow, W.D., and Scromeda, N.
1998a: Electrical characteristics of mineralized and nonmineralized rocks from the Bathurst mining camp, New Brunswick; *in* Current Research 1998-E; Geological Survey of Canada, p. 125–137.

Katsube, T.J., Connell, S., Scromeda, N., Goodfellow, W.D., and Best, M.E.
1998b: Electrical characteristics of mineralized and nonmineralized rocks at the Caribou deposit, Bathurst mining camp, New Brunswick; *in* Current Research 1998-D; Geological Survey of Canada, p. 25–35.
1998c: Electrical characteristics of mineralized and nonmineralized rocks at the Restigouche deposit, Bathurst mining camp, New Brunswick; *in* Current Research 1998-E; Geological Survey of Canada, p. 139–148.

Katsube, T.J., Palacky, G.J., Sangster, D.F., Galley, A.G., and Scromeda, N.
1996b: Electrical properties of disseminated sulphide ore samples from Snow Lake; *in* EXTECH I: Multidisciplinary Approach to Massive Sulphide Research in Rusty Lake-Snow Lake Greenstone Belts, Manitoba, (ed.) G.F. Bonham-Carter, A.G. Galley, and G.E.M. Hall; Geological Survey of Canada, Bulletin 426, p. 319–329.

Katsube, T.J., Scromeda, N., Best, M.E., and Goodfellow, W.D.
1997: Electrical characteristics of mineralized and nonmineralized rocks at the Brunswick No. 12 deposit, Bathurst mining camp, New Brunswick; *in* Current Research 1997-E; Geological Survey of Canada, p. 97–107.

Geological Survey of Canada Project 870057

Heavy-metal concentrations in soils surrounding Canadian base-metal smelters: a comparative study[1]

P.J. Henderson, R. Knight, and I. McMartin
Terrain Sciences Division, Ottawa

Henderson, P.J., Knight, R., and McMartin, I., 1999: Heavy-metal concentrations in soils surrounding Canadian base-metal smelters: a comparative study; in *Current Research 1999-D; Geological Survey of Canada, p. 17–26.*

Abstract: Orientation studies in the vicinity of the Horne smelter (Rouyn-Noranda, Quebec) and the Trail smelter (Trail, British Columbia) have provided organic and mineral-soil geochemical analyses that are comparable with data collected previously near the smelter at Flin Flon, Manitoba. Results from Rouyn-Noranda and Trail are similar to those at Flin Flon and indicate that humus is enriched in elements emitted from the smelter. Concentrations are elevated at sites near the smelter and decrease with distance from the source such that the log-distance is inversely proportional to the log-concentration of the emitted element. Factors affecting the degree of enrichment include smelter type, emission characteristics, topography, and wind direction. Heavy-metal concentrations in mineral soils are related primarily to bedrock composition at all locations. In the vicinity of the smelter, downward migration of some smelter-related metals in the soil profile is indicated by the relationship between concentrations in B- and C-horizon mineral soils.

Résumé : Des études d'orientation à proximité des fonderies de Horne (Rouyn-Noranda, Québec) et de Trail (Trail, Colombie-Britannique) ont fourni des données géochimiques sur les sols organiques et minéraux qui sont comparables aux données recueillies antérieurement près de la fonderie de Flin Flon, au Manitoba. Les résultats obtenus à Rouyn-Noranda et à Trail sont semblables à ceux obtenus à Flin Flon et indiquent que l'humus est enrichi en éléments rejetés par l'usine. Les concentrations sont élevées sur les sites situés à proximité de la fonderie et diminuent en s'éloignant de la source, de sorte que la distance logarithmique est inversement proportionnelle à la concentration logarithmique de l'élément émis. Parmi les facteurs influant sur le degré d'enrichissement figurent le type de fonderie, les caractéristiques des émissions, la topographie et la direction du vent. Sur tous les sites, les concentrations de métaux lourds dans les sols minéraux sont liées essentiellement à la composition du substratum rocheux. À proximité de la fonderie, la migration vers le bas de certains métaux émis par ces usines est attestée par la relation entre les concentrations de certains minéraux dans les sols minéraux des horizons B et C.

[1] Contribution to the Metals in the Environment Program

INTRODUCTION

As part of the Metals in the Environment (MITE) program initiated at the Geological Survey of Canada in 1997, a project was undertaken to examine the distribution of trace metals in surficial sediment (both organic and mineral) surrounding the Horne smelter (Rouyn-Noranda, Quebec) and the Trail smelter (Trail, British Columbia). It has long been known that metal smelters are point sources of heavy-metal loading with concentrations decreasing with distance from the source (Davies, 1983). This distribution pattern has been mapped in

Table 1. Comparison of parameters at three Canadian smelters.

	Rouyn–Noranda, Quebec	Trail, British Columbia	Flin Flon, Manitoba
Commenced	1927	1916	1930
Company	Noranda	Cominco	Hudson Bay Mining and Smelting
Smelter type	Cu, Zn	Pb, Zn	Cu, Zn
Stacks - number	2	52 (1 major)	1
- height	161 and 130 m	122 m	251 m (since 1974 and 2 at 76 and 46 m prior to that date)
Production	Cu, Se, Ag, Au, Te, Pt and Pd concentrate, $CuSO_4$, $NiSO_4$	Zn, Pb, Ag, Au, Cd, Bi, In, Ge concentrate, GeO_2, $CuSO_4$, CuAsO, sodium antimonate, sulphur products, agricultural fertilizers	Zn, Cu, Cd, Pb concentrate, Au, Ag, Se and Te byproducts
Known stack metal emissions	Ag, As, Cd, Cu, Hg, Pb, Zn	Ag, As, Cd, Cu, Hg, Pb, Zn	Ag, As, Cd, Cu, Fe, Hg, Pb, Zn
Major controls on distribution pattern	Wind (N, NE, E, SE), distance from smelter	Wind , topography, distance from smelter	Wind (SE,SW,NW,N,S), distance from smelter
Ecozone	boreal forest	cordilleran	boreal forest
Relief	Low – Shield terrane	high – 600 m	low – Shield terrane/ carbonate platform
Vegetation	mixed deciduous/coniferous	coniferous montane forest	mixed deciduous/coniferous
Bedrock geology	Abitibi greenstone belt-Archean metasedimentary and metavolcanic rocks and associated intrusions	Pre-Pennsylvanian to Eocene sedimentary and volcanic rocks with granitoid intrusions, metamorphosed	Flin Flon greenstone belt-Proterozoic metasedimentary and metavolcanic rocks and associated intrusions
Surficial geology	Extensive clay plain developed below ~300 m elevation. Large areas of glaciofluvial sand and gravel deposits	Thick deposits of sand, silt and gravel form terraces within major river valleys (i.e. Columbia River). Till and colluvium mantles bedrock at higher elevations	Shield: thin and discontinuous glacial and glaciolacustrine deposits Paleozoic carbonate platform: thick, continuous, glacial and glaciolacustrine deposits
Other anthropogenic influences	Extensive urban development; industries; farming; mining, and exploration; smelting; logging; forest fires	Extensive urban development within valleys; fertilizer plant; logging; pulp mills; forest fires; quarrying	Mining and mining exploration, lumbering, forest fires; minor urban development
Soil development	Good podzolic and brunisolic soil profiles developed on till	Good podzolic and brunisolic soil profiles in till, glaciofluvial and fluvial sediment	Good podzolic and brunisolic soil profiles developed on till
Humus development	Varies with distance from smelter and human interference; good, well decomposed, 2–10 cm thick	Poor, 0–3 cm thick, poorly decomposed, commonly absent	Varies with distance from smelter; generally good, well decomposed, 2–10 cm thick

foliage (Freedman and Hutchinson, 1980), organic and surface mineral soils (Hogan and Wotton, 1984; McMartin et al., 1996; Henderson et al., 1998), and peat (Azzaria and Frechette, 1987; Zoltai, 1988; Dumontet et al., 1990). The main objectives of this study encompass more than simply mapping the dispersal patterns, but include 1) an examination of the nature and fate of airborne smelter emissions in the terrestrial environment, 2) an evaluation of factors (i.e. weathering, soil texture, composition, organic content, etc.) affecting heavy-metal distribution in soil profiles in contaminated areas, 3) the development of criteria for distinguishing between anthropogenic and geogenic heavy-metal enrichment in soils as an aid to mineral exploration and environmental studies, and 4) the calculation of a mass balance relating historical emissions of heavy metals from individual smelters to concentrations retained within the surficial environment. In this paper, we will present some of the initial results from fieldwork conducted in the first year of the project. Results will be compared with earlier studies on soils in the vicinity of the base-metal smelter at Flin Flon, Manitoba (Henderson and McMartin, 1995; Henderson, 1995; McMartin et al., 1996, in press; Henderson et al., 1998).

The three smelters differ in many aspects relevant to soil geochemistry (Table 1). As well as the factors indicated in the table, the complexes have also undergone changes through the history of the operations in order to streamline processing and comply with changing environmental standards. As a result, particulate emissions at all facilities have decreased in the past 5–10 years. Concentrations present in the soil today essentially represent the cumulative record of loading from mining, smelting, and other anthropogenic influences in the areas.

METHODS

Field procedures

The program involved an initial orientation study in the vicinity of both the Horne and Trail smelters, in order to assess both sampling and analytical strategies. Approximately 20 sites were sampled in the vicinity of each smelter, with sites varying in distance from the stack, up to 70 km, along two transects. At each site, a 50–100 g bulk humus sample was collected in addition to 3–5 kg samples of B-horizon (5–15 cm depth, directly below H or A horizon) and C-horizon mineral soil (approximately 90–100 cm depth). The soils were collected from hand-dug pits or excavated sections, and till was the preferred sample medium. Humus was collected from directly over or adjacent to the mineral-soil sampling site. Although the well decomposed, dark organic part of the soil horizon (H) was preferentially sampled, partially decomposed forest litter and mineral soil (Ah) constituted part of the sample at some sites due to variations in the thickness and development of the organic horizon.

In addition to the transect samples, four detailed soil profiles were taken at various distances from the smelters in order to examine the vertical distribution of elements and to resolve differences between 'natural' soil-forming processes from those affected by smelter fallout. At these sites, the litter fall (L), bulk humus (H), and top and bottom half of the total humus layer were collected, as well as the Ah and Ae horizon (if appropriate), the B-horizon at 5 cm intervals to approximately 40 cm depth, and the C-horizon at 10 cm intervals to approximately 100 cm depth. Bulk humus was collected for density measurements. This aspect of the project will not be discussed in this paper.

Analytical procedures

Litter fall and humus samples were air-dried. Litter fall was pulverized and all humus samples were dry sieved to separate the >0.425 mm, <0.425 mm, and <2mm fractions. For mineral soils, the <0.002 mm (clay-size) fraction of till and other sediment was extracted by centrifuge and decantation, where appropriate (Lindsay and Shilts, 1995). The <0.063 mm (silt and clay) and <2 mm fractions were also separated by dry sieving using stainless-steel sieves.

All size fractions of organic and mineral soils were analyzed geochemically for a suite of elements using inductively coupled plasma atomic-emission spectrometry (ICP-AES), following nitric-aqua regia digestion by Chemex Labs, Mississauga, Ontario. In addition, the <2 mm fraction of organic and mineral soils was analyzed by neutron activation (INAA) by ACTLABS, Ancaster, Ontario; the <2 mm fraction of organic soils by ICP-AES, following a sodium

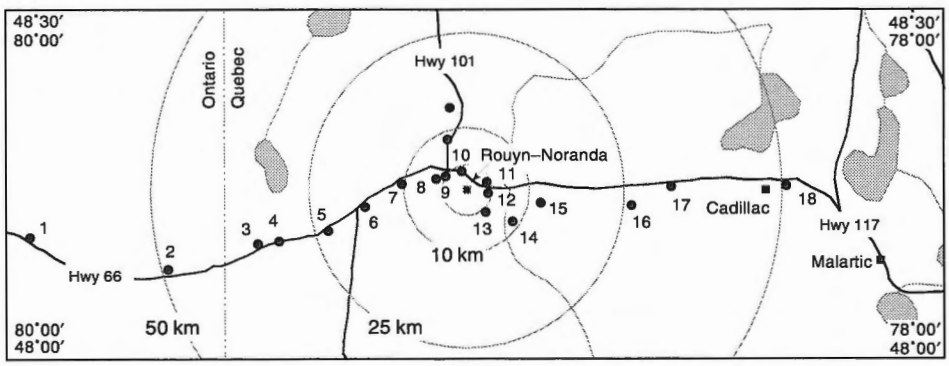

Figure 1. *Transect site locations, Rouyn-Noranda, Quebec.*

pyrophosphate leach (Hall et al., 1996); the <2 mm fraction of mineral soils by ICP-AES, following a total leach ($HF-HClO_4-HnO_3-HCl$). The total organic content (% LOI) of all analyzed fractions of both organic and mineral soils was determined by weight loss on ignition following the method outlined in Sheldrick (1984). The pH was measured on the <2 mm fraction of both organic and mineral soils using $CaCl_2$ (Sheldrick, 1984). Analyses of duplicate samples and laboratory standards were used to monitor analytical accuracy and precision. Grain-size analyses of all mineral soils will also be completed in the upcoming year.

RESULTS

In order to compare the soil and humus geochemical analyses from this study with earlier work carried out near Flin Flon, Manitoba (Henderson et al., 1998; McMartin et al., 1996, in press), only results of ICP-AES analyses (nitric–aqua regia digestion) of the <0.425 mm fraction of humus, and the <0.002 mm fraction of mineral soils will be discussed. The <0.063 mm fraction will also be used in comparing the Horne and Trail smelters, since a large number of sites in both areas were underlain by sandy material lacking a significant clay-sized fraction.

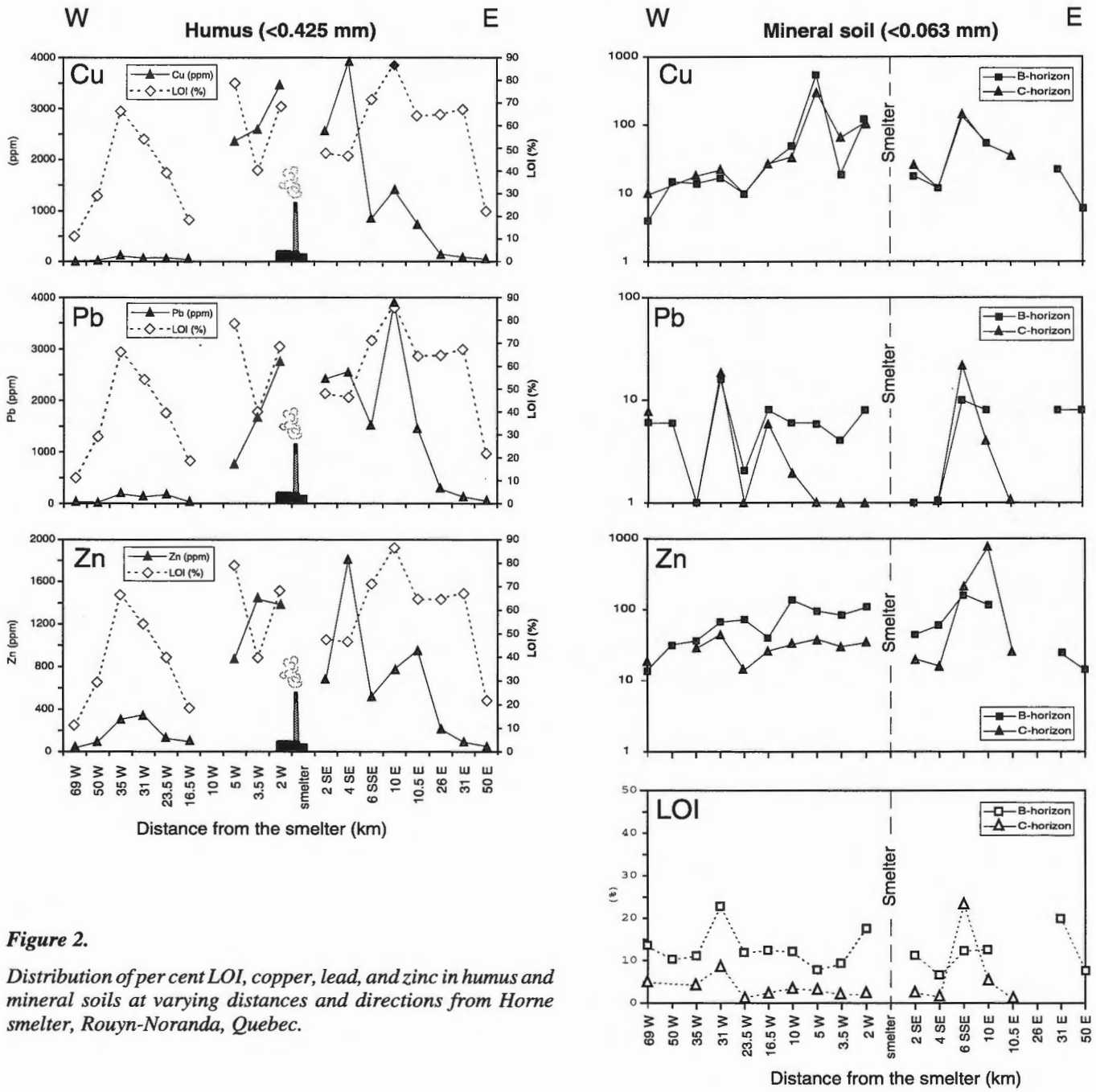

Figure 2.

Distribution of per cent LOI, copper, lead, and zinc in humus and mineral soils at varying distances and directions from Horne smelter, Rouyn-Noranda, Quebec.

Horne smelter — Rouyn-Noranda, Quebec

Characteristics of the copper-zinc smelter (Horne smelter) located in Rouyn-Noranda, northwestern Quebec (lat. 48°13′N; long. 70°00′W) are summarized in Table 1. The smelter is situated within the Abitibi greenstone belt, an area that is highly prospective for gold and base metals. Numerous mines have operated within the region since the first copper deposit was discovered in 1911 and active mineral exploration continues today. It is important to note that both the Horne and Flin Flon smelters are situated in greenstone belts within the boreal forest ecozone. In these respects, among others, they are quite different from the Trail facility.

In September 1997, samples were collected at 20 sites within a 70 km radius of the Horne smelter (Fig. 1). An attempt was made to position sites in wooded areas removed from the direct effects of localized anthropogenic influences (i.e. roads, abandoned mine sites, small processing factories, agricultural areas). The sites are located along two transects extending west and east from the smelter. The western transect includes 10 sites located up to 69 km from the point source (Sites 1–10); the eastern, 8 sites extending 50 km from the smelter (Sites 11–18)(Fig. 1). The two additional sites are situated north of the facility and will not be discussed in this paper. Diamicton (till) was the main mineral soil sampled along the western transect; sand and clay make up a high proportion of samples from the eastern transect.

The distribution of copper, lead, and zinc in the various sample media and the organic content (% LOI) of the soils is shown in Figure 2. For these elements, total concentrations in humus are high at sites adjacent to the smelter and appear to level off at distances beyond 17 km on the western transect and 26 km on the eastern. Values beyond these distances may continue to be elevated in relation to background concentrations for the region, but an accurate background determination cannot be made from the limited number of samples collected. Along the eastern transect, concentrations near the smelter display considerable variation, deviating from the expected decline with distance seen at Flin Flon and other areas (Freedman and Hutchinson, 1980). No explanation can be offered without more detailed examination; however, correlation coefficients indicate little relationship between total concentrations of copper, lead, and zinc, and the organic content (% LOI) of humus (Cu = 0.29; Pb = 0.49; Zn = 0.34).

In mineral soils (Fig. 2), total copper values in both soil horizons tend to be higher within 10 km of the smelter than beyond. Concentrations of C-horizon samples generally equal or exceed those of the B-horizon, with a few exceptions at sites within 10 km of the smelter along the western transect. Correlation coefficients suggest the distribution pattern of copper is poorly related to the organic content of the soils (% LOI) (B-horizon = 0.34; C-horizon = 0.31). Organic contents do not vary significantly over the range of copper concentrations in the soils and the enrichment observed in both B- and C-horizon samples collected within 10 km of the smelter is not matched by an increase in organic content over those samples collected at greater distances (with one exception). This suggests the enrichment is due to other factors, possibly or partly through downward migration of metals from the contaminated humus, although earlier studies in the area by Dumontet et al. (1992) indicate that smelter-related trace metals do not accumulate significantly in the soil profile beyond a depth of 15 cm. Therefore, enriched C-horizon samples represent essentially uncontaminated sediment, and it can be postulated that the enrichment near Rouyn-Noranda is related primarily to bedrock mineralization.

No similar pattern of enrichment is evident in the distribution of lead in mineral soil. For lead, B-horizon concentrations tend to exceed those of the C-horizon along the western transect at sites within 17 km from the smelter, the area with elevated lead concentrations in humus. This suggests downward leaching from humus. At sites along the eastern transect, a different relationship is observed. There, concentrations in C-horizon samples equal those of the B-horizon adjacent to the smelter. High copper, lead, and zinc concentrations in both B- and C-horizon samples collected 6 km south-southeast from the smelter are likely due to mineralization, since several sulphide-rich boulders were observed at the site, although the per cent LOI for C-horizon soil is also high at that site. For zinc, total concentrations in B-horizon soils exceed those of the C-horizon for most transect sites. Adjacent to the smelter the difference in concentration between the two horizons is more pronounced, and enrichment in B-horizon samples is evident within 16 km of the smelter along the western transect. This is indicative of smelter contamination, as discussed above. Beyond 30 km west and approximately 6 km east of the smelter, B-horizon concentrations approach or become less than those in the C-horizon. The enrichment in C-horizon samples from 6 km south-southeast and, most likely, 10 km east of the smelter is related to bedrock mineralization.

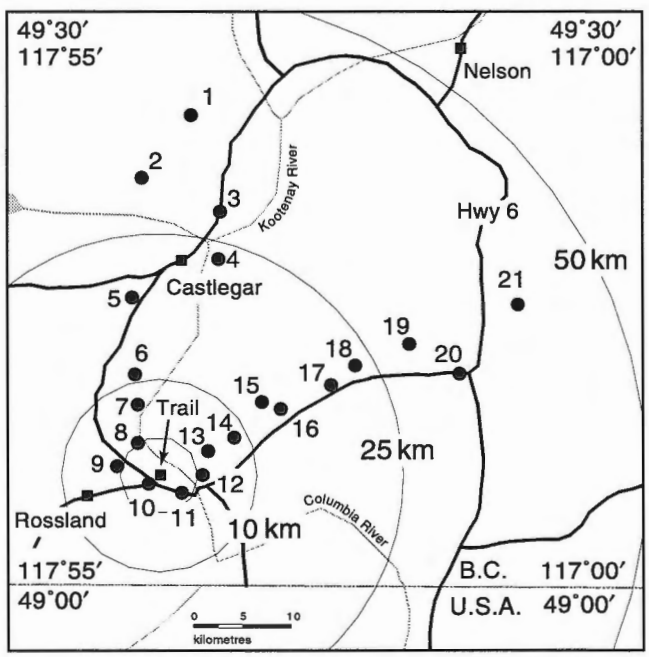

Figure 3. *Transect site locations, Trail, British Columbia.*

Trail smelter — Trail, British Columbia

Trail, British Columbia (lat. 49°06.5′N; long. 117°42′W) has been the site of a major lead-zinc smelter since 1916, although a gold and copper smelter was in operation as early as 1896 (Table 1). The city is located in the southern Kootenay mountains, on the banks of the Columbia River, and the topography is a major factor in controlling the distribution of atmospheric emissions in the area. Deep and steep-sided valleys channel air flow north, south, and southeast.

In October 1997, samples were collected at 21 sites within a 50 km radius of the Trail Operations (Fig. 3). Sites were sampled at all elevations, depending on road access, and are located along two transects extending north and northeast from the point source. The northern transect includes 10 sites located up to 38 km from the smelter (sites 1–10); the northeastern, 11 sites extending 42 km from the smelter (Sites 11–21). Sand or sandy diamicton (till) was the main mineral soil sampled along the northern transect; diamicton (till) makes up a high proportion of samples from the northeastern transect, although sand was collected at some sites at lower elevations. Because humus was generally poorly developed in the area, a decision was made to also collect the organic-rich upper part of the soil horizon (A-horizon) (0–5 cm).

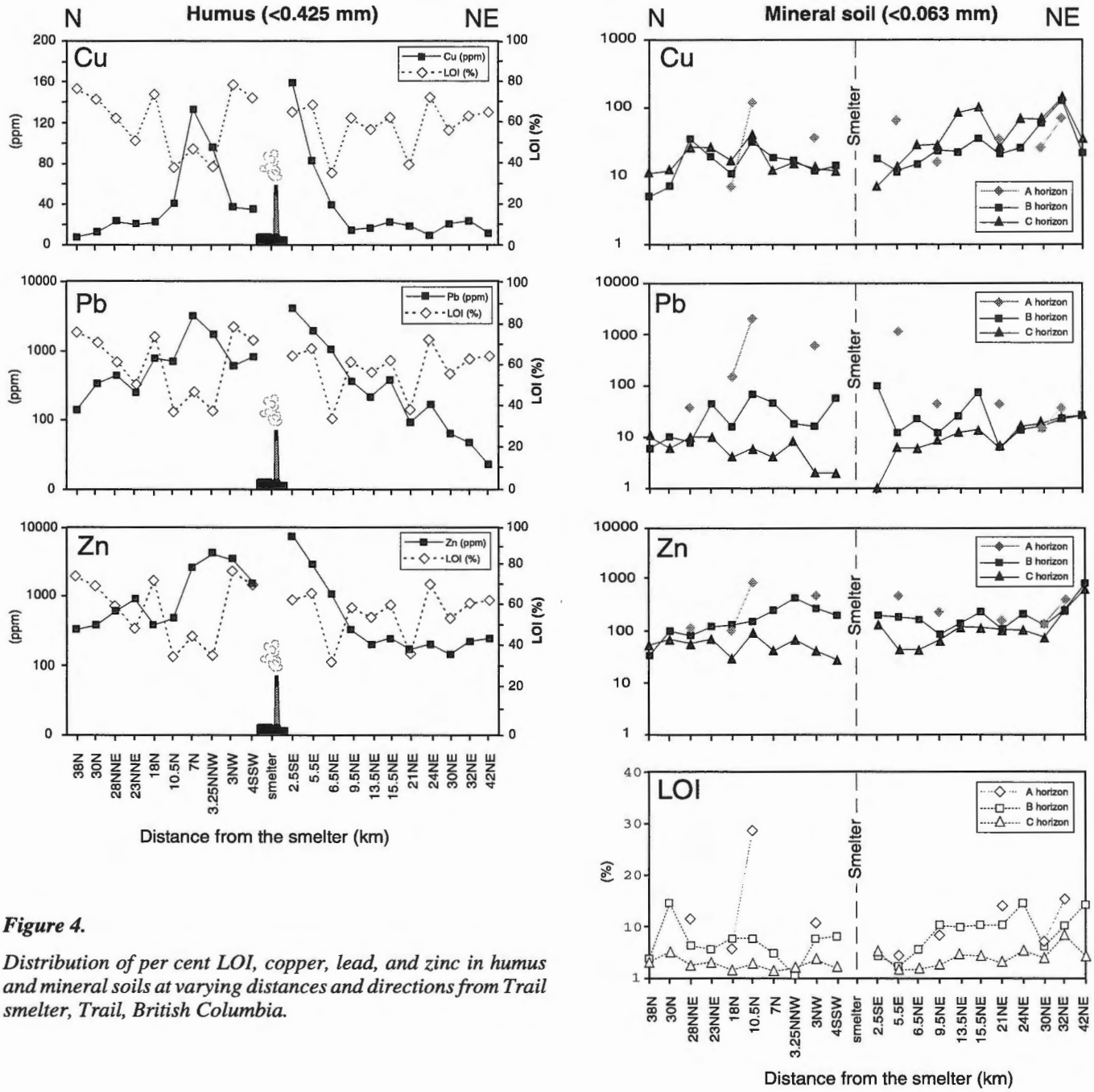

Figure 4.

Distribution of per cent LOI, copper, lead, and zinc in humus and mineral soils at varying distances and directions from Trail smelter, Trail, British Columbia.

The distribution of copper, lead, and zinc in the various sample media and the organic content (% LOI) are shown in Figure 4. For copper, total concentrations in humus are relatively low compared to concentrations in humus collected around the Horne and Flin Flon smelters. Nevertheless, values are elevated at sites within 10 km of the smelter and level off beyond this distance. The enrichment is less pronounced and more variable along the northern transect than the northeastern. For lead, total concentrations in humus tend to decrease with distance along both transects, with no leveling off with distance from the smelter. As with copper, values are slightly depressed at the first two sites on the northern transect adjacent to the smelter. This distribution pattern continues with total zinc concentrations in humus, although values appear to level off at distances greater than 10–15 km northeast from the smelter. It is unlikely that this flattening represents the return to background values in organic soils from the area; however, no conclusions can be reached from the limited number of samples collected. There is no relationship between concentrations of either copper, lead, or zinc and the organic content of humus samples.

With the possible exception of A-horizon samples, there is no evidence of smelter-related enrichment of total copper in mineral soils collected along the transects (Fig. 4). At sites up to 10 km from the Trail operations on the northern transect and approximately 6 km on the northeastern, copper concentrations in A-horizon samples exceed those in both B- and C-horizon samples, suggesting downward migration of the metal from the enriched humus. However, copper concentrations in A-horizon soils are also strongly correlated to organic content ($r = 0.78$). In general, values in C-horizon samples exceed those of B-horizon, which indicates that enrichment at depth is related to sediment provenance. More significant effects of smelter contamination within the soil profile are suggested by the distribution patterns of lead and zinc. For both these elements, concentrations in A-horizon samples exceed those in the B-horizon which, in turn, exceed those in the C-horizon at sites close to the smelter. For lead, and to a lesser extent zinc, this relationship extends for 23–28 km beyond the smelter on the northern transect and 15–21 km on the northeastern. This suggests some downward migration of elements from contaminated humus. Although the organic content of A-horizon soils is strongly correlated to zinc concentrations ($r = 0.70$) and less so to lead ($r = 0.58$), there is no relationship between per cent LOI and copper, lead, and zinc concentrations in B-horizon soils ($Cu = 0.17$; $Pb = -0.12$; $Zn = 0.20$).

Flin Flon smelter — Flin Flon, Manitoba

Regional humus and C-horizon till geochemical analyses from more than 1600 sites within a 200 km radius of the copper-zinc smelting complex at Flin Flon, northwestern Manitoba (lat. 55°46′N; long. 101°52′W) has been published (Henderson, 1995; McMartin et al., 1996, in press). Geochemical maps for humus show a 'bull's eye' pattern, centred on the smelter for arsenic, cadmium, copper, mercury, lead, and zinc, all known smelter emissions. For these elements, concentrations are anomalously high at the centre of the area, and decrease with distance from the smelter, such that the log-concentration of the heavy metal decreases inversely with the log-distance from the smelter until regional background concentrations are reached. Estimates of regional background are determined statistically (McMartin et al., 1996) and indicate that distance to background ranges from 70 to 104 km, with the radius of contamination of As>Cu>Hg>Zn>Pb>Cd. The extent of contamination is also influenced by prevailing wind directions in the area.

Twenty-three sites in the regional geochemical survey were selected for more detailed analyses (Henderson et al., 1998). These sites are located at varying distances from the smelter and represent two transects extending from the point source, and two 'background' sites. One transect extends 82 km north-northwest from the smelter; the other 40 km south-southwest. This suite of samples is similar to those collected in the orientation surveys at Rouyn-Noranda and Trail and will be used to compare the distribution of heavy metals in soils surrounding the smelters.

DISCUSSION

Comparison of heavy-metal concentrations in humus and till

Comparisons of heavy-metal concentrations in the <0.425 mm fraction of humus and <0.002 mm fraction of C-horizon tills from the three smelter sites are shown in Table 2. The comparisons are based on geochemical data from the transect sites only, and the radius of influence in relation to the smelter varies at each location. Based on the results of the Flin Flon study (McMartin et al., in press), all organic soils collected in the Rouyn-Noranda and Trail surveys should lie within the area affected by smelter contamination (<70 km). Smelter-related contamination is seen primarily in the humus since organic soils serve as a sink for heavy metals released to the environment as gases, aerosols, or dust from the smelter stack and other sources (Sposito, 1983), and spherical particles and discrete angular grains characteristic of smelter emissions have been observed in humus in the vicinity of smelters (Adamo et al., 1996; Henderson et al., 1998). In the Flin Flon area, metal concentrations in humus have been shown to accurately reflect the relative proportions of historical emissions from the stack, although not the total concentrations (McMartin et al., in press; Bonham-Carter and McMartin, 1997). Concentrations in C-horizon tills, on the other hand, are related primarily to bedrock composition modified by the effects of glacial erosion, transport, and deposition (Henderson, 1995; McMartin et al., 1996, in press) and are not related to distance from the smelter.

Smelters at Rouyn-Noranda and Flin Flon primarily produce copper and zinc and maximum total concentrations for copper in humus are similar at both sites and enriched compared to those in humus surrounding Trail (Table 2). The Trail facility produces lead and zinc and, consequently, the maximum total concentration of lead in humus is highest at that site, although not significantly enriched compared to

Table 2. Range of trace-metal concentrations in soils in the vicinity of Canadian smelters.

Humus (<0.425 mm)

	As (ppm)	Cd (ppm)	Cu (ppm)	Hg (ppb)	Ni (ppm)	Pb (ppm)	Zn (ppm)
Rouyn	150–8	109–0.25	3910–11	440–50	79–10	3890–30	1810–36
Trail	60–2	90–2	158–8	5340–70	21–3	4230–24	7800–148
Flin Flon	558–<2	43–0.5	2670–29	>100,000–100	169–4	1692–8	7908–174

C-horizon till (<0.002 mm)

	As (ppm)	Cd (ppm)	Cu (ppm)	Hg (ppb)	Ni (ppm)	Pb (ppm)	Zn (ppm)
Rouyn	472–<2	0.5–<0.5	2180–40	310–10	1275–56	50–6	1715–56
Trail	194–<2	0.5–<0.5	355–24	170–<10	43–1.16	100–18	526–96
Flin Flon	136–<2	3.5–<0.5	709–71	190–30	130–5	16–<2	756–52

Rouyn-Noranda. Zinc and mercury concentrations are noticeably lower at Rouyn-Noranda than the other two sites. Near Rouyn-Noranda, a strong correlation was recognized between organic content (% LOI) and mercury (r = 0.83), which indicates mercury is bound with organic material. No such relationship is present in organic surface soils collected at Trail or Flin Flon, which suggests that high concentrations in these localities result from the presence of discrete mercury-rich particulates that are independent of the organic content of the humus (Henderson et al., 1998). Humus near Flin Flon is enriched in arsenic and depleted in cadmium compared to the other two areas.

C-horizon tills in the Rouyn-Noranda area are significantly higher in arsenic, copper, nickel, and zinc than the other two locations. This reflects the extensive mineralization in the Abitibi greenstone belt which underlies the area. Flin Flon is also centred in a greenstone belt and, consequently, copper and zinc values are naturally elevated over those of Trail.

Comparison of distribution patterns in humus

An examination of the distribution of smelter-related metals in humus along the transects in all three areas indicates that the extent of contamination is dependent on the element and the orientation of the site in relation to the smelter (Fig. 2 and 4)(McMartin et al., in press). In the Flin Flon area, the regional dispersal pattern was seen to be skewed in the direction of the dominant winds. In Rouyn-Noranda, elevated trace-metal values in humus extend further along the eastern transect, compared to the western. This is consistent with the dominant wind directions in that region. In the Trail area, lead and zinc enrichments appear to extend further in the northerly direction than the northeasterly, consistent with the Columbia River valley.

Regional distribution patterns indicate the magnitude and extent of smelter fallout. For the <0.425 mm fraction of humus collected from all transect sites at all three locations, total concentrations of arsenic, cadmium, copper, mercury, lead, and zinc are elevated near the smelter and decrease with distance from the smelter. The relationship follows the equation $y = ax^{-b}$, where y is the trace-element concentration, x the distance from the smelter, and a and b variables of the specific trendline for that element (McMartin et al., 1996). Based on this regression curve, comparisons between smelters can be made for each element (Fig. 5). Correlation coefficients indicate the strength of each trendline. Generally, a strong negative correlation ($R^2 > 0.7$) is present between elemental concentrations and distance from the smelter. A weaker correlation is shown for the distribution of mercury ($R^2 = 0.38$) at Rouyn-Noranda and arsenic ($R^2 = 0.42$) and copper ($R^2 = 0.64$) at Trail.

Differences in the dispersal patterns of various smelter-related elements in humus at all three smelter localities are evident from the regression curves (Fig. 5). Concentrations of copper are highest in the vicinity of the Horne and Flin Flon smelter and much lower in humus near Trail. The variation in slope suggests differences in the nature of the emitted particles (i.e. size, composition, etc.), the nature of the humus, and/or atmospheric conditions at each site. Such variation in the slope of the curves is not seen for lead. The lead dispersal pattern is similar at all smelter localities, although concentrations are lower at Flin Flon and comparable at Trail and Rouyn-Noranda, even though Trail is the only lead smelter. Total concentrations of zinc decrease in the order Flin Flon>Trail>Rouyn-Noranda and slopes vary only slightly. For both arsenic and mercury, concentrations are highest in humus near Flin Flon. However, because of differences in the slope, arsenic values in humus at Rouyn-Noranda and Trail exceed those at Flin Flon at some distance from the smelter. This suggests that background concentrations may be higher in the vicinity of the Trail and Horne smelter than at Flin Flon. Mercury concentrations in humus in the Rouyn-Noranda area may not be smelter related, as discussed earlier, since values are low and dependent on the organic content of humus. Cadmium is highest in humus at Rouyn-Noranda and lowest at Trail and appears to have a similar radius of influence at all three localities. Regional sampling in the Rouyn-Noranda and Trail areas is necessary to refine dispersal patterns and determine the full extent of smelter-related fallout.

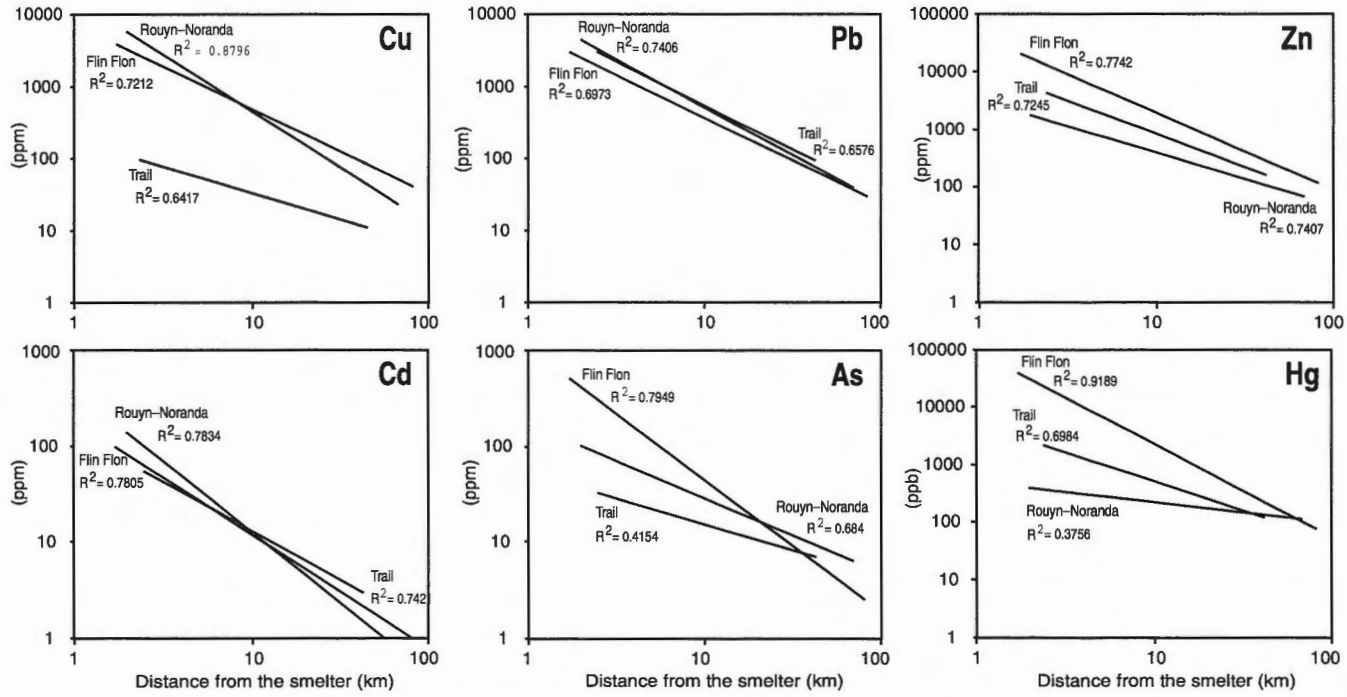

Figure 5. *Dispersal of smelter-related elements in the <0.425 mm fraction of humus in the vicinity of smelters at Flin Flon, Manitoba, Rouyn-Noranda, Quebec, and Trail, British Columbia. The regression curves follow the equation* $y = ax^{-b}$, *where y is the trace element concentration, x the distance from the smelter, and a and b variables of the specific trendline for that element (McMartin et al., 1996). For Flin Flon, n = 20; Rouyn-Noranda, n=17; Trail, n=21.*

Comparison of metal migration within the soil profile

In the Flin Flon area, soil profiles at varying distances from the smelter were examined to characterize regional weathering processes and to determine the extent of downward leaching of surface smelter contamination. Results indicate that subsurface contamination into the B-horizon is not significant beyond 10 km from the smelter, with the exception of zinc, which may be leached into the B-horizon at sites up to 25 km from the smelter (McMartin et al., in press). These conclusions are supported by the results of sequential geochemical analyses designed to determine the residence sites of the heavy metals within the soil horizons (Henderson et al., 1998). In the Rouyn-Noranda and Trail areas, the results of similar analyses are incomplete at present. The enrichment of smelter-related elements in A- and B-horizon soils compared to those of the C-horizon suggests downward migration of heavy metals from contaminated humus may be occurring in the vicinity of the smelters. This is evident along transects in both areas by the distribution of lead and zinc, although in the Rouyn-Noranda area the relationship is only well developed along the western transect where possible subsurface contamination occurs at sites up to 23 km from the smelter for lead and 30 to 35 km for zinc (Fig. 2). In Trail, lead and zinc are enriched in the B-horizon compared to the C-horizon at sites up to 23 km north and 15–20 km northeast (Fig. 4). At all smelter sites, C-horizon soil geochemistry is a reflection of bedrock composition. High copper concentrations observed in the Rouyn-Noranda area are likely related to mineralization in the Abitibi greenstone belt. In order to resolve the extent of subsurface contamination in the area, detailed work on soil profiles will be undertaken.

ACKNOWLEDGMENTS

The authors would like to thank Patti Lindsay and the Sedimentology and Mineral Tracing Laboratory, Terrain Sciences Division, for sample preparation and expediting analyses. We also appreciate the cooperation of the environmental staff from all three smelters involved in the project.

REFERENCES

Adamo, P., Dudka, S., Wilson, M.J. and McHardy, W.J.
1996: Chemical and mineralogical forms of Cu and Ni in contaminated soils from the Sudbury mining and smelting region, Canada; Environmental Pollution, v. 91, p. 11–19.

Azzaria, L.M. and Frechette, G.
1987: Natural and industrial sources of trace elements, Rouyn-Noranda–Val d'Or mining area, Québec, Canada; *in* The Practical Applications of Trace Elements and Isotopes in Environmental Biogeochemistry and Mineral Resources Evaluation, (ed.) R.W. Hurst, T.E. Davis, and S.S. Augustithis; Theophrastus Publications, S.A., Athens, Greece, p. 3–26.

Bonham-Carter, G.F. and McMartin, I.
1997: Calculations on metals in humus around the base-metal smelter at Flin Flon, Manitoba, Canada; *in* Proceedings of the IAMG '97, The Third Annual Conference of the International Association for Mathematical Geology, (ed.) V. Pawlowsky-Glahn; CIMNE, Barcelona, Spain, p. 262–267.

Davies, B.E.
1983: Heavy metal contamination from base metal mining and smelting: implications for man and his environment; *in* Applied Environmental Geochemistry, (ed.) I. Thorton; Academic Press, London, p. 425–462.

Dumontet, S., Dinel, H, and Lévesque, P.E.N.
1992: The distribution of pollutant heavy metals and their effect on soil respiration and acid phosphatase activity in mineral soils of the Rouyn-Noranda region, Quebéc; The Science of the Total Environment, v. 121, p. 231–245.

Dumontet, S., Lévesque, M., and Mathur, S.P.
1990: Limited downward migration of pollutant metals (Cu, Zn, Ni, and Pb) in acidic virgin peat soils near a smelter; Water, Air and Soil Pollution, v. 49, p. 329–342.

Freedman, B. and Hutchinson, T.C.
1980: Pollutant inputs from the atmosphere and accumulations in soils and vegetation near a nickel-copper smelter at Sudbury, Ontario, Canada; Canadian Journal of Botany, v. 58, p. 108–132.

Hall, G.E.M., Vaive, F.E., MacLaurin, A.I., and Hoashi, M,
1996: Selective leaching of the labile organic component of humus and soils with sodium pyrophosphate solution; *in* EXTECH 1: A Multidisciplinary Approach to Massive Sulphide Research in the Rusty Lake–Snow Lake Greenstone Belts, Manitoba, (ed.) G.F. Bonham-Carter, A.G. Galley, and G.E.M. Hall; Geological Survey of Canada, Bulletin 426, p. 201–213.

Henderson, P.J.
1995: Surficial geology and drift composition of the Annabel Lake–Amisk Lake area, Saskatchewan (NTS 63 L/9, L/16, and part of 63 K/12 and K/13); Geological Survey of Canada, Open File 3026, 202 p.

Henderson, P.J. and McMartin, I.
1995: Mercury distribution in humus and surficial sediments, Flin Flon, Manitoba, Canada; Water, Air and Soil Pollution, v. 80, p. 1043–1046.

Henderson, P.J., McMartin, I., Hall, G.E.M., Percival, J.B. and Walker, D.A.
1998: The chemical and physical characteristics of heavy metals in humus and till in the vicinity of the base metal smelter at Flin Flon, Manitoba, Canada; Environmental Geology, v. 34, p. 39–58.

Hogan, G.D. and Wotton, D.L.
1984: Pollutant distribution and effects in forests adjacent to smelters; Journal of Environmental Quality, v. 13, p. 377–382.

Lindsay, P.J. and Shilts, W.W.
1995: A standard laboratory procedure for separating clay-sized detritus from unconsolidated glacial sediments and their derivatives; *in* Drift exploration in the Canadian Cordillera, British Columbia Geological Survey Paper 95-2, p. 165–166.

McMartin, I., Henderson, P., Nielsen, E., and Campbell, J.
1996: Surficial geology, till and humus composition across the Shield margin, north-central Manitoba and Saskatchewan: geospatial analysis of a glaciated environment; Geological Survey of Canada, Open File 3277, 300 p.

McMartin, I., Henderson, P. and Nielsen, E.
in press: Impact of base metal smelter on the geochemistry of soils of the Flin Flon region, Manitoba and Saskatchewan; Canadian Journal of Earth Sciences.

Sheldrick, B.H.
1984: Analytical methods manual 1984; Research Branch, Agriculture Canada, LRRI Contribution No. 84-30.

Sposito, G.
1983: The chemical forms of trace metals is soils; *in* Applied Environmental geochemistry; (ed.) I. Thornton; Academic Press, London, p. 123–170.

Zoltai, S.
1988: Distribution of base metals in peat near a smelter at Flin Flon, Manitoba; Water, Air and Soil Pollution, v. 37, p. 217–228.

Geological Survey of Canada Project 970020-05

True formation factor determination by nonlinear curve fitting

T.J. Katsube
Mineral Resources Division, Ottawa

Katsube, T.J., 1999: True formation factor determination by nonlinear curve fitting; in *Current Research 1999-D; Geological Survey of Canada, p. 27–34.*

Abstract: The pressure characteristics of true formation factor (F) has been determined for three shale samples by eliminating the pore surface conductivity effect, using a nonlinear curve fitting technique. While there exists a widely used technique to eliminate the pore-surface conductivity at single pressures, it is an extremely time-consuming and costly process to repeat that technique at multiple pressures for tight low-permeability shale samples. The purpose of this study was to test the nonlinear curve fitting technique as an alternative.

Results indicate that, by varying the estimated pore-surface resistivity values to be entered into a parallel equivalent circuit model for connecting pores, it was possible to determine the true pore-surface resistivity (ρ_c) value and eliminate the pore-surface conductivity effect, to determine the relationship between F and confining pressure (P):

$$F = F_0 \exp(\alpha P).$$

The coefficients F_0, α, and ρ_c values were in the ranges of 140–520, 0.027–0.039, and 22–100 Ω•m, respectively.

Résumé : Les caractéristiques de pression du facteur de formation (F) réel ont été déterminées pour trois échantillons de shales par élimination de l'effet de conductivité poreuse de surface au moyen d'une technique d'ajustement de courbe non linéaire. Malgré qu'il existe une technique couramment utilisée pour l'élimination de la conductivité poreuse de surface à pressions uniques, le recours répété à cette technique à des pressions multiples pour l'étude de shales compacts peu perméables constitue un processus extrêmement long et coûteux. La présente étude a pour objectif de tester, en tant que solution de remplacement, la technique d'ajustement de courbe non linéaire.

Il ressort des résultats qu'en faisant varier les valeurs estimées de la résistivité poreuse de surface qu'on insère dans un modèle de circuit équivalent parallèle pour pores communicants, on peut déterminer la valeur réelle de la résistivité poreuse de surface (ρ_c) et éliminer l'effet de conductivité poreuse de surface, ce qui permet de déterminer la relation existant entre F et la pression hydrostatique (P) :

$$F = F_0 \exp(\alpha P).$$

Les coefficients F_0 et α et les valeurs de ρ_c s'inscrivent respectivement dans les intervalles 140 à 520, 0,027 à 0,039 et 22 à 100 Ω•m.

INTRODUCTION

A new method for determining the pressure characteristics of the true formation factor, F, has been tested, using several shale samples. While there is a commonly used technique to eliminate the pore-surface conductivity at a single pressure (e.g. Katsube et al., 1991; Katsube and Scromeda, 1993), it can become an extremely time-consuming and costly process to repeat that technique at multiple pressures, particularly for tight, low-permeability mudstone samples (e.g. shale). The purpose of this study was to develop an alternative method for eliminating the pore-surface conductivity effect. This paper reports the results of testing the use of a nonlinear, curve-fitting technique.

The true formation factor, F, which is expressed by the Wyllie and Spangler (1952) equation:

$$F = \tau/(nd), \quad (1)$$

provides important information on the pore structure of rocks because of its relationship to the tortuosity, τ, pore density, n, and pore-size, d, of the interconnecting pores. In principle, F is determined from the bulk rock electrical resistivity, ρ_r, and the electrical resistivity, ρ_w, of the pore fluid that saturates the rock using the Archie (1942) equation:

$$\rho_r = F_a\rho_w, \quad (2)$$

where F_a is the apparent formation factor. However, F_a is not always equal to F, because conductive layers exist on the pore surfaces of rocks and distort the relationship in equation (2). This makes it necessary to replace equation (2) with the Patnode and Wyllie (1950) equation:

$$1/\rho_r = 1/(F\rho_w) + 1/\rho_c, \quad (3)$$

where ρ_c is the true pore-surface resistivity. This implies that by measuring ρ_r for several solutions having different values of ρ_w, and then by inserting them into equation (3), a value of F free from the surface conduction effects can be obtained. A rearrangement of equation (3), suggested by Worthington (1975), has also been used for formation factor determination:

$$1/F_a = 1/F + \rho_w/\rho_c. \quad (4)$$

The true formation factor (F) has been successfully determined for various types of rocks (e.g. Katsube and Walsh, 1987; Hume and Katsube, 1987), including shale (Katsube et al., 1991; Katsube, 1991), using this method. In addition, refinements have also been made to this method to increase the measurement accuracy by changing the selection of ρ_w values of the saturating solutions (Katsube and Scromeda, 1993). However, there are difficulties in applying this technique to determine the pressure characteristics of F for mudstone samples (including shale). Confining pressures, P, applied to a rock sample results in its deformation, so that ρ_r measurements can not be repeated at a lower pressure than already applied. Therefore, ρ_r must be measured for several ρ_w values at each confining pressure, which are usually varied over a range of 2.5 to 100 MPa (e.g. Loman et al., 1993; Katsube and Williamson, 1994) for these rocks. While, in principle, this is possible and the equipment for making such measurements does exist, such measurements for mudstone samples (including shale) can be extremely difficult. This is because the permeability of mudstone samples at P > 10 MPa are usually extremely low (e.g. $<10^{-19}$ m^2, Katsube and Coyner, 1994; Katsube and Connell, 1998) so that it could take many days to make one exchange of a solution in the sample under these pressures. Usually, the ρ_r for one relatively low ρ_w value (<0.2 Ω•m) is measured for the entire pressure range, with the assumption that $\rho_w << \rho_c$ so that the ρ_w/ρ_c in equation (4) is negligible and therefore $F=F_a$. However, the ρ_c values for mudstone samples are often rather low (e.g. <100 Ω•m), giving erroneous values for F, if determined under these assumptions.

One method to overcome these problems is to determine F and ρ_c at atmospheric pressure, assume that ρ_c is constant with pressure, and correct the ρ_r values at each pressure using that ρ_c value. Preliminary tests indicate that this assumption seems to be correct but that the accuracy of the ρ_c values determined by this method is usually not high enough. The ρ_c values determined by this method have a minimum error of about ±40% (Katsube and Scromeda, 1993) which is too low. An error less than ±10% seems to be required for this method to succeed. An alternative method is to assume that the F-P relationship is exponential:

$$F = F_0\exp(\alpha P), \quad (5)$$

where F_0 is the F value at atmospheric pressure and α is a coefficient, and perform a nonlinear curve fitting of the F-P data. That is, assume that the F-P relationship is linear on a semi-log scale and vary ρ_c till a linear F-P relationship is attained. Preliminary results seemed to indicate that this method can succeed. It seems reasonable to assume that the F-P relationship is exponential because the permeability (k) versus pressure (P) relationship (Walsh and Brace, 1984):

$$k = nd^3/(b_0\tau) = k_0\exp(\beta P), \quad (6)$$

which is similar to that for F-P (equation 1), is also exponential (Katsube et al., 1991; Katsube and Coyner, 1994). The b_0, k_0, and β in equation (6) are coefficients. The b_0 is equal to 8 or 12 (Walsh and Brace, 1984). Both F (equation 1) and k (equation 6) are a function of τ, n, and d. The purpose of this paper is to document the results of a study that has used this technique to obtain the true formation factor (F) versus pressure (P) relationship.

METHOD OF INVESTIGATION

Data for analysis

The apparent formation factor (F_a) versus confining pressure (P) data for three shale samples, V-7, V-8, and B-TG-6, have been selected for this analysis (Table 1). The F-P data for samples V-7 and V-8 have been reported in Loman et al. (1993) and the same data for sample B-TG-6 have been reported in Katsube et al. (1996). Samples V-7 and V-8 are well cemented Jurassic shale samples from offshore Eastern

Table 1. Apparent formation factor (F_a), bulk rock electrical resistivity (ρ_r), true formation factor (F), and pore electrical resistivity (ρ_p) data as a function of confining pressure (P) for three shale samples, V-7, V-8, and B-TG-6.

Samples	P	F_a	ρ_r	F	ρ_p
V-7					
ρ_w = 0.083 (Ω•m)	3.5	383.3	31.8	562.1	46.7
ρ_c = 100 (Ω•m)	6.9	416.2	34.5	635.9	52.8
α = 0.02747	13.8	472.6	39.2	777.6	64.5
F_0 = 521.3	27.6	560.3	46.5	1047.4	86.9
r = 0.995	34.5	661.9	54.9	1468.9	121.9
	51.7	762.9	63.3	2079.9	172.6
V-8					
ρ_w = 0.205 (Ω•m)	3.5	225.7	46.9	535.3	109.7
ρ_c = 80 (Ω•m)	6.9	236.8	48.5	602.2	123.5
α = 0.03931	13.8	266.8	54.7	843.4	172.9
F_0 = 471.4	27.6	301.7	61.8	1330	272.6
r = 0.997	34.5	326.6	67.0	2003	410.5
	51.7	350.5	71.9	3442	705.5
B-TG-6					
ρ_w = 0.084 (Ω•m)	3.5	98.5	8.3	157.3	13.2
ρ_c = 22.2 (Ω•m)	6.9	105	8.9	174.5	14.7
α = 0.03739	13.8	123	10.4	230.6	19.4
F_0 = 138.2	27.6	157	13.2	388.2	32.6
r = 0.998	34.5	177.7	15.0	545.3	45.8
	51.8	204.3	17.2	908	76.3
(Units)	(MPa)		(Ω•m)		(Ω•m)

ρ_w = pore-water resistivity
ρ_c = pore-surface resistivity,
α, F_0 = coefficients for $F = F_0\exp(\alpha P)$
r = correlation coefficient

Canada (Katsube et al., 1991; Coyner et al., 1993) and Sample B-TG-6 is an uncemented Tertiary shale from the Beaufort-Mackenzie basin (Katsube et al., 1996). These three samples were selected from groups of shale units (Katsube and Connell, 1998) that display characteristics of relatively high permeabilities for shale units, extremely low permeabilities, and extremely large permeability variations, respectively.

Nonlinear curve fitting analysis technique

Although it is the electrical resistivity (ρ_r) as a function of confining pressure (P) that is measured in the laboratories, the results are routinely converted to apparent formation factor (F_a) versus confining pressure (P) and reported (e.g. Loman et al., 1993; Katsube et al., 1996). For our analytical purposes we first convert the reported F_a data back to ρ_r, by inserting the reported F_a and ρ_w values into equation (2), and then to bulk electrical conductivity, σ_r, by the following relationship:

$$\sigma_r = 1/\rho_r. \tag{7}$$

The pore-surface resistivity (ρ_c) is also converted to pore-surface conductivity, σ_c, in this analysis:

$$\sigma_c = 1/\rho_c. \tag{8}$$

The purpose of this analysis is to determine the true pore resistivity, ρ_p, or pore conductivity, σ_p, expressed by

$$\rho_p = F\rho_w, \tag{9}$$

$$\sigma_p = 1/\rho_p, \tag{10}$$

which are free from pore-surface conductivity effects. The use of conductivities is more convenient in this analysis, since the pore and pore-surface resistivities are in a parallel relationship (Fig. 1). From equations (5) and (7) to (10) we obtain

$$\sigma_p = F_0\exp(-\alpha P)/\rho_w = \sigma_r - \sigma_c. \tag{11}$$

In this analysis, an estimated pore-surface conductivity value, σ_{cx}, is selected and inserted into equation (11) to derive a calculated pore conductivity, σ_{px}, value:

$$\sigma_{px} = F_0\exp(-\alpha P)/\rho_w + x = \sigma_r - \sigma_{cx}, \tag{12}$$

where x is the difference between σ_p and σ_{px}. The σ_{cx} value will be varied until a linear σ_{px}-P relationship (x = 0 in equation 12) on a semi-log scale is obtained. When the linear relationship is attained, it will be judged that a true σ_p-P relationship and a true value for σ_c have been obtained.

ANALYTICAL RESULTS

First, the bulk electrical resistivity (ρ_r) and conductivity (σ_r) values for the three samples V-7, V-8, and B-TG-6 were derived from the previously reported data (Table 1), using equations (2) and (7). The bulk electrical conductivity (σ_r) as a function of confining pressure (P) for sample V-7 is displayed in Figure 2. This figure shows σ_r initially decreasing with increased P, and then leveling off somewhat, rather than

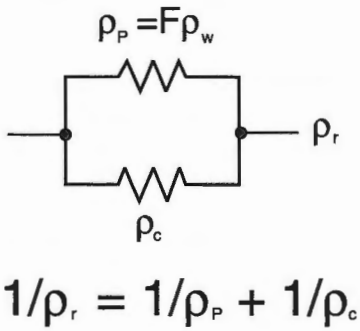

Figure 1. *Equivalent circuit model of connecting pores (Katsube and Hume, 1989), consisting of pore resistivity (ρ_p) or pore conductivity ($\sigma_p=1/\rho_p$) and pore-surface resistivity (ρ_c) or pore-surface conductivity ($\sigma_c= 1/\rho_c$). The bulk electrical resistivity (ρ_r) or bulk electrical conductivity ($\sigma_r=1/\rho_r$) of the rock is the combination of the two,*

$$\sigma_r = 1/\rho_r = \sigma_p + \sigma_c = 1/\rho_p + 1/\rho_c,$$

where ρ_p is a function of formation factor (F) and pore-water resistivity (ρ_w),

$$\rho_p = F\rho_w.$$

continuing to decrease as suggested by equation (11) if $\sigma_r = \sigma_p$ and if the term σ_c were negligible. Based on this figure, a pore-surface conductivity (σ_{cx}) value of 10 mS•m has been selected to calculate σ_{px} (equation 12). In Figure 3, the σ_{px} versus P curves for values ranging from 0.5 times to 2.0 times the selected value for σ_{cx} ($0.5\sigma_{cx}$–$2.0\sigma_{cx}$) of 10 mS•m are displayed. This figure indicates that the linearity of the curve for σ_{cx} = 10 mS•m is rather good and that the selection of that value is probably adequate. The results of these calculations are listed in Table 2.

This linearity can be expressed quantitatively by creating a set of curvature parameters, θ_1, θ_2, and θ_3 which are defined by

$$\theta_1 = \text{ABS}[\sigma_{px3} - (AP_3 + B)], \quad (13)$$

$$\theta_2 = \text{ABS}[\sigma_{px4} - (AP_4 + B)], \quad (14)$$

$$\theta_3 = \text{ABS}[\sigma_{px5} - (AP_5 + B)], \quad (15)$$

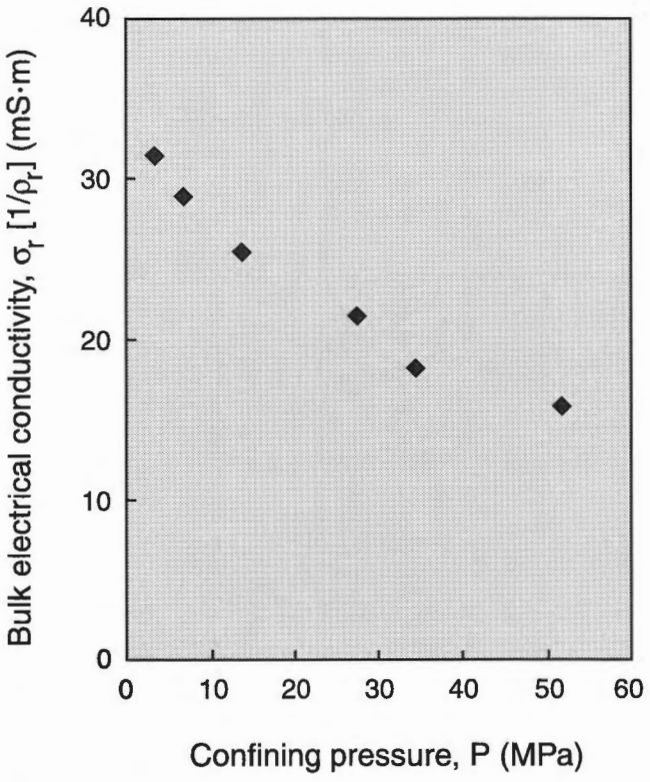

Figure 2. Bulk electrical conductivity (σ_r) as a function of confining pressure (P) for sample V-7.

where A and B are defined as

$$A = (\sigma_{px6} - \sigma_{px1})/(P_6 - P_1), \quad (16)$$

$$B = \sigma_{px1} - AP_1. \quad (17)$$

There are six data points, for each of the seven σ_{px} versus P curves displayed in Figure 3 (Table 2), which are represented by (P_1, σ_{px1}), (P_2, σ_{px2}) to (P_6, σ_{px6}). The abbreviation 'ABS' implies the absolute value. Essentially, these curvature parameters, θ_1, θ_2, and θ_3, in equations (13) to (15), represent the differences between the calculated values: σ_{px3}, σ_{px4}, and σ_{px5}, using equation (12) and the calculated values for conductivity assuming a linear relationship between the two data points: (P_1, σ_{px1}) and (P_6, σ_{px6}), on a semi-log scale, as shown in Figure 4. The three parameters θ_1, θ_2, and θ_3 are displayed as a function of the selected σ_{cx} values in Figure 5. This figure shows a minimum at about σ_{cx}= 8 mS•m for θ_2 and at about σ_{cx}= 13 mS•m for θ_1 and θ_3, suggesting that these values may be more representative of the true σ_c value, compared to the existing σ_{cx}= 10 mS•m. These results are also listed in Table 3.

Now that the true σ_c value can be judged to be within the range of 8–13 mS•m, a refinement analysis is carried out by calculating the F-P curves for various σ_{cx} values within that range, using equations (9), (10), and (12). The results are displayed in Figure 6, for σ_{cx} values of 8, 10, and 13 mS•m. The solid lines are the reduced major axis (RMA, Davis, 1986; Katsube and Agterberg, 1990) for all six data points, and the broken lines are the two reduced major axes for the first four data points (1 to 4) and the last four data points (3 to 6). The three lines for the case of σ_{cx} = 13 mS•m show some discrepancies. The three lines for the case of σ_{cx} = 8 mS•m show a slight discrepancy at the lower confining pressures (P). These two values represent the two extremes for σ_{cx}. The case for σ_{cx} = 10 mS•m is considered as representing the best results, and as representing the true value of σ_c. It shows very minor discrepancies between the three lines which are balanced over the entire range of the P_c values. It is for this reason that the similarity between the three lines is judged to be the best, and that the formation factor coefficients, F_0 and α (equation 5), determined using this value to be closest to the true values of this sample. The coefficients of the three lines for σ_{cx} = 10 mS•m are listed in Table 4. The F values for samples V-8 and B-TG-6 were also determined by following the same procedure, and the results are added to Table 1. The F versus P curves for all three samples are displayed in Figure 7.

Table 2. Log of calculated pore-conductivity (σ_{px}, equation 12) as a function of confining pressure (P) for calculated pore-surface conductivity values ranging from 0.5 times to 2.0 times the selected pore-surface conductivity (σ_{cx}) value of 10 mS•m, for sample V-7.

P	$0.5\sigma_{cx}$	$0.6\sigma_{cx}$	$0.7\sigma_{cx}$	$0.8\sigma_{cx}$	$0.9\sigma_{cx}$	σ_{cx}	$1.1\sigma_{cx}$	$1.2\sigma_{cx}$	$1.3\sigma_{cx}$	$1.4\sigma_{cx}$	$1.6\sigma_{cx}$	$2\sigma_{cx}$
3.5	1.422	1.405	1.388	1.370	1.351	1.331	1.310	1.289	1.266	1.241	1.188	1.058
6.9	1.379	1.361	1.341	1.321	1.300	1.278	1.254	1.229	1.203	1.175	1.112	0.952
13.8	1.312	1.290	1.267	1.243	1.217	1.190	1.161	1.130	1.097	1.060	0.977	0.740
27.6	1.218	1.190	1.162	1.130	1.097	1.061	1.021	0.978	0.930	0.875	0.741	0.177
34.5	1.121	1.086	1.049	1.009	0.964	0.914	0.858	0.793	0.716	0.624	0.343	-
51.7	1.033	0.991	0.944	0.892	0.832	0.763	0.681	0.579	0.446	0.254	-	-

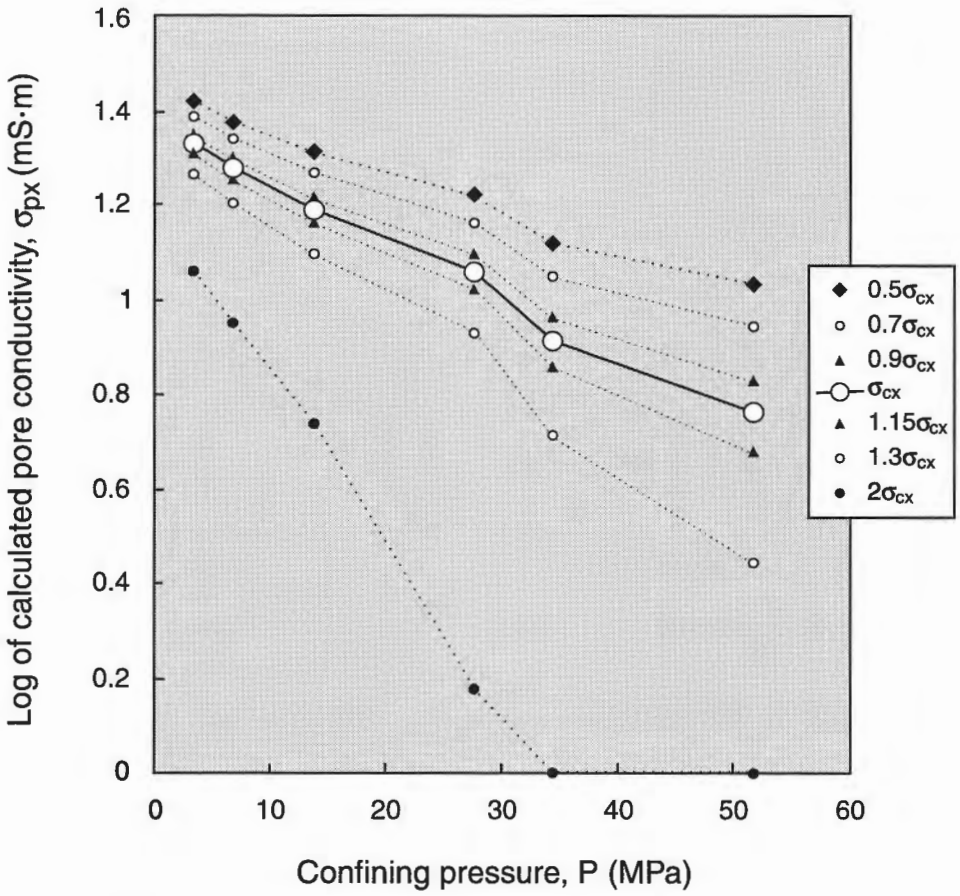

Figure 3. *Calculated pore conductivity (σ_{px}) as a function of confining pressure (P) for pore-surface conductivity values ranging from 0.5 times to 2.0 times (0.5 σ_{cx}–2.0 σ_{cx}) the selected pore-surface conductivity value of σ_{cx}=10 mS•m for sample V-7.*

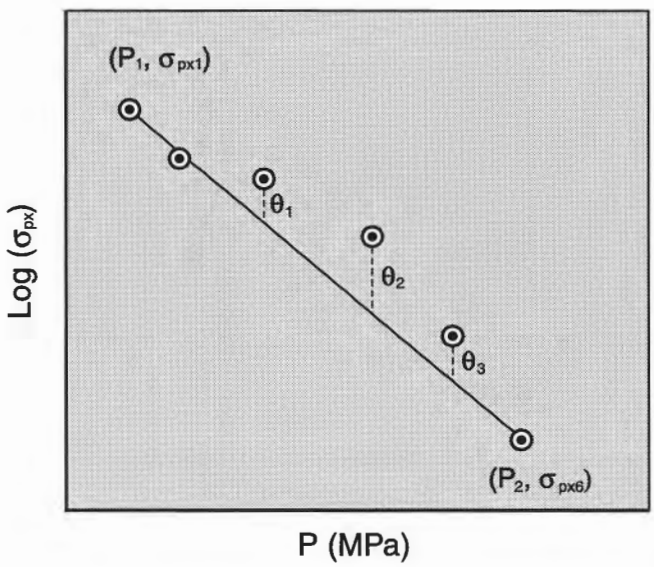

Figure 4.

Diagram showing that the three curvature parameters: θ_1, θ_2, and θ_3, each represent the distances between the three data points and their projections on the line joining the two end data points, (P_1, σ_{px1}) and (P_6, σ_{px6}). P=confining pressure; Log(σ_{px})=log of calculated pore conductivity.

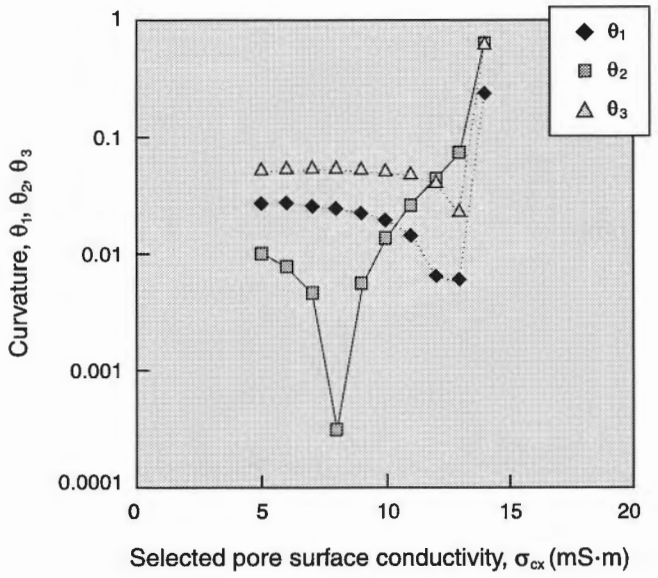

Figure 5. Curves for the curvature parameters, θ_1, θ_2, and θ_3, as a function of pore-surface conductivity values ranging from 0.5 times to 2.0 times (0.5 σ_{cx}–2.0 σ_{cx}) the selected pore-surface conductivity value of σ_{cx}=10 mS•m for sample V-7.

Table 3. Values of the three curvature parameters: θ_1, θ_2, and θ_3, for the calculated pore-surface conductivities ranging from 0.5 times to 2.0 times the selected pore-surface conductivity (σ_{cx}) value of 10 mS•m.

Calculated σ_{cx}	σ_{cx} (mS·m)	θ_1	θ_2	θ_3
$0.5\sigma_{cx}$	5	0.0274	0.0101	0.0513
$0.6\sigma_{cx}$	6	0.0269	0.00773	0.0524
$0.7\sigma_{cx}$	7	0.0261	0.0046	0.0532
$0.8\sigma_{cx}$	8	0.0248	0.0003	0.0536
$0.9\sigma_{cx}$	9	0.023	0.006	0.053
σ_{cx}	10	0.02	0.014	0.052
$1.1\sigma_{cx}$	11	0.0146	0.0259	0.0478
$1.2\sigma_{cx}$	12	0.0068	0.0441	0.0396
$1.3\sigma_{cx}$	13	0.00623	0.0738	0.0223
$1.4\sigma_{cx}$	14	0.24	0.622	0.653
$1.6\sigma_{cx}$	16	-	-	-
$2.0\sigma_{cx}$	20	-	-	-

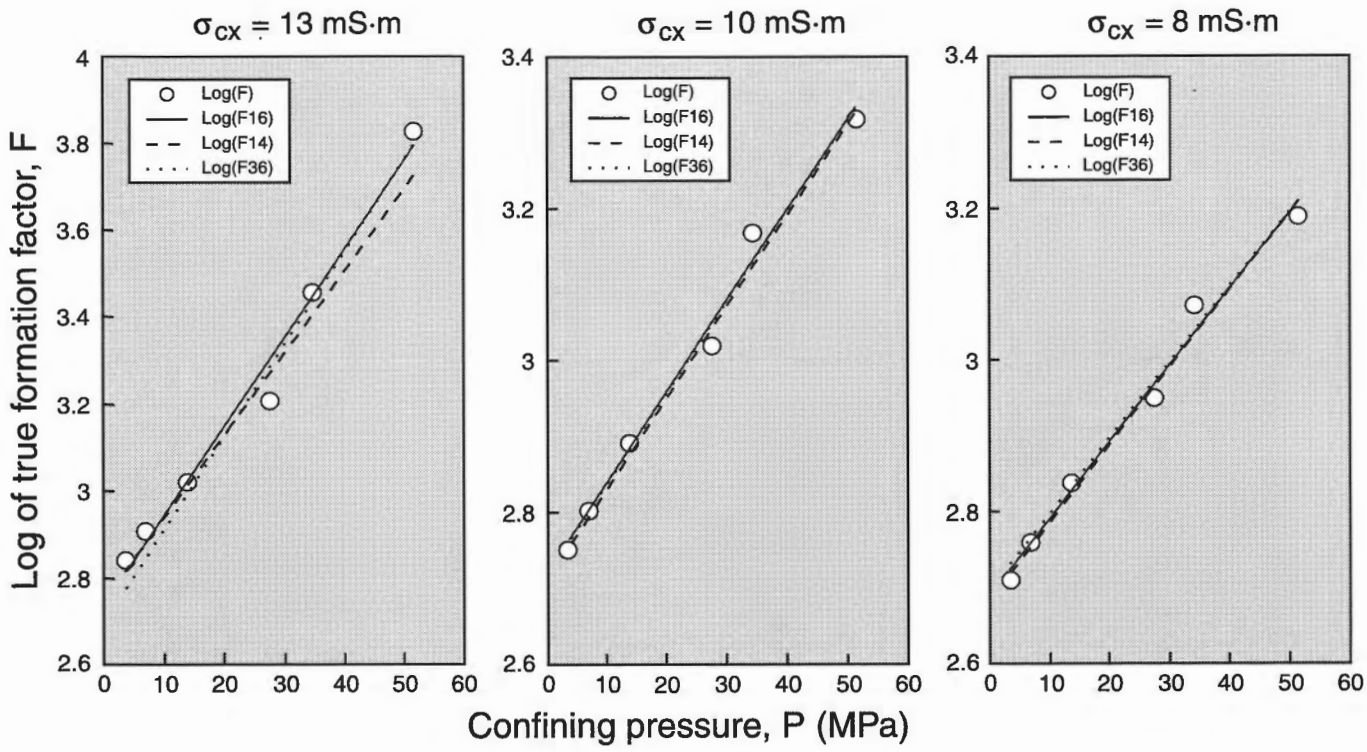

Figure 6. Curves (sample V-7) for the true formation factor (F) as a function of confining pressure (P) for three selected values of pore-surface conductivity (σ_c): 8, 10, and 13 mS•m. The solid lines are the reduced major axis (Davis, 1986; Katsube and Agterberg, 1990) for all six data points, and the broken lines are the two reduced major axes for the first four data points (1 to 4), starting from the left-hand side of the diagrams, and the last four data points (3 to 6).

Table 4. The true formation factor (F) and calculated formation factor values (sample V-7): F_{16}, F_{14}, and F_{36} as function of confining pressure (P) for the selected pore-surface conductivity (σ_c) value of 10 mS•m or a pore-surface resistivity (ρ_c) value of 100 Ω•m. These three parameters represent values for the reduced major axes (RMA, Davis, 1986; Katsube and Agterberg, 1990) for all six data points, the first four data points, and the last four data points, respectively, using the $F = F_0\exp(\alpha P)$ relationship (equation 5). The α and F_0 are coefficients.

P (MPa)	F	F_{16}	F_{14}	F_{36}
3.5	562.1	573.9	567.5	579.8
6.9	635.9	630.1	622.7	636.0
13.8	777.6	761.6	751.8	767.4
27.6	1047.4	1112.8	1095.8	1117.2
34.5	1468.9	1345.0	1322.9	1348.1
51.7	2079.9	2157.5	2115.9	2153.0
α		0.027	0.02731	0.02722
F_0		47	515.8	527.1
r		521.3	0.996	0.992
		0.995		

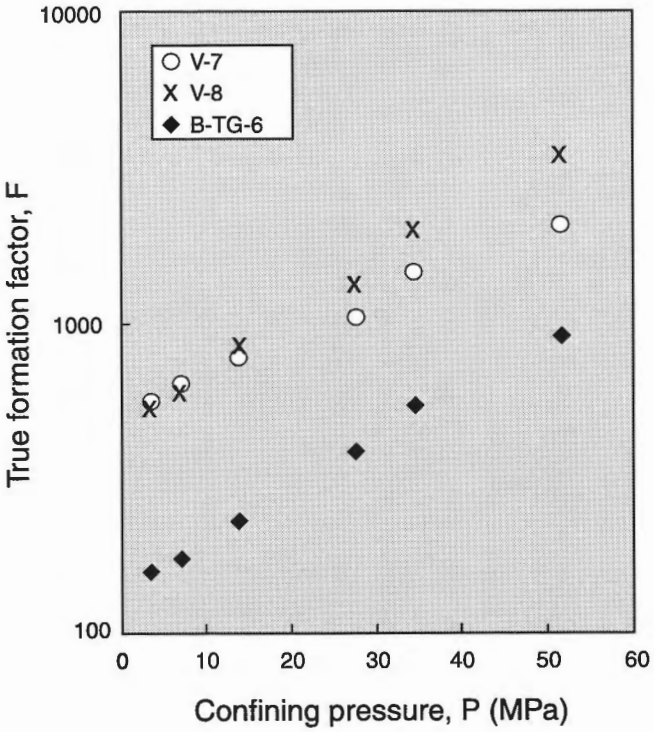

Figure 7. Curves for the true formation factor (F) as a function of confining pressure (P) for the three shale samples, V-7, V-8, and B-TG-6.

DISCUSSION AND CONCLUSIONS

The results of this nonlinear curve fitting analysis for three shale samples suggests that, by varying the pore-surface conductivity values to be entered into a parallel equivalent circuit model for connecting pores, it has been possible to eliminate the pore-surface conductivity effect and determine the true relationship between formation factor (F) and confining pressure (P). Use of the reduced major axis by the liner regression technique has allowed further refinement of this curve-fitting operation. The basis of this analytical technique lies in the assumption that the F-P relationship is exponential:

$$F = F_0\exp(\alpha P),$$

an assumption that seems reasonable since it applies to the permeability-pressure relationship which is explained by a similar pore-structure model. The values of F_0, α, and pore-surface resistivity (ρ_c) for these three samples were in the ranges of 140–520, 0.027–0.039, and 22–100 Ω•m, respectively. However, the absence of independent data for confirmation leaves room for argument over whether the F-P relationship is really exponential, and whether it only appears in that form due to the selection of an appropriate pore-surface conductivity value that was entered into the model. Nonetheless, the main achievement of this study is that a technique has been developed to eliminate the pore-surface conductivity effect from that F-P relationship, if that relationship is exponential.

While the analytical results for these three samples produced linear F-P relationships as were predicted from theory, a question remains on how this technique would perform for cases where the F-P relationship may be exponential but a two-curve system (e.g. permeability-pressure data, Katsube and Williamson, 1994; Katsube and Coyner, 1994). However, this technique has the capability for adding more refinement procedures, such as quantification of the differences between the three reduced major axes that appear in the current refinement procedure.

ACKNOWLEDGMENTS

The author expresses his appreciation and thanks to C.J. Mwenifumbo (Geological Survey of Canada, Ottawa) for critically reviewing this paper and for his useful comments. The author also expresses his thanks to S. Connell (Geological Survey of Canada, Ottawa) for producing the diagrams in this paper, and to N. Perez (Geological Survey of Canada, Ottawa), for her comments.

REFERENCES

Archie, G.E.
1942: The electrical resistivity log as an aid in determining some reservoir characteristics; Transactions of the American Institute of Mining, Metallurgical and Petroleum Engineers, v. 146, p. 54–67.

Coyner, K., Katsube, T.J., Best, M.E., and Williamson, M.
1993: Gas and water permeability of tight shales from the Venture Gas Field offshore Nova Scotia; *in* Current Research, Part D; Geological Survey of Canada, Paper 93-1D, p. 129–136.

Davis, J.C.
1986: Statistics and Data Analysis in Geology; John Wiley & Sons, New York, p. 200–204.

Hume, J.P. and Katsube, T.J.
1987: Pore structure characteristics; *in* Geotechnical Studies at East Bull Lake Research Area (ed.) A.G. Latham; Canada Centre for Mineral and Energy Technology, Report MRL 87-94, p. 39–66.

Katsube, T.J.
1991: Petrophysical characteristics of granites, shales and gabbros, and their significance in nuclear fuel waste containment; *in* Proceedings of 1991 Joint International Waste Management Conference, Volume 2, Seoul, Korea, p. 313–320.

Katsube, T.J. and Agterberg, F.P.
1990: Use of statistical methods to extract significant information from scattered data in petrophysics; *in* Statistical Applications in the Earth Sciences, (ed.) F.P. Agterberg and G.F. Bonham-Carter; Geological Survey of Canada, Paper 89-9, p. 263–270.

Katsube, T.J. and Connell, S.
1998: Shale permeability characteristics; *in* Current Research 1998-E, Geological Survey of Canada, p. 183–192.

Katsube, T.J. and Coyner, K.
1994: Determination of permeability-compaction relationship from interpretation of k-stress data for shales from Eastern and Northern Canada; *in* Industry Research Associates Scheme, (ed.) M. Williamson; Hydrocarbon Charge Modelling Project, Newsletter, v. 5, December 1993, p. 27.

Katsube, T.J. and Hume, J.P.
1989: Electrical resistivity of rocks from Chalk River; *in* Workshop Proceedings on Geophysical and Related Geoscientific Research at Chalk River, Ontario, Atomic Energy of Canada Limited Report AECL-9085, p. 105–114.

Katsube, T.J. and Scromeda, N.
1993: Formation factor determination procedure for shale sample V-3; *in* Current Research, Part E; Geological Survey of Canada, Paper 93-1E, p. 321–330.

Katsube, T.J. and Walsh, J.B.
1987: Effective aperture for fluid flow in microcracks; International Journal of Rock Mechanics and Mining Sciences and Geomechanics Abstracts, v. 24, p. 175–183.

Katsube, T.J. and Williamson, M.A.
1994: Effects of diagenesis on shale nano-pore structure and implications for sealing capacity; Clay Minerals, v. 29, p. 451–461.

Katsube, T.J., Best, M.E., and Mudford, B.S.
1991: Petrophysical characteristics of shales from the Scotian shelf; Geophysics, v. 56, p. 1681–1689.

Katsube, .T.J., Issler, D.R., and Coyner, K.
1996: Petrophysical characteristics of shales from the Beaufort-MacKenzie Basin, Northern Canada; permeability, formation factor and porosity versus pressure; *in* Current Research 1996-B, p. 45–50.

Loman, J.M., Katsube, T.J., Correia, J.M., and Williamson, M.A.
1993: Effect of compaction on porosity and formation factor for tight shales from the Scotian Shelf, offshore Nova Scotia; *in* Current Research, Part E; Geological Survey of Canada, Paper 93-1E, p. 331–335.

Patnode, H.W. and Wyllie, M.R.J.
1950: The presence of conductive solids in reservoir rocks as a factor in electric log interpretation; Transactions of the American Institute of Mining, Metallurgical and Petroleum Engineers, v. 189, p. 47–52.

Walsh, J.B. and Brace, W.F.
1984: The effect of pressure on porosity and the transport properties of rocks; Journal of Geophysical Research, v. 89, p. 9425–9431.

Worthington, P.F.
1975: Quantitative geophysical investigations of granular aquifers; *in* Geophysical Surveys, v. 2, D. Reidel, Dordrecht, p. 313–366.

Wyllie, M.R. and Spangler, M.B.
1952: Application of electrical resistivity measurements to problems of fluid flow in porous media; Bulletin of the American Association of Petroleum Geologists, v. 36, p. 359–403.

Geological Survey of Canada Project 870057

Evaluation of detectors and probe housings for borehole spectral γ-γ logging

C.J. Mwenifumbo and B.E. Elliott
Mineral Resources Division, Ottawa

Mwenifumbo, C.J. and Elliott, B.E., 1999: Evaluation of detectors and probe housings for borehole spectral γ-γ logging; in *Current Research 1999-D; Geological Survey of Canada, p. 35–46.*

Abstract: Three scintillation detectors; sodium iodide, cesium iodide, and bismuth germanate (BGO) were evaluated with particular reference to the detection of low-energy γ-rays in borehole spectral γ-γ (SGG) logging applications. The spectral response characteristics of a low-atomic-number (Z), fibreglass probe housing was also compared to stainless steel, a high-Z probe housing. Direct γ-rays from low-energy barium and medium-energy cesium γ-ray sources, and backscattered γ-rays from a cobalt source, were used to evaluate the detector and probe-housing performances. The BGO detector has the worst energy resolution; however, it is more efficient at stopping γ-rays. The stainless-steel probe housing significantly attenuates the low-energy γ-rays, making it difficult to detect changes in the spectral shape related to variations in the distribution of heavy elements. Stainless steel is, therefore, a poor choice as a probe housing. The attenuation of low-energy γ-rays through the fibreglass probe housing is slight, making it a better choice for SGG logging.

Résumé : Trois détecteurs de scintillation, respectivement à l'iodure de sodium, à l'iodure de césium et au germanate de bismuth, ont été évalués eu égard particulièrement à la détection de rayons γ de faible énergie pour les applications de diagraphie spectrale γ-γ de trou de sondage. Les caractéristiques de réponse spectrale d'un boîtier de sonde en fibre de verre de faible numéro atomique (Z) ont été comparées à celles d'un boîtier en acier inoxydable, à Z élevé. Des rayons γ directs issus de sources de rayons γ de faible énergie en baryum et d'énergie moyenne en césium, ainsi que des rayons γ rétrodiffusés provenant d'une source de cobalt, ont été utilisés pour évaluer les performances des détecteurs et des boîtiers de sonde. Le détecteur au germanate de bismuth présente la plus mauvaise résolution énergétique, mais il est plus efficace pour arrêter les rayons γ. Le boîtier de sonde en acier inoxydable atténue considérablement le rayonnement γ de faible énergie, ce qui rend difficile la détection des variations de motif spectral liées à des variations dans la distribution des éléments lourds. L'acier inoxydable constitue donc un mauvais choix comme boîtier de sonde. L'atténuation du rayonnement γ de faible énergie par le boîtier de sonde en fibre de verre est faible, ce qui en fait un meilleur choix pour les diagraphies spectrales γ-γ.

INTRODUCTION

Several studies have been carried out comparing the performance of different scintillation detectors for borehole-logging applications in natural γ-ray detection. These studies have concentrated on the spectral-response characteristics of these detectors relative to high-energy γ-rays (Conaway et al., 1980; Stromswold, 1981; Borsaru et al., 1983). No work, to the authors' knowledge, has been reported on evaluating the performance or response characteristics of these detectors to low-energy γ-rays because the low-energy γ-rays are usually of less importance in natural γ-ray logging applications. However, recent developments in spectral γ-γ (or selective γ-γ) logging applications for density, ore-grade estimation, and lithology mapping require that accurate measurements be made in the low-energy γ-ray region where information related to the variation in the effective atomic number of the formations can be obtained.

Probe-housing materials also play an important role in the detection of low-energy γ-rays, especially around the scintillation detector. The use of low-atomic-number (Z) beryllium (^{4}Be) windows around the scintillation detector are commonly used in lithodensity probes (Ellis et al., 1985; Gearhart and Mathis, 1987) to minimize the photoelectric absorption of the backscattered γ-rays from the formation by the probe-housing material. Aluminum has also been used as probe-housing material for spectrometric γ-γ logging probes (Almasoumi et al., 1998). Aluminum (^{13}Al) is a relatively low-atomic-number material compared to the stainless steel (essentially iron) material (^{26}Fe) commonly used in probe housing.

The spectral γ-γ (SGG) method has been investigated by the Geological Survey of Canada as a technique for accurate ore delineation and a possible technique for downhole, in situ assaying of base metals (Killeen and Mwenifumbo, 1988). This requires that accurate and reliable measurements be made in the low-energy portion of the backscattered γ-ray spectra. Recent studies have indicated that low-energy Pb Kα X-rays produced by the backscattered γ-rays can also be utilized in the determination of the concentration Pb in the borehole (Almasoumi, et al., 1998; Charbucinski et al., 1997). This study was undertaken to look at the response characteristics (specifically in the low-energy range of spectral γ-γ logging applications) of three commonly used scintillation-detector materials; thallium-activated sodium iodide, NaI(Tl); sodium-activated cesium iodide, CsI(Na); and bismuth germanate, $Bi_4Ge_3O_{12}$, (commonly referred to as BGO); and two probe-housing materials. The probe-housing materials investigated consisted of high-temperature, high-pressure, fibreglass and stainless-steel tubings.

SPECTRAL γ-γ LOGGING

The spectral γ-γ logging technique is based on the different interactions of γ-rays with matter. The energy spectrum of backscattered γ-rays from a radioactive source contains information about the density and chemical composition (i.e. information relating to the effective Z) of the rock formation. There are two main interactions of γ-rays with the rock formation: 1) Compton scattering, in which γ-rays from the source are reduced in energy by scattering as they collide with electrons in the outer shells of atoms, and 2) photoelectric absorption, in which a γ-ray loses all its energy in a collision with an electron and ceases to exist. The probability of photoelectric absorption is roughly proportional to the 5th power of Z of the element with which the γ-ray interacts, and is inversely proportional to about the 3rd power of the γ-ray energy, E. The probability of Compton scattering is roughly proportional to Z/E. Thus, if a spectral γ-ray logging tool is used to measure the distribution of energies of γ-rays from a radioactive source after they have interacted with rock, the shape of the spectrum will contain information about the effective atomic number of the elements that constitute the rock.

Figure 1 is a schematic illustrating the main components of the spectral γ-γ logging system and typical backscattered γ-ray spectra obtained from a ^{60}Co source in formations with low-Z (country rock) and high-Z (ore). When there is a change in the density of the rock being measured, the count rates will increase or decrease due to the associated change in the number of Compton scattered γ-rays reaching the detector. However, when heavy (i.e. high-Z) elements are present in the rock, the associated increase in the photoelectric absorption will cause a significant decrease in count rate in a low-energy window, but a relatively small change in a high-energy window. The low-energy window is affected by both density and Z effect while the high-energy window is only affected by density. Therefore, a ratio of the count rate in the high-energy window to the count rate in the low-energy window can be used to obtain information on changes in Z. The spectral γ-γ (SGG) ratio log is a ratio of counts in a high-energy window to counts in a low-energy window. This ratio increases when the probe passes through zones containing high-Z materials. This technique has been used in coal-ash determinations where the ash constitutes material with heavy elements (e.g. ^{26}Fe, Charbucinski and Mathew, 1982), in iron-ore assay determination (Charbucinski et al., 1977) and in base-metal sulphide determinations (Killeen and Mwenifumbo, 1988).

Detector material

The most widely used scintillation-detector materials for borehole-logging applications in natural spectral γ-ray and spectral γ-γ logging are NaI(Tl) and CsI(Na). The BGO detector is less commonly used and its applications have been investigated mainly for the detection of high-energy γ-rays (Nestor and Huang, 1975; Evans, 1979; Drake, 1981). Table 1 summarizes some of the properties of these three scintillation detectors. Three detectors of the same size were not available for this evaluation. The NaI(Tl) and CsI(Na) detectors were of the same size (25 x 76 mm) whereas the BGO was larger (25 x 127 mm). The use of the name 'detector' in this study implies an integral assembly photomultiplier tube and a hermetically sealed crystal.

The energy resolution values in Table 1 represent typical values provided by the manufacturer of the detectors and may vary with detector size. The NaI(Tl) detector has the best energy resolution among these three scintillation detectors. CsI(Na) has a higher density (4.51 g/cm^3) than NaI(Tl) (3.67 g/cm^3) making it more efficient for detecting high-energy γ-rays. However, the energy resolution of the CsI(Na) detector is inferior to the resolution of the NaI(Tl) (Conaway et al., 1980; Borsaru et al., 1983). The BGO detector is made of high-Z material (^{83}Bi) and its density (7.13 g/cm^3) is far greater than either of the NaI(Tl) or the CsI(Na) detectors. It has, therefore, greater stopping power, especially for high-energy γ-rays, but also the worst resolution (Conaway et al., 1980; Stromswold, 1981; Borsaru 1993).

Table 1. Some properties of detectors.

Detector Material	Size (mm)	Density (g/cm^3)	Energy Resolution*
NaI(Tl)	25 x 76	3.67	8
CsI(Na)	25 x 76	4.51	11
BGO - $Bi_4Ge_3O_{12}$	25 x 127	7.13	20
*measured at 662 keV, ^{137}Cs peak			

Probe-housing material

The most widely used probe-housing material is stainless steel. The standard probe housing for the GSC spectral γ-γ (SGG) logging probes is stainless steel. Although the attenuation of low-energy γ-rays is quite significant with this type of probe housing, the SGG data have proven quite promising in mapping heavy-element distributions along the borehole (e.g. base-metal sulphides) within a formation and in estimating the concentration of these heavy elements. Recently, however, the requirement that the logging probes operate to depths of up to 2 km has necessitated increases in the thickness of GSC probe housing and hence the low-energy backscattered γ-rays from the formation are significantly attenuated by photoelectric absorption. This prompted the investigation into a low-Z housing material for high-pressure

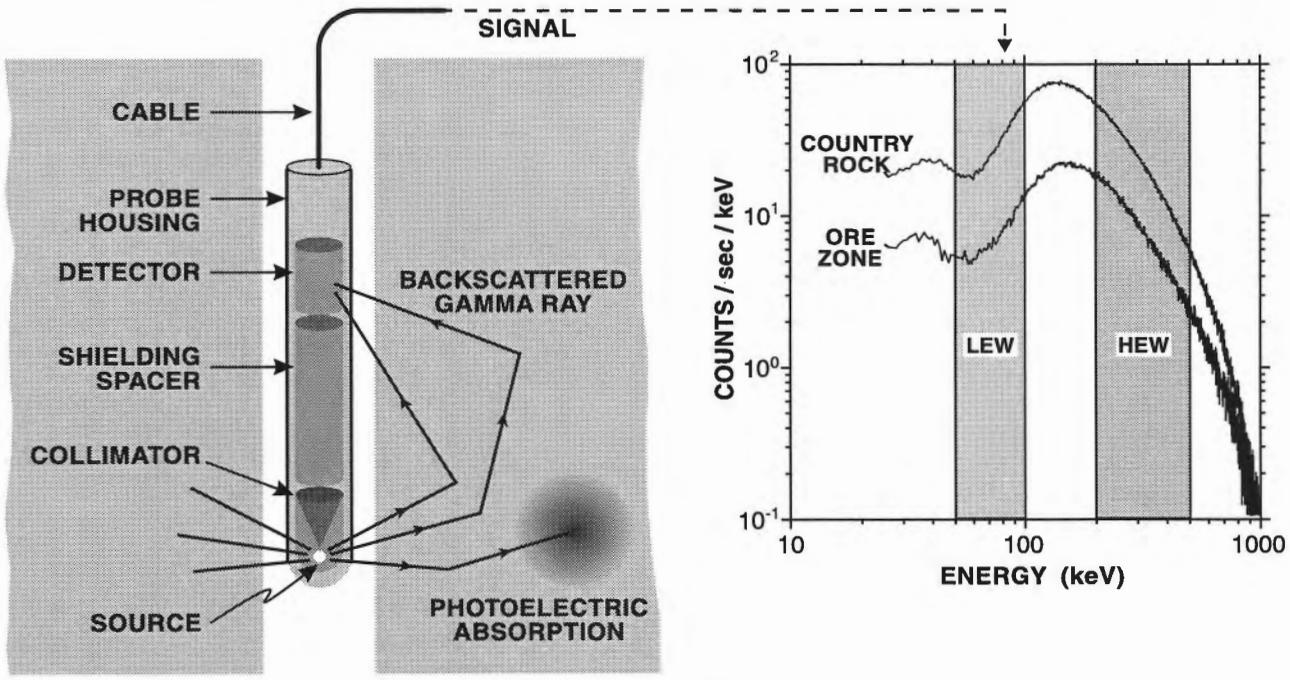

Figure 1. Schematic illustrating the main components in the spectral γ-γ logging technique. The source (^{60}Co) is separated from the detector by a collimator and a shielding spacer. The energy spectra of the backscattered γ-rays are recorded in 512 channels covering an energy range from 0 to 800 keV. On the right, backscattered γ-ray spectra recorded in a relatively low-Z country rock and in a high-Z, mineralized ore zone are compared. In the ore zone, the large decrease in the count rate at low energy (photoelectric window LEW), relative to that observed in the country rock, is easily seen compared to the decrease in the high energy (Compton scattering region, window HEW)

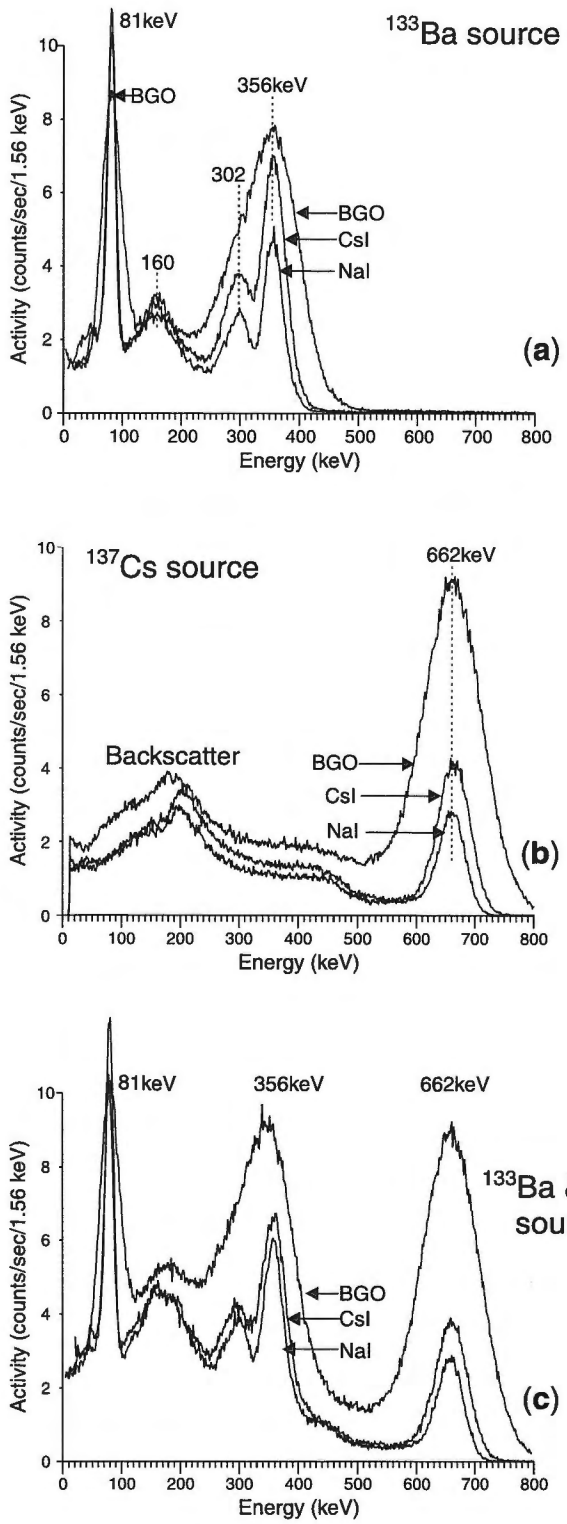

applications. In the petroleum industry, the lithodensity tools (Ellis et al., 1985; Gearhart and Mathis, 1987) use a low-Z metallic beryllium (^{4}Be) window around the detector to allow low-energy backscattered γ-rays from the formation to pass through to the detector with little attenuation. These beryllium windowed lithodensity probes use collimated sources and the detector is side-walled. The construction of probes using beryllium is quite expensive. The GSC's SGG probes have detectors that are not windowed and also the source is omnidirectional. Instead of constructing expensive beryllium-windowed probe housings, the GSC sought to find an alternative (less expensive), relatively low-Z material for use as probe housings.

Aluminum has been used as probe-housing material (Almasoumi et al., 1998) because of its relatively low atomic number (^{13}Al). The pressure and temperature ratings for this material are, however, not adequate for the depths that the GSC has targeted. Some of the GSC's logging probes (e.g. IFG multiparameter probe) use fibreglass tubing as probe-housing material. These fibreglass tubes are rated to stand water pressures to 2 km depths. Borehole logging has been carried out with these probes to this depth. Fibreglass is a composite structure constructed of glass (silica, SiO_4) fibre-reinforced thermoset epoxy matrix (AMALGA Composites Inc.). The exact components and their percentages are not provided by the manufacturer because of the proprietary nature of the information for the products. The overall effective atomic number for the fibreglass material is believed to be fairly low (comparable to aluminum), considering that the main constituent used in the fabrication of the tubes is glass (^{14}Si, ^{8}O).

Laboratory experiments were carried out to investigate the response characteristics of stainless steel and fibreglass housings to both direct and backscattered, low-energy γ-rays. Table 2 shows the properties and sizes of the tubes used in the construction of the probe housings.

Figure 2. *The response of NaI(Tl), CsI(Na), and BGO detectors to a low- and medium-energy γ-ray source. The 512-channel, γ-ray spectra (energy range: 0 to 800 keV, 1.56 keV per channel) were acquired over a period of 5 minutes. Direct γ-rays from the source were recorded without a probe housing around the detector. Figure 2a: γ-rays from a low-energy, ^{133}Ba source (two main photopeaks at 81 keV and 356 keV); Figure 2b: γ-rays from a medium-energy, ^{137}Cs source (662 keV photopeak), and Figure 2c: γ-rays from a composite, ^{133}Ba + ^{137}Cs source.*

Table 2. Some probe-housing properties.

Material	OD (mm)	ID (mm)	Thickness (mm)	Composition
stainless steel	38.1	34.3	1.9	mainly iron (^{26}Fe)
fibreglass	42.0	34.7	3.7	mainly silica (^{14}Si,$^{8}O_4$)

RESULTS

Laboratory investigations into the performance of the three detectors and the two probe-housing materials involved two sets of experiments using direct and backscattered γ-rays. A ^{133}Ba, low-energy γ-ray source and a ^{137}Cs, medium-energy γ-ray source were used for the direct γ-ray source. Five minutes of spectra were acquired with each of these sources separately and with the two sources together using the NaI(Tl), CsI(Na), and BGO detectors. This set of experiments was conducted for three probe-housing conditions; no housing, stainless-steel housing and fibreglass housing. The probe electronics and data acquisition systems were maintained the same in all these investigations. Measurements were made by interchanging detectors in the same borehole-probe electronics package.

Experiments recording backscattered γ-rays were also carried out in the standard (SGG) logging configuration (Fig. 1) in model boreholes at GSC Lebreton calibration facilities.

Detector responses to low- and medium-energy γ-ray sources

Figure 2 shows five-minute γ-ray spectra obtained with low- (^{133}Ba) and medium-energy (^{137}Cs) γ-ray sources using the NaI(Tl), CsI(Tl), and BGO detectors. Direct γ-rays from the sources were recorded without a probe housing around the detector. The objective of these experiments was to investigate the response characteristic of the detectors without the influence of probe-housing material.

Figure 2a shows γ-ray spectra obtained with a low-energy ^{133}Ba source with the detector material as a variable. The two main ^{133}Ba peaks (81 and 356 keV) are clearly indicated on all the spectra. The NaI(Tl) and CsI(Na) detectors show fairly similar spectral response characteristics. Both clearly show the minor photopeaks at 302 and 160 keV. The CsI(Na)-measured γ-ray activity is, however, higher and its resolution is poorer than that of the NaI(Tl) detector for energies above 150 keV. At the 81 keV photopeak, the difference in the count rate and resolution of these two detectors is relatively small. The BGO detector shows higher count rate than either of the two other detectors for energies above 150 keV, partly because it is 67% larger and partly because it is a more dense material and therefore, more efficient. The BGO detector shows lower γ-ray activity at the 81 keV photopeak in contrast to the observations in the energy range above 150 keV. The energy resolution is, however, noticeably poorer than that of the NaI(Tl) and CsI(Na) detectors.

Figure 2b shows γ-ray spectra from a ^{137}Cs source comparing response characteristics of the NaI(Tl), CsI(Tl), and BGO detectors. The ^{137}Cs peak at 662 keV is clearly indicated on all the spectra. The γ-ray activity measured for both the NaI(Tl) and CsI(Na) detectors is lower than that observed with the BGO detector, as expected. However, the resolution is better with these two detectors, as observed with the low-energy ^{133}Ba source. All the spectra with the cesium source show a broad maximum around 200 keV. This backscatter peak is more likely due to contribution from scattering sources around the detectors. The ^{137}Cs source was kept in a tin container which may also contribute to the backscatter peak.

Figure 2c shows spectra for a composite, low-energy (^{133}Ba) and medium-energy (^{137}Cs) source comparing response characteristics of the three detector materials. The same observations seen with the single low-energy ^{133}Ba source (Fig. 2a) and the medium-energy ^{137}Cs source (Fig. 2b) apply to the composite source configuration. There are some slight differences in the relative peak heights at the 356 keV and 662 keV photopeaks, between the BGO and the other two detectors.

Figure 3 shows five-minute, γ-ray spectra from ^{133}Ba and ^{137}Cs sources acquired using NaI(Tl) (Fig. 3a), CsI(Na) (Fig. 3b), and BGO (Fig. 3c) detectors. These data illustrate the characteristic change that occurs in the γ-ray spectrum as a function of probe-housing material. The three spectra for each detector represent the following probe-housing conditions; i) no housing, ii) low-Z, fibreglass housing, and iii) high-Z, stainless-steel housing (Table 2).

There is hardly a change in the shape or characteristics of the spectra above 300 keV acquired with the NaI(Tl) detector for all the three probe-housing conditions. However, attenuation of the low-energy γ-rays, especially at the 81 keV photopeak, is quite significant through the steel probe housing (*see* details in Fig. 4). The responses for no housing and fibreglass housing are virtually identical for the entire 800 keV range, including the 81 keV ^{133}Ba photopeak. There is barely any degradation in the energy resolution at both the 356 and 662 keV photopeaks. These observations are similar for the other two detectors (Fig. 3b - CsI(Na) detector and Fig. 3c - BGO detector).

The high-Z, steel probe housing prevents γ-rays in the low-energy region from reaching the detector through photoelectric absorption. Although most of the borehole natural γ-ray logging applications consider the measurements of photoelectric effect less important, the spectral γ-γ logging makes use of these measurements for lithology measurements (e.g. the lithodensity tool, Ellis et al., 1985; Gearhart and Mathis, 1987), and for heavy-element detection and estimation of percentages of the heavy elements (Killeen and Mwenifumbo, 1988; Mwenifumbo, 1991; Charbucisnki et al., 1997).

Backscattered γ-ray spectra in models

The primary purpose of these experiments was to determine the spectral response characteristics of low- to medium-energy (0–800 keV) backscattered γ-rays obtained with the

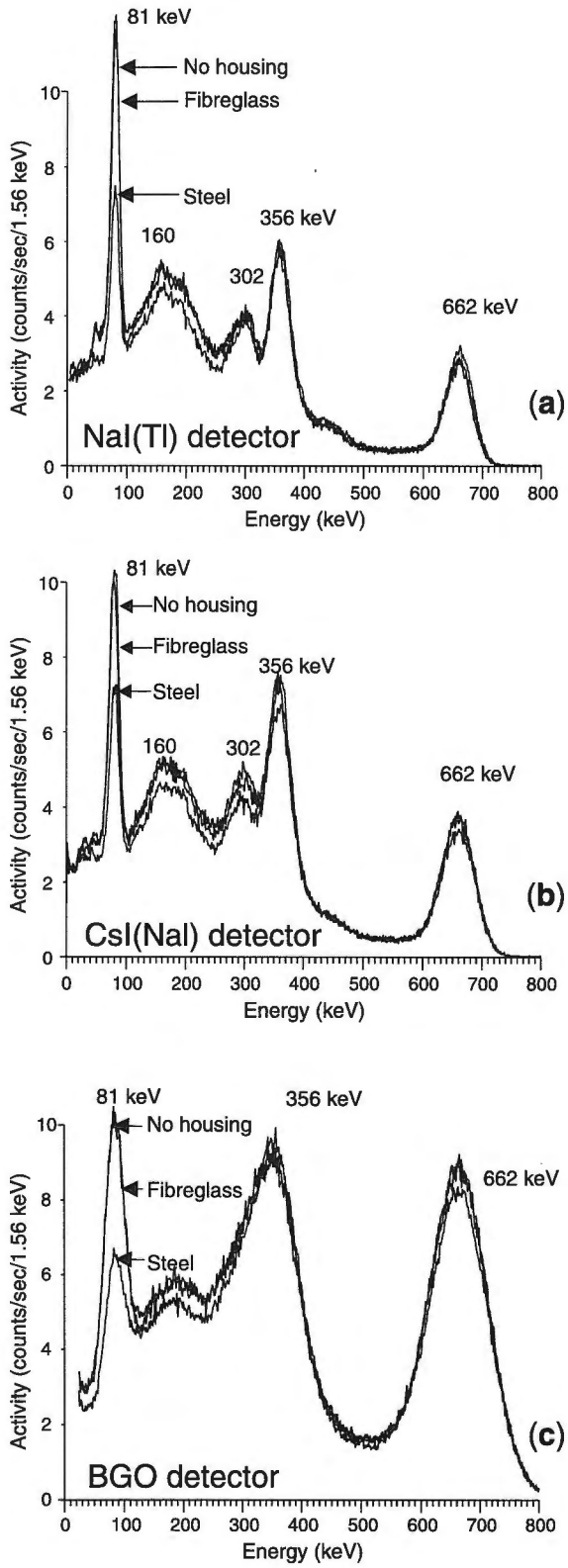

Figure 3. *Comparison of γ-ray spectra from ^{133}Ba + ^{137}Cs source recorded using NaI(Tl) (Fig. 3a), CsI(Na) (Fig. 3b), and BGO (Fig. 3c) detectors with different probe housings around the detectors. Spectra were acquired over a period of 5 minutes with no housing, with fibreglass housing, and with stainless-steel housing.*

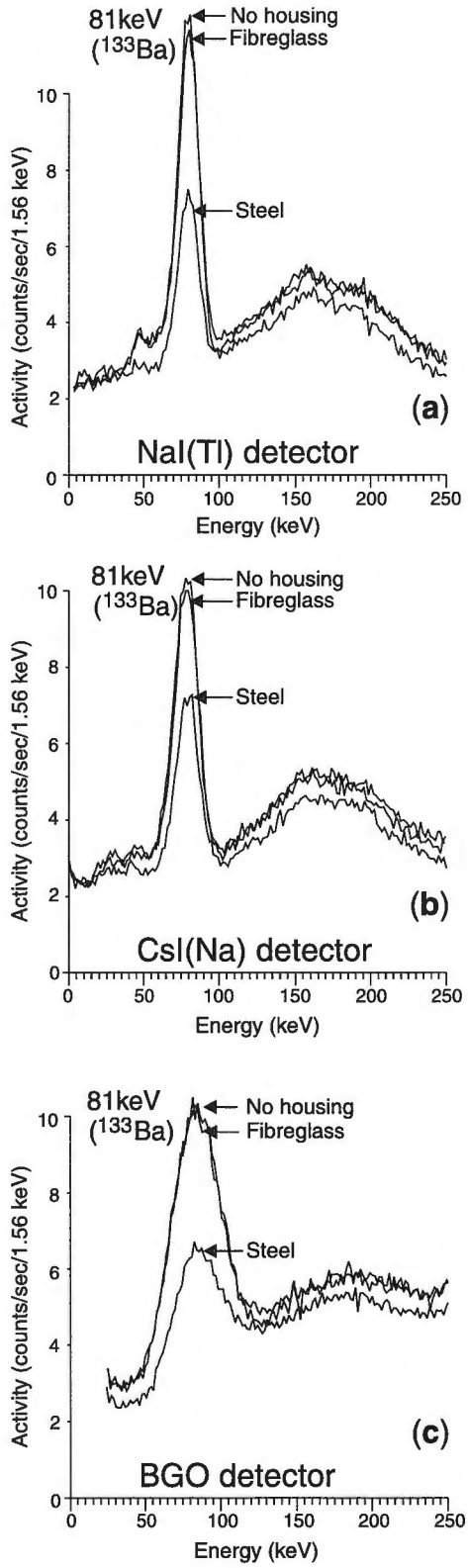

Figure 4. *Expanded section of the data shown in Figure 3, comparing the probe-housing responses to low-energy γ-rays (81 keV γ-ray energy from ^{133}Ba source) for the NaI(Tl), CsI(Na), and BGO detectors.*

three detectors and two probe-housing combinations so that an optimum detector-housing combination could be constructed for spectral γ-γ measurements. The probe configuration is presented in Figure 1. For each probe configuration, the detector was separated from a γ-ray source by tungsten shielding to prevent direct radiation entering the detector. A ^{60}Co γ-ray source with a strength of 370 MBq (10 milliCurie) was used. Spectra were recorded over an energy range from 0–800 keV in 512 channels resulting in a nominal energy calibration of 1.56 keV/channel. The backscattered γ-ray spectra for each parameter combination were acquired over a 5-minute time interval.

The models were constructed with different types and grade of high-Z media (pyrite, FeS_2; barite, $BaSO_4$; and galena, PbS). The model and probe geometry used in these laboratory experiments is illustrated in Figure 5. The pyrite, barite, and galena materials were mixed with silica sand. The models were constructed out of cardboard and plastic tubes 915 mm long and 300 mm in diameter. A 60 mm ID plastic tube, simulating a borehole, was placed axially in the model. The radial thickness of the scattering medium, surrounding the borehole was, therefore, 120 mm. The source-detector

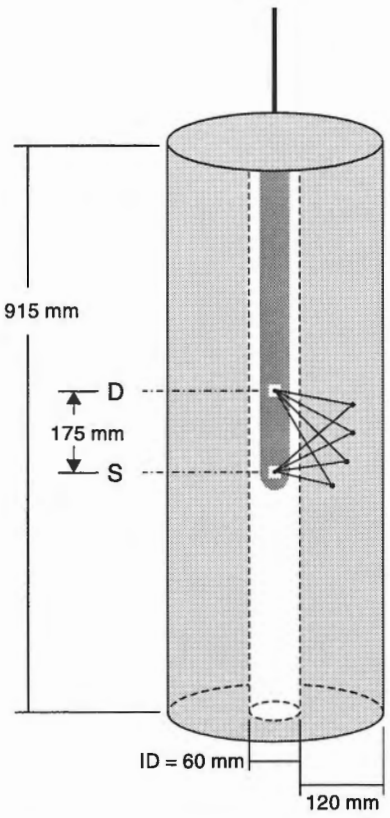

Figure 5. *Cylindrical model and probe geometry used in the laboratory experiments with different high-Z scattering media (pyrite, FeS_2; barite, $BaSO_4$; and galena, PbS).*

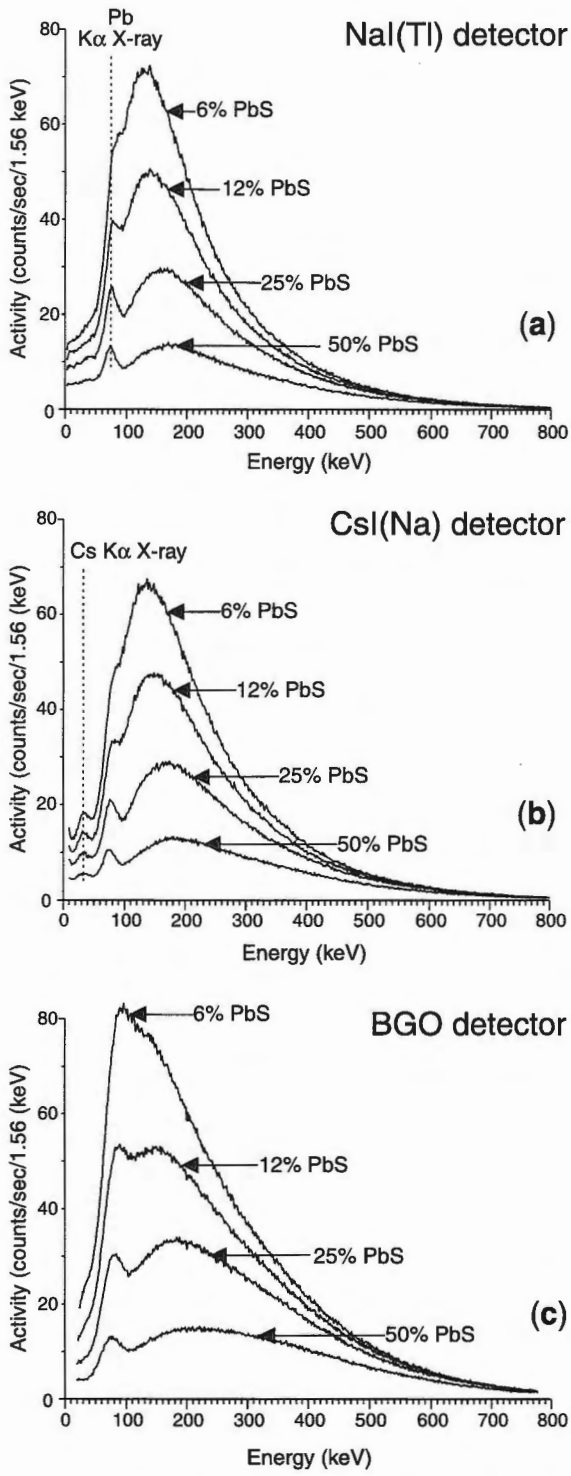

Figure 6. *Backscattered γ-ray spectra from a ^{60}Co source acquired in several galena models with a NaI(Tl) (Fig. 6a), a CsI(Na) (Fig. 6b), and a BGO (Fig. 6c) scintillation detector. Four galena models with varying percentages of PbS mixed with silica sand (6%, 12%, 25% and 50% PbS) were used. Five-minute spectra were acquired with a fibreglass probe housing.*

spacing for the probe was 175 mm. The probe was placed in the centre of the simulated borehole. Four galena models (concentrations 6%, 12%, 25% and 50% PbS) were used in the experiments. Also 50% pyrite and 50% barite models were used.

Detector-material response in galena models with different grade

Figure 6 shows backscattered γ-ray spectra from a ^{60}Co source acquired with NaI(Tl) (Fig. 6a), CsI(Na) (Fig. 6b) and BGO (Fig. 6c) scintillation detectors, respectively, in the galena models. The measurements were made in dry 'boreholes' and material. The fibreglass housing was used in the probe configurations for all the measurements.

Figure 6a shows γ-ray spectra acquired with a NaI(Tl) detector. The γ-ray activity decreases with increasing percentage of galena because γ-ray attenuation by both Compton scattering and photoelectric absorption increases as the percentage of galena increases. The backscatter peak is observed between 100 and 250 keV. The γ-ray spectrum in the 6% galena model shows a shoulder on the left side of the backscatter peak at 75 keV. This shoulder develops into a prominent peak in the 12% model through to the 50% galena models. Photoelectric absorption predominates at low energies so that most of the incident photons are totally absorbed. In a small fraction of these absorption processes, the binding energy of the K electrons in the atoms in the scattering media may be lost by escape of Kα X-rays. This energy loss gives rise to satellite peaks below the main backscatter peak. The peak around 75 keV represents the characteristic Pb Kα X-ray emission peak ($E_{K\alpha}$ =74.96 keV). The presence of this peak in the spectra suggests the possibility of detecting Pb within a polymetallic mineralized zone and the possibility of estimating the concentration of Pb along the borehole (Charbucisnki et al., 1997; Almasoumi, et al., 1998).

The γ–ray spectra acquired with a CsI(Na) detector (Fig. 6b) shows the same characteristics as those observed with the NaI(Tl) detector except that there is an additional small peak observed around 31 keV. This peak is only prominently observed with the CsI(Tl) detector material. It appears to represent the position of the Cs k-shell photopeak ($E_{K\alpha}$=30.97)

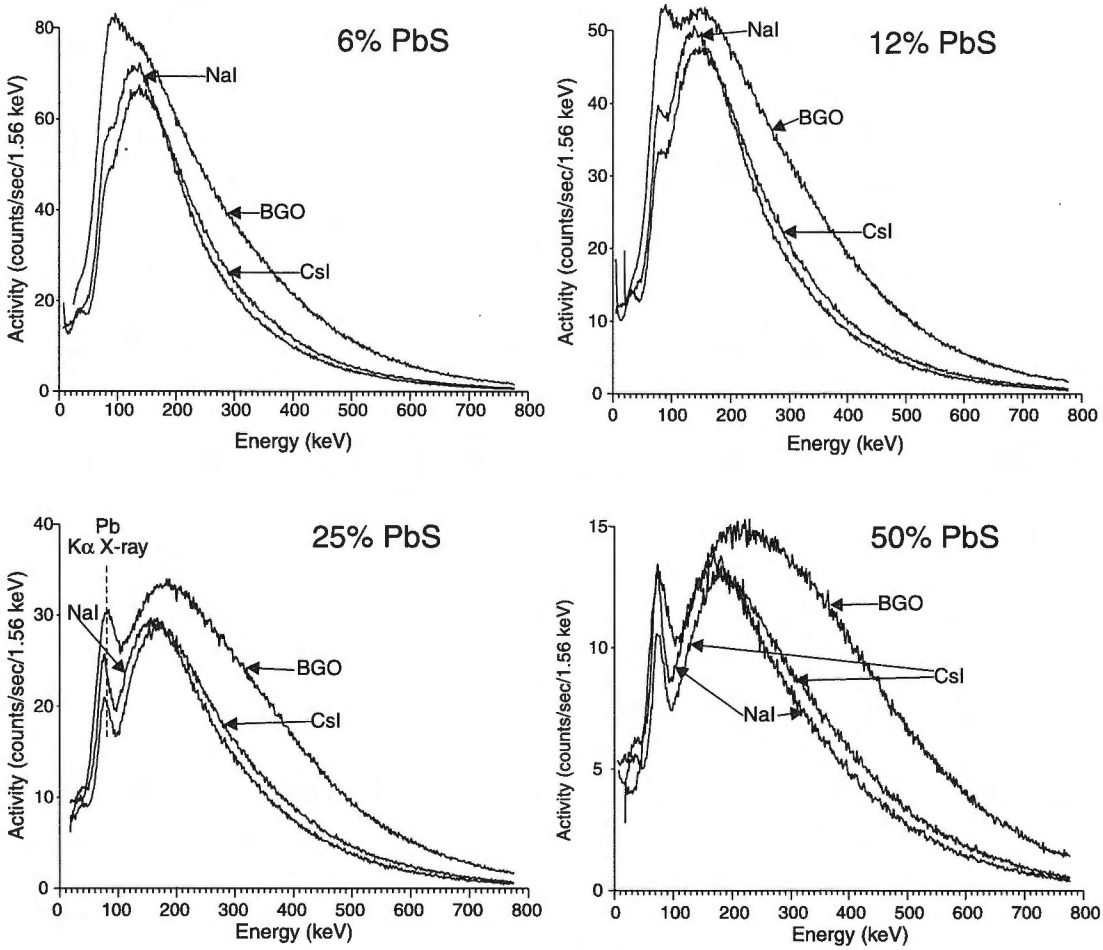

Figure 7. *Same data presented in Figure 6 emphasizing a comparison of detector responses as a function of per cent galena (PbS).*

which is due to the excitation of the Cs in the detector material by the backscattered γ-rays. This Cs X-ray photopeak may be used to monitor the gain shifts during data acquisition, as a non-zero offset correction for the spectra.

The response to backscattered γ-rays from ^{60}Co source measured with the BGO detector is similar to that observed with the other two detectors (NaI(Tl) - Fig. 6a and CsI(Na) - Fig. 6b) in that the γ-ray activity decreases with increasing percentage of galena because γ-ray attenuation by both Compton scattering and photoelectric absorption increases as the percentage of galena increases. The backscatter peak is also observed between 100 and 250 keV. However, the Pb Kα X-ray emission peak, observed as shoulder on the NaI(Tl) and CsI(Na) spectra at 75 keV, is higher than the backscatter peak. This observation cannot be explained at the present time, but may be due to an overall increase in γ-rays at this position from the detector material (Bi X-ray emissions at $E_{K\alpha}$=77keV). This peak also develops into a prominent peak at higher percentages of galena.

Figure 7 shows the same data as in Figure 6, but is plotted to emphasize the change in spectral shape between the three detectors in each of the four galena models. One interesting observation in these plots is that the activity measured by the CsI(Na) detector is higher compared to that of the NaI(Tl) detector above the backscatter peak (above 200 keV) and lower below 200 keV.

Detector response in pyrite, barite, and galena models

Figures 8 and 9 show the backscattered γ-ray spectra from a ^{60}Co source acquired with NaI(Tl), CsI(Na), and BGO detectors in 50% pyrite (FeS_2), 50% barite ($BaSO_4$), and in 50% galena (PbS). The matrix for all the models consisted of silica sand. These models represent variations in the effective atomic number in the range of most base-metal sulphides. The data were acquired with the probes configured with the fibreglass probe housing. The data presented in Figures 8 and 9 are the same. In Figure 8 they are presented to compare the response characteristics of the three detectors for the three scattering media, whereas the data in Figure 9 are presented to compare the response in the three scattering media for each type of detector. The backscattered γ-ray activity decreases considerably from FeS_2 to PbS because of the increase in the effective atomic number of the scattering media (high-Z elements are ^{26}Fe, ^{56}Ba, and ^{82}Pb). Note the Pb Kα X-ray emission peak around 76 keV in the spectra from the galena models (Fig. 8C). The backscatter peaks are broader for the BGO detector in all the three models compared to either the NaI(Tl) or the CsI(Na) detectors. There is an apparent shift towards the left in the backscatter peak with increase in the effective atomic number of the scattering media, due to the decrease related to the number of low-energy γ-rays recorded as Z increases. The peak position varies from 123 to 173 keV for the NaI(Tl) detector (from pyrite to galena, respectively). Also the rate of falloff of the count rate decreases with increase in the effective Z.

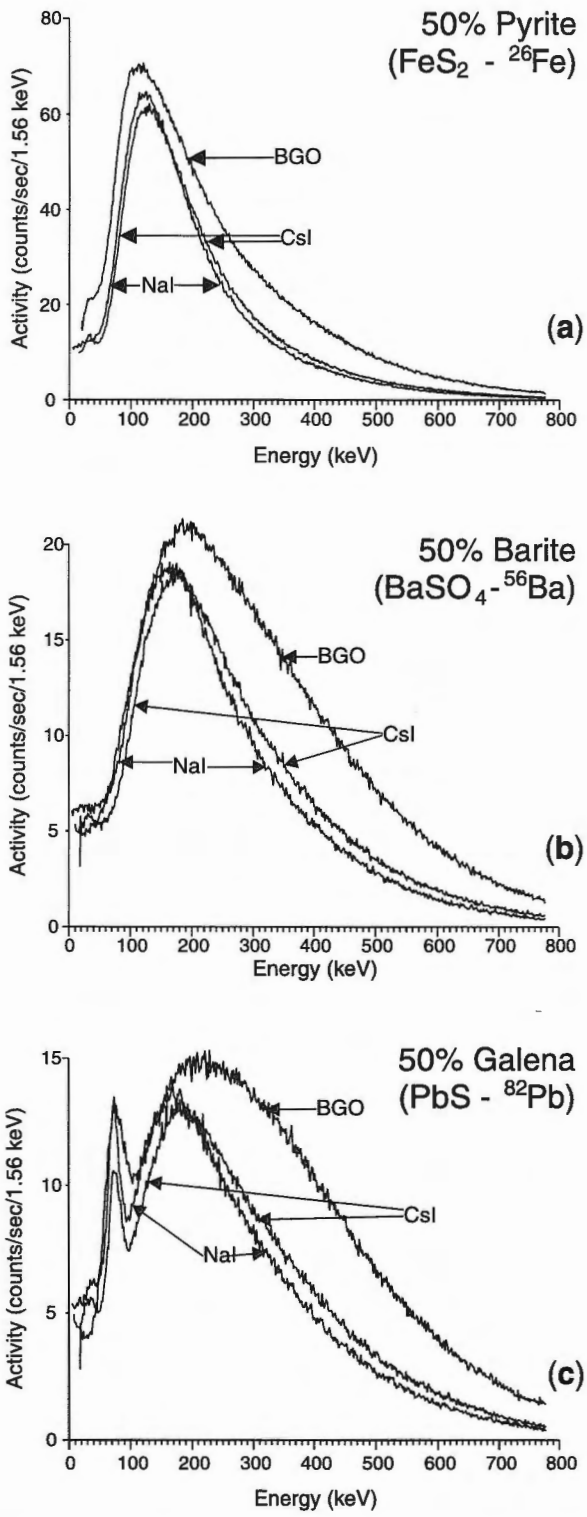

Figure 8. *Backscattered γ-ray spectra from a ^{60}Co source acquired in three high-Z media composed of 50% pyrite (FeS_2) (Fig. 8a), 50% barite ($BaSO_4$) (Fig. 8b), and 50% galena (PbS) models with NaI(Tl), CsI(Na) and BGO scintillation detectors. Five-minute spectra were acquired with a fibreglass probe housing.*

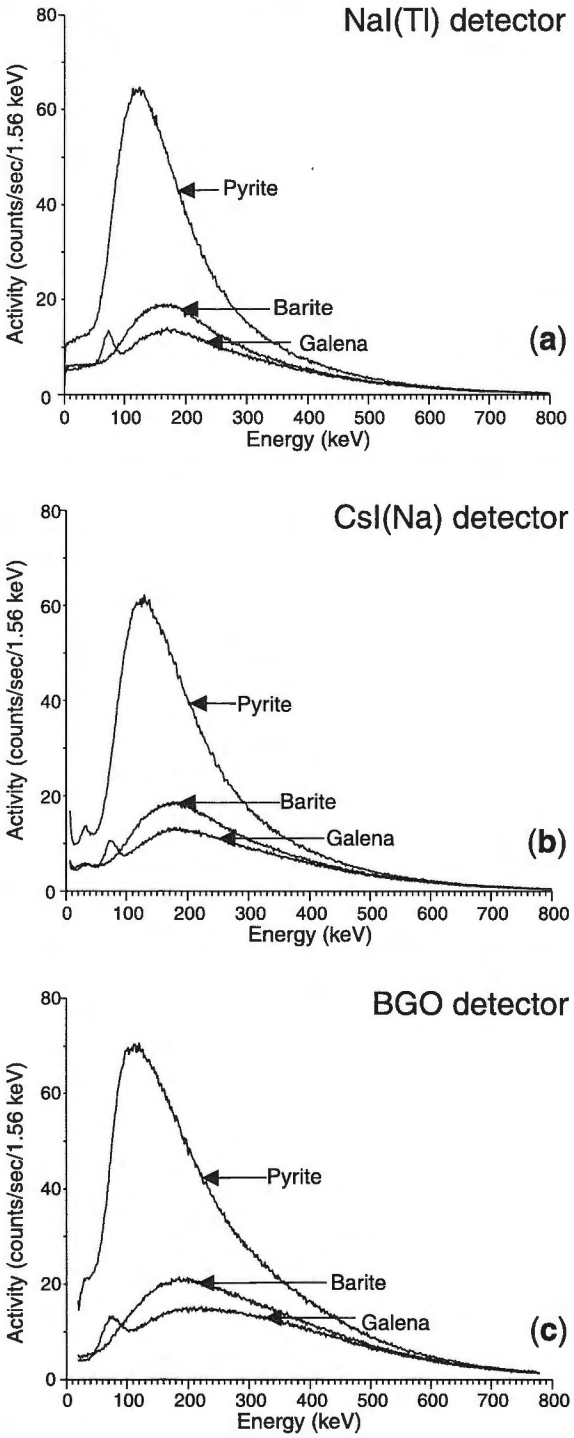

Figure 9. Same data presented in Figure 8 comparing the scattering-media responses for the three scintillation detectors: Five-minute spectra were obtained in a 50% pyrite, barite, and galena models with NaI(Tl) detector (Fig. 9a), CsI(Na) detector (Fig. 9b), and with BGO detector (Fig. 9c).

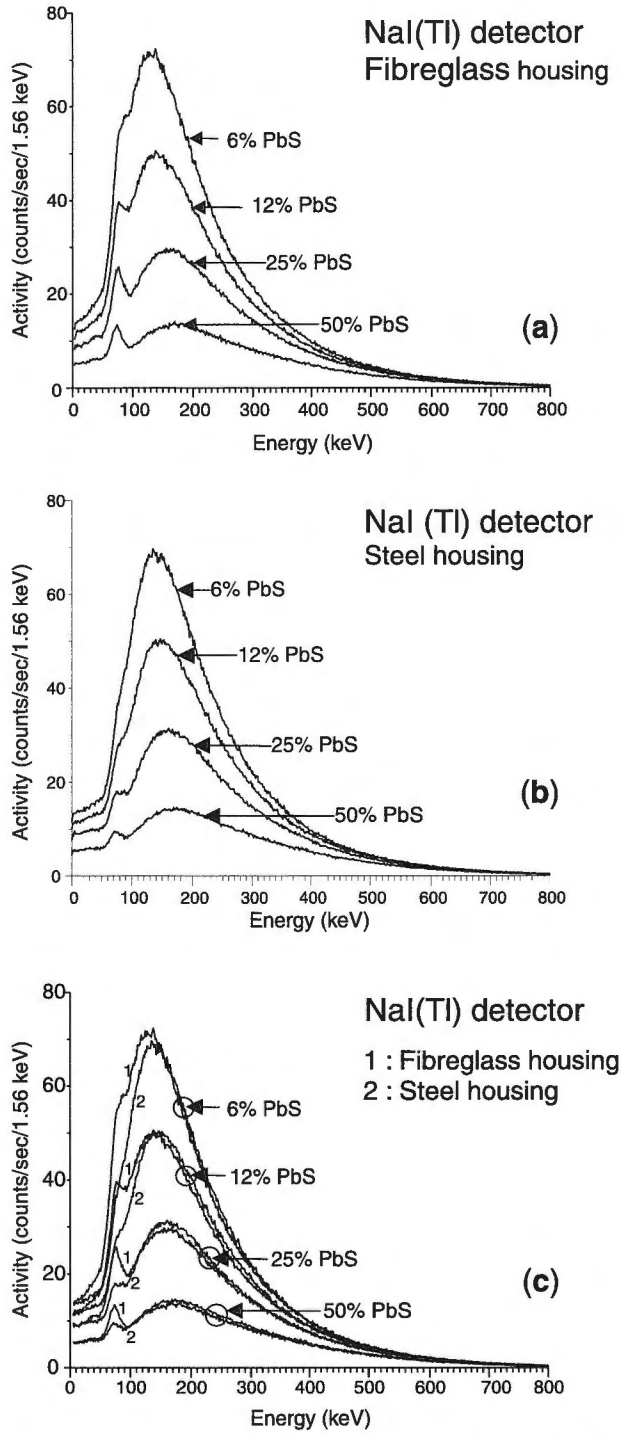

Figure 10. Backscattered γ-ray spectra from a ^{60}Co source recorded in galena models (6%, 12%, 25% and 50% PbS) with a NaI(Tl) detector comparing the spectral response characteristics to different types of probe housings. Five-minute spectra were acquired using a fibreglass probe housing (Fig. 10a), and a stainless-steel probe housing (Fig. 10b). Figure 10c compares data using the two probe housings (Fig. 10a and 10b).

Backscattered γ-rays response to probe housing

Figure 10 shows backscattered γ-ray spectra from a ^{60}Co source recorded in galena models (6%, 12%, 25% and 50% PbS) with a 25 x 76 mm NaI(Tl) detector comparing the spectral response characteristics to different types of probe housings. The spectra were acquired for five minutes with a fibreglass probe housing (Fig. 10a), and with a steel probe housing (Fig. 10b). Figure 10c compares data from Figures 10a and 10b. The steel probe housing significantly attenuates γ-rays in the photoelectric, low-energy region (<150 keV). The Pb Kα X-ray emission peak around 76 keV is virtually non-existent in the 6% and 12% galena models. It starts to appear in the 25% PbS model. Note that all spectral differences occur in the energy region less than 100 keV which is dominated by photoelectric effects, whereas there are only minor differences in the spectral shapes in the high-energy region (100 keV). The steel probe housing, therefore, tends to diminish the ability of the spectral γ-γ technique in detecting and estimating the content of PbS mineralization.

DISCUSSION AND CONCLUSION

One of the primary features in the spectral γ-γ (or selective γ-γ) logging tools is that measurements in the low-energy photoelectric region can be made. It has been shown that the spectral γ-γ ratio of a low-energy window in the photoelectric region and a high-energy window in the Compton region can be used to characterize heavy-element distributions and estimate the concentration of these elements in situ. There are also features in the photoelectric region which make it possible to distinguish the distribution of different types of heavy elements in the backscattering media (Borsaru, 1993). Photoelectric absorption is the most important mode of γ-ray attenuation for energies less than about 100 keV. This process is dominated by elements with the highest atomic number in the backscattering media. Thus the low-energy portion of the backscattered γ-ray spectrum will be strongly influenced by whether or not the backscattered γ-rays came from a high-Z or low-Z medium before reaching the detector. Also the photoelectric absorption of γ-rays is followed by emission of X-rays whose energy depends on the atomic number of the absorbing material (for example, $E_{K\alpha}$ = 74.96 keV for Pb). These secondary peaks provide extremely useful information for discriminating heavy elements in the scattering media. The experiments have shown that the use of low-Z probe-housing material enhances the detection of photoelectric effects resulting from heavy elements with different Z.

Although the presentation of the data in this paper has been mainly qualitative, the information from this study is useful in designing the optimum detector–probe housing configuration for ore delineation and in situ assaying in boreholes with the spectral γ-γ method. Quantitative evaluation of these data is in progress. The shapes of several backscattered γ-ray spectra from the different Z-materials will be analyzed to evaluate Compton scattering and photoelectric absorption effects. These effects will be evaluated in the form of count-rate-independent ratios. The Pb Kα X-ray peak suggests the possibility of using this peak to discriminate Pb from other base metals in a polymetallic deposit and also the possibility of estimating the Pb content. This is part of continuing research at the GSC to develop an in situ assaying technique for base metals. This information may also be used to differentiate between the different backscattering media in the formation (e.g. presence of different heavy elements such as Fe, Cu, Ni, and Pb sulphides). Field experiments to evaluate the performance of the three detectors are scheduled at a copper-lead-zinc polymetallic massive-sulphide deposit. The borehole and scattering media environment will be different in that the boreholes will be water filled and the scattering media saturated with water.

ACKNOWLEDGMENTS

The authors wish to thank Bill Haytt and Jacques Parker for their contribution to the laboratory measurements and Sarah McArthur, our Waterloo co-op student, for the data processing and preparation of the figures.

REFERENCES

Almasoumi, A., Borsaru, M., and Charbucinski, J.
1998: Determination of lead concentration of Pb-Zn ores in laboratory boreholes using gamma-gamma techniques with very low activity sources; Applied Radiation and Isotopes, v. 49, no.1-2, p. 125–131.

Borsaru, M.
1993: Nuclear techniques for in situ evaluation of coal and mineral deposits; Nuclear Geophysics, v.7, no. 4, p. 555–574.

Borsaru, M., Ceravolo, C., Charbucinski, J., Eisler, P.O., and Youl, S.
1983: Comparative performance of BGO and NaI(Tl) detectors for identifying coal sediments by gamma-ray logs; Transaction of the 8th European Formation Evaluation Symposium, London, Paper O.

Conaway, J.G., Killeen, P.G., and Hyatt, W.G.
1980: A comparison of bismuth germanate, cesium iodide, and sodium iodide scintillation detectors for gamma ray spectral logging in small diameter boreholes; *in* Current Research, Part B, Geological Survey of Canada, Paper 80-1B, p.173–177.

Charbucinski, J. and Mathew, P.J.
1982: A backscatter gamma-ray spectrometric method for the determination of ash in coal; Nuclear Instruments and Methods, v. 193, p. 269–273.

Charbucinski, J., Borsaru, M., and Gladwin, M.
1997: Ultra-low radiation intensity spectrometric probe for ore body delineation and grade control of Pb-Zn ore; *in* Proceedings of Exploration 97: Fourth Decennial International Conference on Mineral Exploration,(ed.) A.G. Gubins; GEO F/X Division of Information Systems Ltd, p. 631–638.

Charbucinski, J., Eisler, P.L., Mathew, P.J., and Wylie, A.W.
1977: Use of backscattered gamma radiation for determining grade of iron ores in blast holes and development drill holes; Proceedings of Australasia Institute of Mining and Metallurgy, no. 262, p. 29–37.

Drake D.M.
1981: Bismuth germanate scintillators as detectors for high-energy gamma radiation; Nuclear Instruments Methods, v. 188, p. 313–317.

Ellis, D, Flaum, C., Marienbach, E., Roulet, C., and Seeman, B.
1985: Litho-density tool calibration; Society of Petroleum Engineers; v. 25, no. 4, p. 515–241.

Evans A.E.
1979: Application of bismuth germanate scintillators to detection of high-energy gamma radiation; American Nuclear Society, Transactions v. 33, p. 693–696.

Gearhart, D.A. and Mathis, G.L.
1987: Development of a special litho-density tool by use of empirical methods; The Log Analyst, September-October, v. 28, no. 5, p. 470–487.

Killeen, P.G. and Mwenifumbo, C.J.
1988: Downhole assaying in Canadian mineral deposits with the spectral gamma-gamma method; *in* Current Trends in Nuclear Borehole Logging Techniques for Elemental Analysis, International Atomic Energy Agency Technical Documentation IAEA-TECDOC-464, p 23–29.

Mwenifumbo, C.J.
1991: On the possibility of discriminating between economic and non-economic sulphides by the spectral gamma-gamma method; in Proceedings of the 5th International Symposium of the Minerals and Geotechnical Logging Society, Tulsa, 24–28 October 1993, Paper J, p. 1–14.

Nestor, O.H. and Huang, C.Y.
1975: Bismuth germanate: a high-Z gamma-ray and charged particle detector; Institute of Electrical and Electronic Engineers Transactions on Nuclear Science, NS-22, p. 68–71.

Stromswold, D.C.
1981: Comparison of sodium iodide, cesium iodide and bismuth germanate scintillation detectors for borehole gamma-ray logging; Institute Electrical and Electronic Engineers Transactions on Nuclear Science, NS-28, p. 290.

Geological Survey of Canada Project 880030

Geological landscape of the pre-Inca archeological site at Chavin de Huantar, Peru

Robert J.W. Turner, Rosemary J. Knight[1], and John Rick[2]
GSC Pacific, Vancouver

Turner, R.J.W., Knight, R.J., and Rick, J., 1999: The geological landscape of the pre-Inca archeological site at Chavin de Huantar, Peru; in *Current Research 1999-D; Geological Survey of Canada, p. 47–56.*

Abstract: Chavin de Huantar, a large pre-Inca temple complex in a steep-walled mountain valley, was constructed on three geomorphic elements: the toe of an inactive earthflow, an alluvial fan, and a river floodplain. Part of the temple complex suffered river-bank erosion early this century and structures indicate ancient Chavin inhabitants attempted to control river position. The temple complex and nearby valley floor was buried by a damaging debris flow in 1945. A nearby agricultural plain that likely influenced the siting of the temple complex represents an ancient landslide-dammed lake floor.

The temple is constructed of large stone blocks, mostly sandstone and quartzite with lesser granite, limestone, and volcanic tuff. Sandstone and volcanic tuff could have been quarried locally but the nearest sources for limestone and granite are 3 km and 15 km from the site.

Résumé : Chavin de Huantar, un vaste complexe de temples pré-Inca situé dans une vallée de montagne à versants fortement inclinés, a été construit sur trois reliefs géomorphologiques : la pointe d'une coulée de fluage inactive, un cône de déjection et une plaine d'inondation. Au début du siècle, l'érosion des berges de la rivière a endommagé une partie du site et la présence d'ouvrages indique que les anciens habitants de Chavin avaient tenté de modifier le tracé de la rivière. En 1945, le site et le fond de la vallée avoisinante ont été enfouis sous une coulée de débris. Une plaine agricole adjacente, qui a vraisemblablement influé sur le choix de l'emplacement du site, représente un ancien fond de lac barré par un glissement de terrain.

Le temple a été construit avec de gros blocs, essentiellement de grès et de quartzite avec en quantité moindre du granite, du calcaire et des tufs volcaniques. Le grès et les tufs volcaniques ont probablement été extraits de carrières locales, alors que les sources de calcaire et de granite les plus proches se trouvent à 3 km et à 15 km du site.

[1] Department of Earth and Ocean Sciences, University of British Columbia, #129-2219 Main Mall, Vancouver, British Columbia V6T 1Z4
[2] Department of Anthropology, Stanford University, Stanford, California, 94305-2145

INTRODUCTION

Geomorphic studies of mountain valleys with a record of ancient human occupation offer insights into the issues of long-term human inhabitation of mountain environments. Lessons from such places are particularly relevant to our understanding of the Canadian Cordillera where valleys have only recently been populated and there is relatively little human experience with mountain processes such as debris flows, earthflows, landslides, and floods.

Chavin de Huantar is a large pre-Inca fortress-like temple complex situated in a high elevation valley in the Andes Mountains of Peru. The temple complex is interpreted to have been an active community from 850–250 BC and an important site within the pre-Inca Chavin culture of northern Peru (Bennett, 1944; Tello, 1960; Burger, 1981). The valley within which Chavin de Huantar is situated has probably been inhabited by humans for much of the last 3000 a.

To assist ongoing archaeological work at the temple complex, a reconnaissance geological and geophysical assessment was conducted during July 1998. The primary focus of the geophysical study was to test the use of ground-penetrating radar as a means of imaging below the current excavated surface. The geological studies summarized here provide a preliminary assessment of the geomorphology of the site and of the source of materials used in the construction of the temple complex. It also provides information important for planning and interpreting the geophysical studies.

LOCATION AND PHYSIOGRAPHY

Chavin de Huantar lies on the mountainous eastern flank of the Cordillera Blanca in central Peru, about 280 km northeast of Lima and 40 km southeast of the town of Huaras (Fig. 1, 2). The temple complex lies adjacent to the village of Chavin de Huantar (for which it is named) and can be reached by vehicle from Huaras on paved highway to Catac and gravel road over the Cordillera Blanca via a pass at 4178 m elevation. The temple complex includes a number of megalithic buildings constructed of large stone blocks, as well as terrace surfaces and plazas (Fig. 3, 4a).

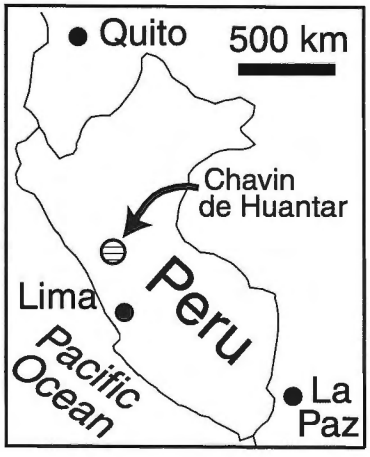

Figure 1. *Location of Chavin de Huantar within Peru.*

The Cordillera Blanca, a part of the continental divide of South America, contains numerous glacier-covered peaks over 6000 m. Southeast of the Cordillera Blanca, a rolling upland surface between 4000–4500 m elevation is deeply incised by tributaries of the north-flowing Rio Mosna. Chavin de Huantar is sited on the floor of the Rio Mosna valley at the confluence with the Rio Huachecsa, a steep tributary draining the east side of the Cordillera Blanca.

BEDROCK GEOLOGY

The extreme topography of the Cordillera Blanca reflects a combination of hard granitic rock resistant to erosion and active tectonic uplift. The granitic rock, granodiorite to quartz monzonite in composition, forms the core of the southern Cordillera Blanca (Fig. 2). The granitic rock has intruded a north-trending belt of folded and faulted sedimentary rocks of the late Jurassic (163–144 Ma) Chicama Formation and early Cretaceous (144–97.5 Ma) Gollarisquizga Group (Instituto Geologico Minero y Metalurgico, 1995a, b). On its western side, the Cordillera Blanca rises 2500 m above the Callejon de Huaylas, a broad sediment-filled valley drained by the Rio Santa. This mountain front has formed by displacement along the Cordillera Blanca fault zone (Schwartz, 1988). Recent movement on parts of the fault system is indicated by fault scarps that cut glacial sediments as young as 10 000 a (Schwartz, 1988).

Chavin de Huantar, and the Rio Huachecsa and Mosna valleys immediately upstream of Chavin de Huantar are underlain by rocks of the Gollarisquizga Group (Fig. 2). The Goyllarisquizga Group has been divided into four formations; in ascending stratigraphic order they are Chimu, Santa, Carhuaz, and Farrat. Based on descriptions of these units (Instituto Geologico Minero Y Metalurgico, 1995a, b) the sandstone and quartzite, which outcrop on lower valley slopes immediately northwest, west, and east of Chavin de Huantar, likely belong to the Chimu Formation. These sandstone and quartzite layers, tilted steeply due to folding, form prominent rib-like outcrops that protrude tens of metres above slopes underlain by recessive-weathering, black siltstone and shale, and minor layers of anthracite coal. A striking fin-like rib of sandstone creates a distinct north-trending cliff immediately west and upslope of the village of Chavin de Huantar (Fig. 4a).

Other formations in the Goyllarisquizga Group are exposed farther from Chavin de Huantar. The Santa Formation is composed of limestone, calcareous shale units, black limestone, and dark fossiliferous shale units; limestone upstream along the Rio Huachecsa and along the Rio Mosna, 5 km upstream of Chavin de Huantar may belong to this formation. The Carhuaz Formation includes red-brown, thin-bedded shale, siltstone, and sandstone. The Farrat Formation is composed of pale grey sandstone and quartzite with cross-bedding, interbedded with grey to brown-red shale units. Dark shale units, sandstone, dark limestone, and volcanic tuff

of the Chicama Formation underlie the Rio Mosna valley east and north of Chavin de Huantar (Instituto Geologico Minero y Metalurgico, 1995b).

SURFICIAL GEOLOGY

A preliminary map of surficial sediments in the immediate Chavin de Huantar area is presented in Figure 3. An interpretation of the subsurface relationships between these units is illustrated in Figure 5.

Bedrock with thin colluvium

Much of the middle and upper slopes of the Rio Mosna and Rio Huachecsa valleys are bedrock with a discontinuous cover of thin rock debris and soil or colluvium. Such bedrock and thin colluvium occurs at the canyon mouth of the Rio Huachecsa (Fig. 4a) and as the low ridge immediately east of Chavin de Huantar (Fig. 4b). Too rocky or steep to cultivate, these slopes support only grass and shrubby vegetation. Resistant bedrock layers form topographic ribs and ridges while softer siltstone and shale layers are recessive and have a mantle of colluvium. The colluvium is a variable mix of silt, sand, and coarse rock fragments.

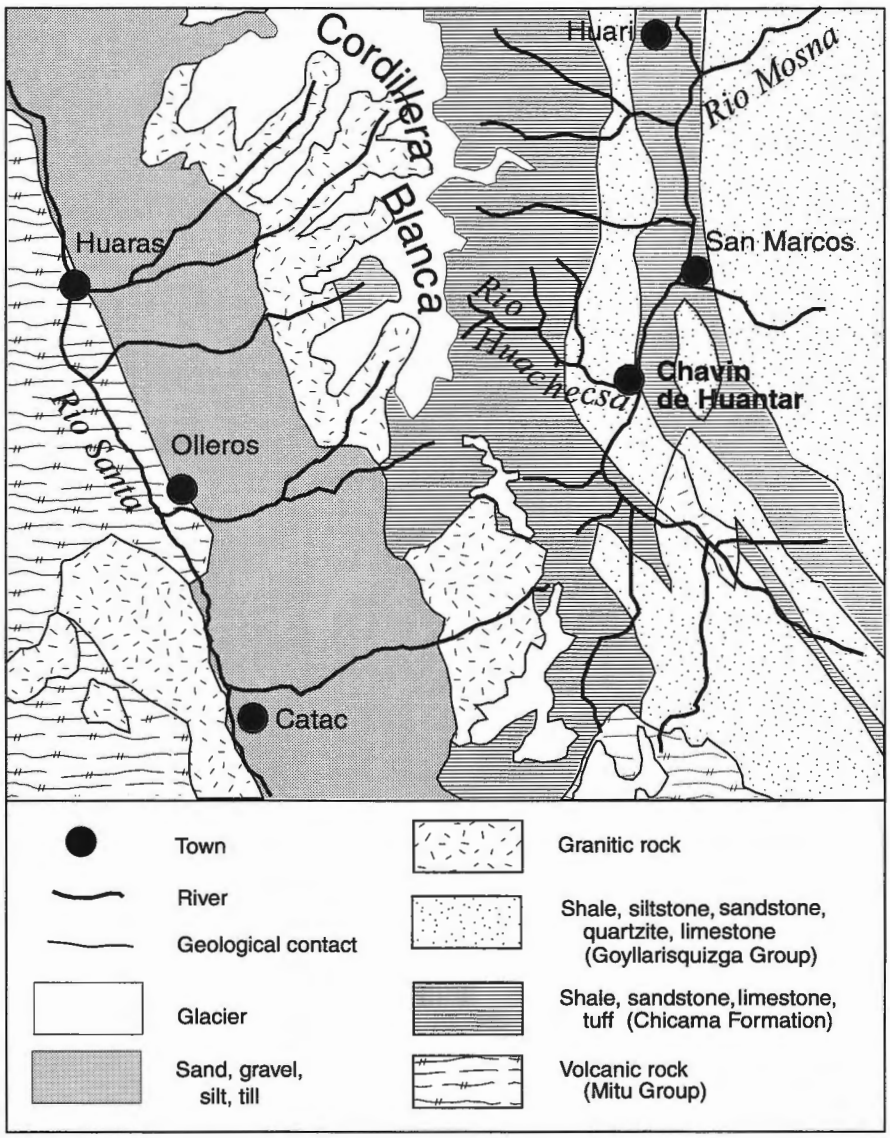

Figure 2. *Geological map of southeastern Cordillera Blanca and Rio Mosna valley. Geology is based on Instituto Geologico Minero y Metalurgico (1995a); extent of glacier cover is from Instituto Geograpfico Nacional (1989).*

Earthflow deposits

Several large lobe-like topographic features extend 1 km or more from the upper slopes to the floor of the Rio Mosna valley. These lobes are hundreds of metres across near the valley floor, narrow in width upslope, and at their highest elevations are transitional into large, upper valley slope basins. Based on morphology, these lobes are interpreted to be earthflow deposits, bodies of rock and soil debris that move downslope by a process of slow creep. Studies elsewhere have shown earthflows to move by slow internal deformation or flow above a basal detachment surface at rates of metres to tens of metres a year, and that periods of movement or accelerated movement can be triggered by long term climate change

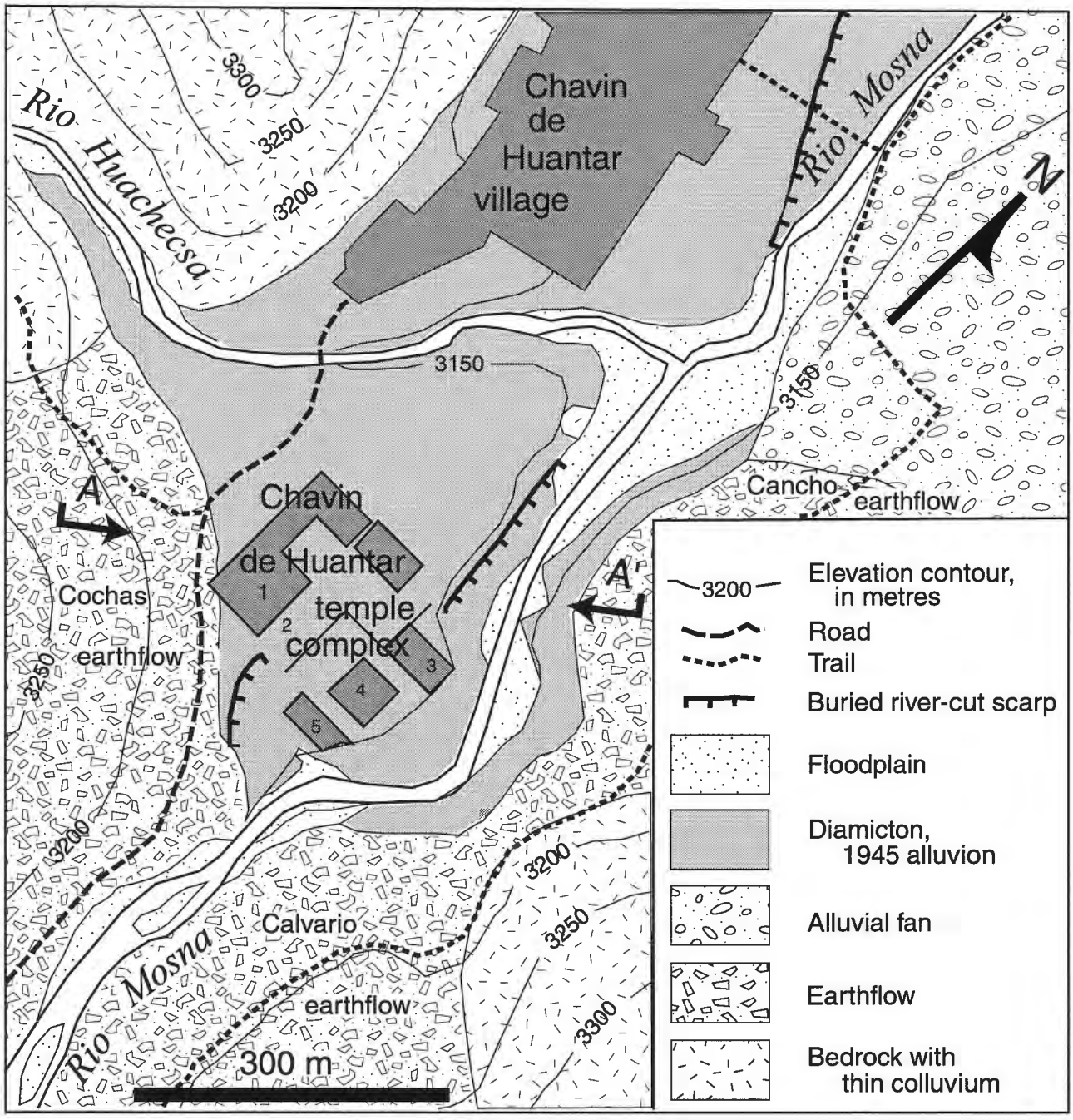

Figure 3. *Geological map of surficial sediments in the immediate area of Chavin de Huantar. Structures labelled within the Chavin de Huantar temple complex are: 1) castillo; 2) upper terrace; 3) north-flanking mound of the New Temple; 4) square plaza, and 5) south-flanking mound of the New Temple. The location of the line of section in Figure 4 is shown.*

(i.e. wetter conditions). The presence of these earthflow deposits in the Rio Mosna valley likely reflects the local abundance of weak bedrock such as organic-rich black siltstone and shale which decompose readily into graphite- or clay-rich particles. This lithology breaks down into a good agricultural soil and thus the surfaces of the earthflows are intensively cultivated. No tilted trees or disrupted roads, rock walls, or houses were observed, suggesting the earthflows are not currently active.

Three major earthflow deposits form much of the middle and lower valley slopes in the immediate Chavin de Huantar area. For the purpose of this paper, these earthflows are referred to by the name of villages on their slopes: Cochas, Calvario, and Cancho. The temple complex of Chavin de Huantar is built at the toe of the Cochas earthflow. At the valley floor, the Cochas earthflow is a kilometre-wide lobe but narrows upslope to a basin-like trough 800 m above the valley near the village of Cochas (Fig. 4c). The soils of the Cochas earthflow are a distinctive pink-brown and roadcuts immediately south of the temple complex expose scattered angular blocks of brick-coloured siltstone and sandstone in a matrix of pink-brown, silty sand and rock fragments (Fig. 4d).

The Calvario earthflow, similar in morphology and size to the Cochas earthflow, lies to the east across the Rio Mosna (Fig. 4b). Like the Cochas earthflow, the Calvario earthflow is intensively cultivated, but distinguished by the dark grey colour of its soil. Where the toe of the Calvario earthflow is exposed in the river bank of the Rio Mosna it is composed of silt- to pebble-size, angular fragments of dark grey siltstone and shale and lesser coarse angular blocks of quartzite up to 20 cm in diameter. To the north, across a ridge of bedrock and thin colluvium and opposite Chavin de Huantar village, is the Cancho earthflow. This earthflow differs from the others as its middle slopes have been cut by a stream canyon and an alluvial fan blankets its lower slopes. The source areas of the Cancho and Calvario earthflows lie adjacent to each other on the upper valley slope and the earthflows share a similar material composition.

Valley floor

Chavin de Huantar temple complex and village sit on a gently east- and north-sloping valley floor surface that is incised by the Rio Mosna and Rio Huachecsa. This valley floor surface, elevated above the modern streams and their floodplains, is

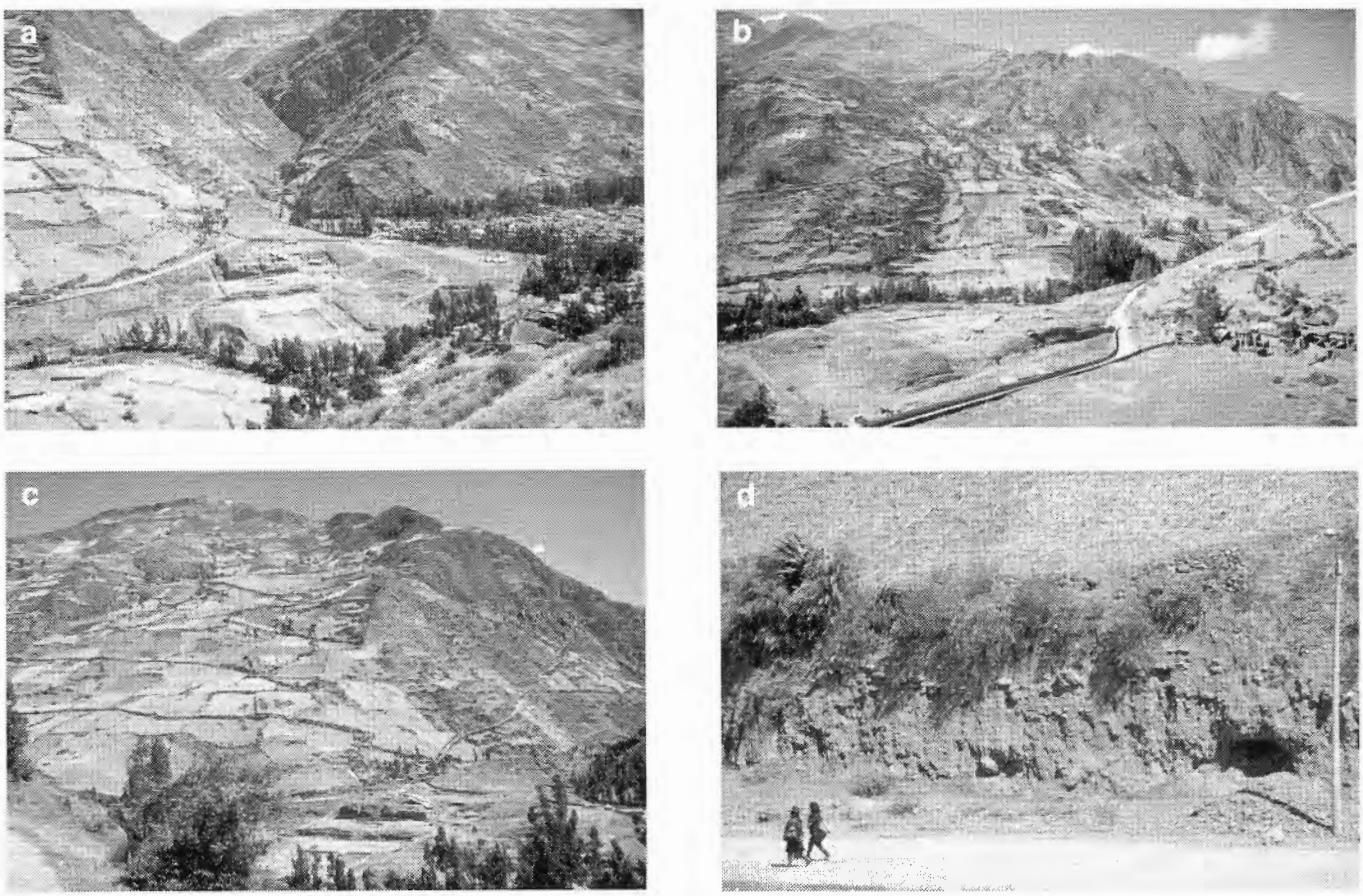

Figure 4. *Photographs of geological landscape features.* ***a)****View to northwest across Chavin de Huantar temple complex and canyon of Rio Huachecsa. Large outcrop on north (right) side of canyon is steeply dipping quartzite.* ***b)****View to southeast across Chavin de Huantar temple complex to Calvario earthflow.* ***c)*** *View to southwest across Chavin de Huantar temple complex at the toe of the Cochas earthflow.* ***d)*** *Angular blocks in fine matrix of Cochas earthflow exposed in a roadcut just south of Chavin de Huantar temple complex.*

mantled by several metres of debris deposited during a major debris flow or 'alluvion' into the valley in 1945 ('alluvion' is the term used in the Peruvian Andes for this type of debris flow; *see* discussion below). This layer of debris covered various geomorphic elements of the valley floor previous to 1945: the alluvial fan of the Rio Huachecsa, a small apron of debris along the base of the Cochas earthflow, floodplain areas of the Rio Mosna and Rio Huachecsa, and human-modified terraces associated with the Chavin de Huantar temple complex. The possible subsurface relationships between these buried valley floor components is illustrated in Figure 5.

The January 1945 alluvion was a high-velocity flow of rock and mud debris that swept down the Rio Huachecsa canyon and into the valley of the Rio Mosna. Geological investigations conducted shortly after the alluvion event by members of the Instituto Geologico del Peru determined that it originated from an avalanche of ice, rock, and mud into a small glacial-debris-dammed lake at 4600 m elevation on the flanks of the Cordillera Blanca, 15 km east of Chavin de Huantar (Indacochea y Iberico, 1945; Spann, 1947). The avalanche material, mixed with lake water, overtopped and breached the debris dam and descended the Rio Huachecsa canyon, incorporating additional material from the stream channel along its path. At the mouth of the canyon, the alluvion, with an estimated volume of 900 000 m^3, spread out of the channel and across the alluvial fan, destroying the southernmost part of Chavin de Huantar village, killing a number of villagers, and burying archeological excavations that were in progress at the Chavin de Huantar temple complex. The main flow of the alluvion followed the channel of the Rio Huachecsa, and continued down the Rio Mosna valley for several kilometres.

Alluvion debris is exposed in the stream banks of the Rio Huachecsa and Rio Mosna, and in excavations within the temple complex and southern Chavin de Huantar village. The alluvion debris varies in thickness from 1 m to more than 5 m and is diamicton composed of a dark grey, silty sand matrix with abundant angular rock fragments and rounded cobbles and boulders that typically are less that 0.3 m in diameter (Fig. 6). However, boulders in excess of 2 m diameter are present in the diamicton along the Rio Huachecsa where the main flow of the alluvion was focused.

The valley floor surface from the village of Chavin de Huantar to the northwestern areas of the temple complex slopes away from the mouth of Rio Huachecsa canyon (Fig. 4a). This surface is interpreted as an alluvial fan of rock debris deposited by the Rio Huachecsa where it flows from its confined, high gradient canyon and enters the broad, lower gradient Rio Mosna valley. Deposition on the fan surface is

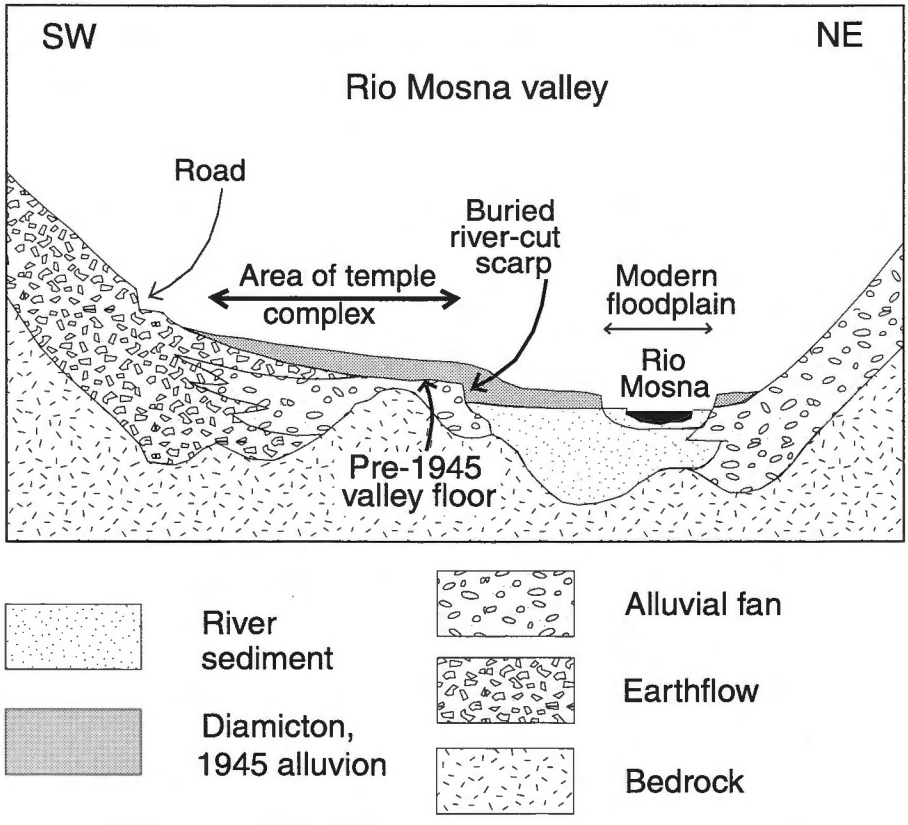

Figure 5. *A schematic cross-section oriented from southwest to northeast across the Chavin de Huantar temple complex illustrating possible subsurface relationships between geological units present on surface. The legend and location of section is shown on Figure 3.*

likely restricted to rare, extreme flood or alluvion events as was the case in January 1945; typical stream flow is confined to an incised channel across the fan.

Little is known of the nature of alluvial fan materials underlying the 1945 alluvion debris. However, excavations at the temple complex immediately west and east of the castillo expose alluvion diamicton above a layer of pink-brown, matrix-rich, stony debris 1–2 m thick and an underlying layer of coarse, angular rock rubble with lesser fine matrix. Similar layers were noted underlying alluvion diamicton in an excavation in southwestern Chavin de Huantar village. The middle layer is similar in colour to the Cochas earthflow and is likely derived from it. The gentle northward slope of the land surface away from the toe of the Cochas earthflow along the southwestern side of the temple complex suggests that debris eroded from the earthflow surface has spread north across the alluvial fan. A shallow, basin-like area on the lower Cochas earthflow just above the temple complex appears to be the head scar of a recent landslide. Such landslides are likely triggered by periods of heavy rain during the wet season when the soils are saturated with water.

Figure 6. *Exposure of the upper part of the 1945 alluvion diamicton exposed in excavation 100 m northwest of temple complex. Ice axe for scale.*

The thickness of sediment overlying bedrock in the valley near the temple complex is unknown, but bedrock is locally exposed at surface suggesting that the sediment fill is not thick (Fig. 5). A small knob of sandstone and shale occurs near the confluence of the Rio Mosna and Rio Huachecsa and thin-bedded shale and sandstone are exposed northwest of the square plaza in the temple complex. Both are interpreted as bedrock rather than the tops of large boulders as they share similar orientation of bedding (335–345° strike, 60–90°SW dip).

A well developed alluvial fan forms the lower valley slope immediately east of the village of Chavin de Huantar (Fig. 3). Unvegetated lobes of gravel on cultivated fields and fresh gullies in the fan surface were observed and indicate that the fan is actively forming during flood events.

A distinct, north-trending scarp, 2–3 m high is present immediately northeast of the temple complex (Fig. 3). The scarp separates the gently east-dipping elevated surface of the alluvial fan from a lower terrace surface that slopes gently northwards. Material exposed immediately above, on, and below the scarp is alluvion diamicton, and stream banks of the Rio Mosna cut into the lower terrace also expose alluvion diamicton. The scarp parallels the course of the Rio Mosna, and it is likely an old river-cut scarp of the Rio Mosna, partially buried by the 1945 alluvion (Fig. 5). Given this interpretation, it follows that the lower terrace is a floodplain of the Rio Mosna buried by the 1945 alluvion.

A similar terrace occurs immediately south of the temple complex. The terrace is separated from more elevated areas to the west by a discontinuous bank that is partly obscured by excavated debris from recent archeological work. A photograph of this area in 1945 immediately following the alluvion shows this lower terrace to be bound on the west by a distinct crescent-like scarp that has the morphology of a river-cut scarp (Lamina LIII *in* Tello, 1960).

Much of the eastern part of the temple complex lies east of a line joining the scarps to the north and south as illustrated in Figure 3. This suggests that features such as the south- and north-flanking mounds of the New Temple, and square plaza where built wholly or in part on a floodplain surface of the Rio Mosna. Photographs and maps indicate that during the 1930s the channel of the Rio Mosna was west of its present position and was actively eroding the south flanking mound of the New Temple (Lamina XIV, XV, and Fig. 5 *in* Tello, 1960). This river erosion of the temple complex must mark the westernmost transgression of the river channel since the ancient Chavin civilization, as no other river erosion of the temple complex is evident. Photographs of the Chavin de Huantar site immediately following the 1945 alluvion (Lamina LIII *in* Tello, 1960) show the position of the Rio Mosna near its present position and suggest that the debris flow displaced the river channel eastward, terminating river erosion of the Chavin de Huantar site.

Gravels from this river channel predating 1945 are exposed in the present bank of the Rio Mosna immediately east of the square plaza. The river gravels are well sorted pebbles and cobbles, and some layers up to 1 m thick display inclined bedding (crossbedding). The gravels are overlain by

the 1945 alluvion diamicton, and interbedded with as many as three other diamicton layers that vary in colour from grey to pink-brown and are up to 1 m thick.

Modern river floodplain

Flat surfaces, some vegetated with grass and eucalyptus trees lie within 1 m of the elevation of the average July river levels of the Rio Mosna and Rio Huachecsa. These floodplain surfaces are bounded by scarps cut by the river into the 1945 alluvion diamicton and underlying sediments.

CONSTRUCTION MATERIALS

The walls of the Chavin de Huantar temple complex are constructed of large blocks of sandstone and quartzite. Lesser amounts of granite, limestone, and volcanic tuff as used for ornamental and specialty purposes. Many sandstone and quartzite slabs are striated on one surface, suggesting that they were dragged to the site. Potential sources for quarried sandstone, quartzite, and tuff occur within 1 km of the temple complex but the nearest sources for limestone and granite are at least 3 km and 15 km distant from Chavin de Huantar respectively.

Quartz sandstone and quartzite

Blocks of pale grey, cream, and reddish-brown-stained sandstone and grey to white quartzite blocks 1 m in width and height and as much as several metres in length (Fig. 7a) were used to construct the Chavin de Huantar temple complex. The sandstone is composed predominantly of quartz grains 0.1–0.2 mm in diameter with an intergranular mineral cement of finer grained quartz, clay, and mica. Intergranular pore space can be as much as 10–20% of the rock volume and may reflect dissolution of soluble mineral cements (e.g. calcite) in the surface weathering environment.

Quartzite is also a quartz-rich sandstone, but is an intergrown mosaic of quartz grains 0.2–0.5 mm in diameter with only minor clay minerals. This pure quartz composition and lack of porosity gives the quartzite greater hardness, paler colour, and a more lustrous appearance. Both sandstone and quartzite blocks can lack internal structure or display laminations parallel to or inclined to bedding (Fig. 7a).

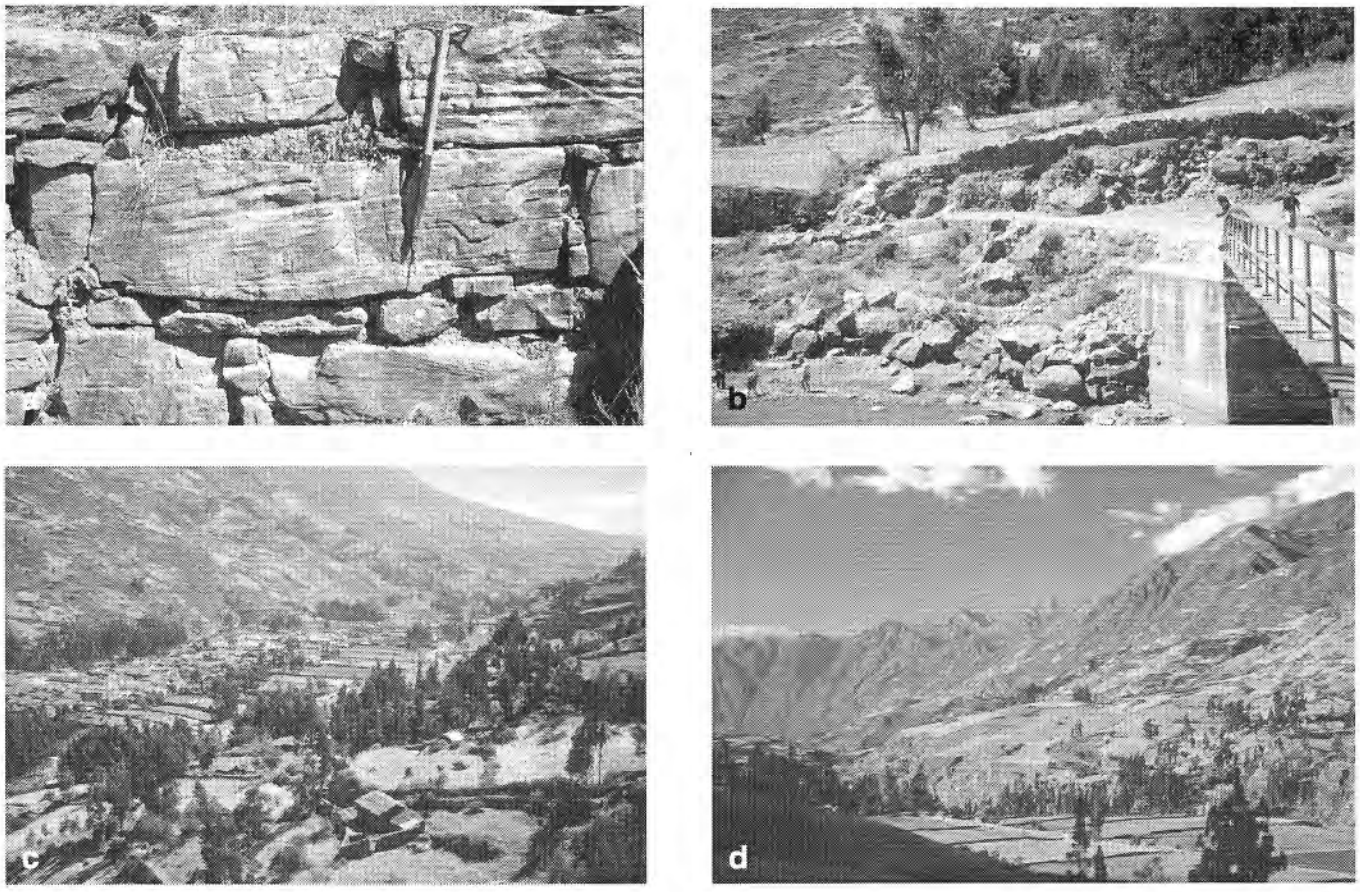

***Figure 7. a)** Sandstone blocks with crossbedding, south-flanking mound of the New Temple of temple complex. **b)** Large blocks of volcanic tuff in bank of Rio Mosna east of Chavin de Huantar village. **c)** View north across valley floor plain in Rio Mosna valley downstream of Chavin de Huantar. **d)** View northeast of landslide across Rio Mosna valley and northern limit of valley floor plain.*

It is likely that sandstone and quartzite blocks reflect the thickness of the original sedimentary layer from which they were quarried, as interbedded shale or siltstone would provide a natural plane of weakness along which the rock would break.

Granite

Granitic rock was employed for specialty purposes such as stairs (blocks to 3 m length) and engraved blocks. The granitic rock is pale grey and composed of interlocking grains 1–3 mm in diameter of grey feldspar and lesser black amphibole and biotite (3–7%) and grey quartz (3–10%). There is no granitic bedrock in the local Chavin de Huantar area, and granitic boulders in the Rio Mosna and Rio Huachecsa are too small to be a likely source for quarry material.

Granitic rock (granodiorite to tonalite composition) forms much of the Cordillera Blanca west of the continental divide (Fig. 2; Instituto Geologico Minero y Metalurgico, 1995b). The closest sites of granitic bedrock to Chavin de Huantar are 1) about 18 km southwest of Chavin de Huantar and west of the continental divide along the trail from Chavin de Huantar to Olleros, 2) about 15 km upstream to the southwest along the continental divide on the road to Catac, and 3) about 15 km upstream to the southeast in the Rio Mosna valley.

Limestone

Large blocks of dark, fine-grained limestone were used for stairs and large ornamental plates in the temple complex. An exceptionally large block in excess of 2 m in length and width sits near the square plaza. The limestone can contain abundant fossil debris and white calcite veins.

Similar dark limestone is exposed along the Rio Huachecsa valley 3–4 km west of Chavin between the villages of Racri and Lanchan and about 5 km upstream of Chavin de Huantar along the Rio Mosna.

Volcanic tuff

Soft, porous volcanic tuff was used for carving small rock sculpture (e.g. tenon heads) and large rock columns. One tenon head (number D52) contains abundant grey to white rectangular crystals (phenocrysts) of feldspar to 2 mm diameter, lesser grains of black amphibole and grey quartz, and lithic fragments of pale quartzite and black siltstone up to 1 cm in diameter. Large, 2 m high columns on the east side of the castillo are carved from a different volcanic tuff that is brownish-grey and contains 30–50% feldspar phenocrysts and 10–20%, 1–2 mm pores.

Boulders of volcanic tuff to 4 m in diameter along the bank of the Rio Mosna at the bridge east of Chavin de Huantar village (Fig. 7b) are similar in composition to the tuff used to carve the tenon head described above. These boulders are likely part of a rockfall or landslide that descended to the valley floor from the upper valley slope to the east. This slope is underlain by Chicama Formation (Fig. 2) that is reported to include tuff (Instituto Geologico Minero y Metalurgico, 1995b). These boulders are large enough to provide the material for carving small sculpture such as the tenon heads. It is unclear whether the tuff used to carve the larger rock columns could have been quarried from these boulders.

INFLUENCE OF LANDSCAPE ON CHAVIN DE HUANTAR

Siting of the Chavin de Huantar temple complex

A number of aspects of the local landscape favour the Chavin de Huantar temple site including reliable water supply, and junction of major valley transportation routes. In addition, a fertile valley floor plain 2.5 km by 1 km in dimension lies immediately north of Chavin de Huantar village (Fig. 7c, 7d). The origin of this plain, an unusual geographic element within the Rio Mosna valley, is briefly considered here.

The plain extends downstream to a ridge of landslide debris tens of metres high that has descended the eastern valley slope (Fig. 7d). The channel of the Rio Mosna is incised into the plain and has cut a canyon through the landslide. Below the landslide, the gradient of the Rio Mosna increases, descending about 170 m over the next 5 km. It is likely that the origin of the plain relates to the landslide event and a possible scenario is offered here. The landslide descended into the valley, blocking the waters of the Rio Mosna and causing the formation of a lake. Sediment carried by the Rio Mosna was deposited within the lake, filling the lower valley with a thick sequence of sediment. When the Rio Mosna finally breached the landslide dam and the lake drained, the lake sediments remained as a plain. Since that time the Rio Mosna has cut down through both the landslide and lake sediments.

Erosion by the Rio Mosna

The square plaza and adjacent flanking mounds of the New Temple were built on the floodplain of the Rio Mosna during a period of temple expansion and were vulnerable to erosion and flooding by the Rio Mosna. There is evidence that Chavin de Huantar inhabitants attempted to control the position of the river channel. There are remnants of rock walls along the western bank of the Rio Mosna east of the temple complex; photographs indicate similar walls existed along the eastern bank as recently as the 1930s (Lamina XLVI *in* Tello, 1960) but could not be located during this study. Above the east bank are a row of aligned quartzite monoliths that such a river bank wall would have served to protect. Large quartzite blocks of similar dimension lie nearby within the bed of the Rio Mosna, and indicate erosion and toppling of monoliths.

Remains of an east-trending rock wall about 3 m wide and 1.5 m high, interpreted to have been built by ancient Chavin inhabitants, intersects the west bank of the Rio Mosna and lies just upstream from the temple complex. The end of the wall has been eroded by the Rio Mosna and within the present river bed is a large slab of quartzite (2 m x 2 m x 0.3 m) positioned on its edge and oblique to the flow of the river. The orientation of the slab deflects the river current toward the eastern bank, and would have protected both the wall and also the temple complex downstream from stream erosion.

Alluvion events

Given the catastrophic impact of 1945 alluvion, one is led to wonder whether similar earlier events occurred during or following occupation of the temple complex. Debris layers buried in the shallow subsurface of the Chavin de Huantar area deserve further study. Several layers of poorly sorted debris interbedded with river channel gravels are exposed in the banks of the Rio Mosna; these could represent deposition from alluvions that descended either the Rio Mosna or Rio Huachecsa.

Two stone block bridges probably built by the ancient Chavin people were present over the Rio Huachecsa earlier this century (Lamina XLVII *in* Tello, 1960). These bridges were destroyed by the 1945 alluvion and it is unlikely they could have survived a previous alluvion of similar size. This suggests that catastrophic debris flows of the magnitude of the 1945 event have not descended the Rio Huachecsa since final occupation of the Chavin de Huantar temple complex.

REFERENCES

Bennett, W.C.
1944: The north highland of Peru — excavations in the Callejon de Huaylas and Chavin de Huantar; Anthropological Papers of the American Museum of Natural History, v. 39, pt. 1, New York, 114 p.

Burger, R.L.
1981: The radiocarbon evidence for the temporal priority of Chavin de Huantar; American Antiquity, v. 46, n. 3, p. 592-602.

Instituto Geologico Minero y Metalurgico
1995a: Mapa geologico del Peru, actualisado a diciembre de 1994, version digital, escala: 1:1 000 000; Sector Energia Y Minas, Lima.
1995b: Geologia del Peru, Boletin N° 55, Serie A; Carta Geologica Nacional, Sector Energia Y Minas, Lima, 176 p.

Indacochea, G.A. y Iberico, M.
1945: Aluvionamiento de Chavin de Huantar el 17 de Enero de 1945; Boletin N. 20, Sociedad Geologica del Peru, p. 21–28.

Instituto Geograpfico Nacional
1989: Huaraz, Peru; hoja SC 18-5, edicion 1, Americas 1:250 000, escala 1:250 000.

Schwartz, D.P.
1988: Paleoseismicity and neotectonics of the Cordillera Blanca fault zone, northern Peruvian Andes; Journal of Geophysical Research, B, Solid Earth and Planets, v. 93, no. 5, p. 4712-4730.

Spann, H.J.
1947: Informe sobre el origen de la catástrofe de Chavin de Huantar, Boletin de la Sociedad Geologica del Peru, tomo XX, p. 29–33.

Tello, J.C.
1960: Chavin Cultura Matriz del la Civilizacion Andina; primera parte, La Universidad de San Marcos, Lima, Peru, 425 p.

Geological Survey of Canada Project 9800-01

AUTHOR INDEX

NOTE TO CONTRIBUTORS

Submissions to the Discussion section of Current Research are welcome from both the staff of the Geological Survey of Canada and from the public. Discussions are limited to six double-spaced typewritten pages (about 1500 words) and are subject to review by the Managing Editor. Discussions are restricted to the scientific content of Geological Survey reports. General discussions concerning sector or government policy will not be accepted. All manuscripts must be computer word-processed on an IBM compatible system and must be submitted with a diskette using WordPerfect. Illustrations will be accepted only if, in the opinion of the editor, they are considered essential. In any case no redrafting will be undertaken and reproducible copy must accompany the original submissions. Discussion is limited to recent reports (not more than two years old) and may be in either English or French. Every effort is made to include both Discussion and Reply in the same issue. Current Research is published in January and July. Submissions should be sent to the Managing Editor, Geological Survey of Canada, 601 Booth Street, Ottawa K1A 0E8.

AVIS AUX AUTEURS D'ARTICLES

Nous encourageons tant le personnel de la Commission géologique que le grand public à nous faire parvenir des articles destinés à la section discussion de la publication Recherches en cours. Le texte doit comprendre au plus six pages dactylographiées à double interligne (environ 1500 mots), texte qui peut faire l'objet d'un réexamen par la rédactrice en chef administrative. Les discussions doivent se limiter au contenu scientifique des rapports de la Commission géologique. Les discussions générales sur le Secteur ou les politiques gouvernementales ne seront pas acceptées. Le texte doit être soumis à un traitement de texte informatisé par un système IBM compatible et enregistré sur disquette WordPerfect. Les illustrations ne seront acceptées que dans la mesure où, selon l'opinion du rédacteur, elles seront considérées comme essentielles. Aucune retouche ne sera faite aux illustrations et dans tous les cas, une copie qui puisse être reproduite doit accompagner le texte original. Les discussions en français ou en anglais doivent se limiter aux rapports récents (au plus de deux ans). On s'efforcera de faire coïncider les articles destinés aux rubriques discussions et réponses dans le même numéro. La publication Recherches en cours paraît en janvier et en juillet. Les articles doivent être envoyés à la rédactrice en chef administrative, Commission géologique du Canada, 601, rue Booth, Ottawa K1A 0E8.

Geological Survey of Canada Current Research, is released twice a year, in January and July. The four parts published in January 1999 (Current Research 1999-A to D) are listed below.

Recherches en cours, une publication de la Commission géologique du Canada, est publiée deux fois par année, en janvier et en juillet. Les quatre parties publiées en janvier 1999 (Recherches en cours 1999-A à D) sont énumérées ci-dessous.

Part A:	Cordillera and Pacific Margin
Partie A:	Cordillère et marge du Pacifique
Part B:	Interior Plains and Arctic Canada
Partie B:	Plaines intérieures et région arctique du Canada
Part C:	Canadian Shield
Partie C:	Bouclier canadien
Part D:	Eastern Canada and national and general programs
Partie D:	Est du Canada et programmes nationaux et généraux